

# Tectonics

## RESEARCH ARTICLE

10.1029/2019TC005735

### Key Points:

- The Alichur dome was tectonically exhumed from 10–15 km depth between ~16 and 4 Ma at ~1.1 km/Myr by syn-collisional ~N–S extension
- Dome-scale boudinage and divergent footwall exhumation reflect subordinate westward lateral extrusion coeval with dominant ~N–S extension
- Basal shear imposed by the underthrusting Indian lithosphere enabled ~N–S extension in the South Pamir to outlast that in the Central Pamir

### Supporting Information:

- Supporting Information S1
- Figure S1
- Figure S2
- Figure S3
- Figure S4
- Figure S5
- Data Set S1
- Data Set S2
- Data Set S3
- Data Set S4
- Table S1–S9

### Correspondence to:

J. R. Worthington,  
jworthin@caltech.edu

### Citation:

Worthington, J. R., Ratschbacher, L., Stübner, K., Khan, J., Malz, N., Schneider, S., et al. (2020). The Alichur Dome, South Pamir, Western India–Asia Collisional Zone: Detailing the Neogene Shakh-dara–Alichur Syn-collisional Gneiss-Dome Complex and Connection to Lithospheric Processes. *Tectonics*, 39, e2019TC005735. <https://doi.org/10.1029/2019TC005735>

Received 26 JUN 2019

Accepted 9 NOV 2019

Accepted article online 14 NOV 2019

©2019. American Geophysical Union.  
All Rights Reserved.

## The Alichur Dome, South Pamir, Western India–Asia Collisional Zone: Detailing the Neogene Shakh-dara–Alichur Syn-collisional Gneiss-Dome Complex and Connection to Lithospheric Processes

James R. Worthington<sup>1,2,3</sup> , Lothar Ratschbacher<sup>2</sup> , Konstanze Stübner<sup>2,4</sup> , Jahanzeb Khan<sup>2,5</sup> , Nicole Malz<sup>2,6</sup> , Susanne Schneider<sup>2</sup>, Paul Kapp<sup>1</sup> , James B. Chapman<sup>1,7</sup>, Andrea Stevens Goddard<sup>8</sup> , Hanna L. Brooks<sup>1,9,10</sup> , Hector M. Lamadrid<sup>11,12</sup> , Matthew Steele-MacInnis<sup>1,9</sup>, Daniel Rutte<sup>2,13</sup> , Raymond Jonckheere<sup>2</sup>, Jörg Pfänder<sup>2</sup>, Bradley R. Hacker<sup>14</sup> , Ilhomjon Oimahmadov<sup>15</sup>, and Mustafo Gadoev<sup>15</sup> 

<sup>1</sup>Department of Geosciences, University of Arizona, Tucson, AZ, USA, <sup>2</sup>Geologie, TU Bergakademie Freiberg, Freiberg, Germany, <sup>3</sup>Now at Division of Geological and Planetary Sciences, California Institute of Technology, Pasadena, CA, USA, <sup>4</sup>Now at Geowissenschaften, Universität Potsdam, Potsdam, Germany, <sup>5</sup>Now at Institute of Geology, The University of Azad Jammu and Kashmir, Muzaffarabad, Pakistan, <sup>6</sup>Geologie, Mineralogie, & Geophysik, Ruhr-Universität Bochum, Bochum, Germany, <sup>7</sup>Now at Department of Geology and Geophysics, University of Wyoming, Laramie, WY, USA, <sup>8</sup>Department of Geology, Rowan University, Glassboro, NJ, USA, <sup>9</sup>Department of Earth and Atmospheric Sciences, University of Alberta, Edmonton, Alberta, Canada, <sup>10</sup>Now at School of Earth and Climate Sciences, University of Maine, Orono, ME, USA, <sup>11</sup>Department of Earth Sciences, University of Toronto, Toronto, Ontario, Canada, <sup>12</sup>Now at Department of Geological Sciences, University of Missouri, Columbia, MO, USA, <sup>13</sup>Now at Institut für Geowissenschaften, Universität Bonn, Bonn, Germany, <sup>14</sup>Department of Earth Science, University of California, Santa Barbara, CA, USA, <sup>15</sup>Institute of Geology, Earthquake Engineering and Seismology, Tajik Academy of Science, Dushanbe, Tajikistan

**Abstract** Neogene, syn-collisional extensional exhumation of Asian lower–middle crust produced the Shakh-dara–Alichur gneiss-dome complex in the South Pamir. The <1 km-thick, mylonitic–brittle, top-NNE, normal-sense Alichur shear zone (ASZ) bounds the 125 × 25 km Alichur dome to the north. The Shakh-dara dome is bounded by the <4 km-thick, mylonitic–brittle, top-SSE South Pamir normal-sense shear zone (SPSZ) to the south, and the dextral Gunt wrench zone to its north. The Alichur dome comprises Cretaceous granitoids/gneisses cut by early Miocene leucogranites; its hanging wall contains non/weakly metamorphosed rocks. The 22–17 Ma Alichur-dome-injection-complex leucogranites transition from foliation-parallel, centimeter- to meter-thick sheets within the ASZ into discordant intrusions that may comprise half the volume of the dome core. Secondary fluid inclusions in mylonites and mylonitization-temperature constraints suggest Alichur-dome exhumation from 10–15 km depth. Thermochronologic dates bracket footwall cooling between ~410–130 °C from ~16–4 Ma; tectonic cooling/exhumation rates (~42 °C/Myr, ~1.1 km/Myr) contrast with erosion-dominated rates in the hanging wall (~2 °C/Myr, <0.1 km/Myr). Dome-scale boudinage, oblique divergence of the ASZ and SPSZ hanging walls, and dextral wrenching reflect minor approximately E–W material flow out of the orogen. We attribute broadly southward younging extensional exhumation across the central South Pamir between ~20–4 Ma to: (i) Mostly northward, foreland-directed flow of hot crust into a cold foreland during the growth of the Pamir orocline; and (ii) Contrasting effects of basal shear related to underthrusting Indian lithosphere, enhancing extension in the underthrust South Pamir and inhibiting extension in the non-underthrust Central Pamir.

### 1. Introduction

Gneiss domes—dome-shaped culminations of higher-grade rocks mantled by lower-grade rocks—express the geodynamics that govern their hosting orogens (e.g., Whitney et al., 2004; Yin, 2004). In general, gneiss domes in both Cordilleran-style and collisional orogens record an early phase of burial during plate convergence, followed by exhumation during either lithosphere-scale extension (for Cordilleran-style domes) or continued plate convergence (for syn-collisional domes). Cordilleran-style gneiss domes, exemplified by the metamorphic-core complexes in the North American Cordillera (e.g., Coney & Harms, 1984), are exhumed by bounding extensional shear zones that are kinematically congruent with a tectonic

framework of post-collisional extension. By contrast, extensional shear zones that bound and exhume syn-collisional gneiss domes are incongruent with the regional framework of ongoing plate convergence and represent components of a complex fault network that includes shortening and/or relay structures that extend laterally and/or vertically through the crust. Kinematically incongruent syn-collisional extensional gneiss-dome exhumation involves extension that is either perpendicular (e.g., Laskowski et al., 2017; Murphy et al., 2002; Ratschbacher et al., 1989) or parallel (e.g., de Sigoyer et al., 2004; Horton et al., 2015) to the plate-convergence azimuth. In either case, an understanding of how extensional gneiss domes reflect collisional dynamics is only achievable by evaluating them as components of regional contractional and transcurrent fault/shear-zone networks.

Gneiss domes that are exhumed by non-coaxial crustal extension are asymmetric both in map view and in cross section because they are bounded by a detachment fault, which defines one limb of the dome and juxtaposes upper-crustal hanging wall rocks with more deeply derived footwall rocks. The detachment localizes strain and displays a broad, upward-convex geometry (Tirel et al., 2004). The underlying mylonites are overprinted by brittle, commonly chloritized structures that resulted from downward migration of the brittle-ductile transition with respect to the exhuming dome. Footwall cooling ages are predicted to decrease and metamorphic grade is predicted to increase from the dome interior toward the detachment (e.g., Yin, 2004). The hanging wall can be coherent or broken by normal faults and commonly carries syn-extensional basins.

The northward-convex Pamir salient in Afghanistan, Tajikistan, and China forms the northwestern extension of the Tibet plateau within the India–Asia collision zone and comprises—like Tibet—terrane that were accreted to Asia (Schwab et al., 2004). Suture zones delineate the North Pamir—Paleozoic–early Mesozoic arcs and subduction-accretion systems built on Asian continental crust, and the Central and South Pamir—parts of Gondwana that accreted to Asia during the Mesozoic (Figure 1). The Central Pamir is bounded to the north by the early Mesozoic Tanyamas suture (e.g., Burtman & Molnar, 1993). The South Pamir, which is continuous with the Hindu Kush–Karakorum ranges to the south, is bounded to the north and to the south by the Triassic–early Jurassic Rushan–Pshart and Tirich–Kilik sutures, respectively (Figure 1; e.g., Angiolini et al., 2013). During the Cretaceous, the South Pamir batholith intruded the Karakorum–South Pamir terranes during northward subduction of Neo-Tethys oceanic lithosphere to the south (e.g., Aminov et al., 2017; Chapman, Scoggin, et al., 2018). The Pamir differs from the adjacent Tibet orogen by its narrower N–S width, a northward-convex salient, intermediate-depth seismicity, greater Cenozoic internal shortening, and higher-magnitude exhumation expressed by Cenozoic gneiss domes that expose Asian crust (Hacker et al., 2017; Negrodo et al., 2007; Pegler & Das, 1998; Roecker, 1982; Sippl et al., 2013).

The Pamir gneiss-dome system comprises lower–middle-crustal rocks that were metamorphosed and exhumed during the Cenozoic and cover 20–30% of the surface exposure (Figure 1; Robinson et al., 2004; Schwab et al., 2004; Robinson et al., 2007; Schmidt et al., 2011; Stearns et al., 2013; Stübner, Ratschbacher, Rutte, et al., 2013; Smit et al., 2014; Stearns et al., 2015; Hacker et al., 2017; Rutte, Ratschbacher, Schneider, et al., 2017). The Central Pamir gneiss domes—Yazgulom, Sarez, Muskol, and Shatput—comprise an ~400 km-long, 5–40 km-wide belt (Rutte, Ratschbacher, Schneider, et al., 2017). The ~350-km-long and up to 100-km-wide Shakh dara and Alichur gneiss domes occupy the western and central South Pamir (Stübner, Ratschbacher, Rutte, et al., 2013). The ~70-km ~N–S trend of the Kongur Shan dome in the East Pamir (Robinson et al., 2004) contrasts with the approximately E–W trend of the central South Pamir domes. The ~E–W-trending Muztaghata dome in the East Pamir (Robinson et al., 2007) constitutes an overprinted, ~50-km-eastward extension of the Central Pamir domes. All domes are bounded by normal-sense shear zones and formed in a syn-collisional setting of 3–4 cm/yr ~N–S convergence between India and Asia (e.g., Molnar & Stock, 2009). With the exception of the Kongur Shan dome, extension was subparallel to convergence (~N–S). To explain the formation of the Sarez–Muskol–Shatput and the Shakh dara–Alichur domes, Stübner, Ratschbacher, Rutte, et al. (2013) and Rutte, Ratschbacher, Schneider, et al. (2017) proposed models of core-complex formation in an extensional tectonic setting within the broader India–Asia collision zone.

The tectonic setting of gneiss-dome formation in the Central and South Pamir—Neogene, syn-collisional, convergence-parallel extensional exhumation—contrasts with the neotectonic setting of the Pamir derived

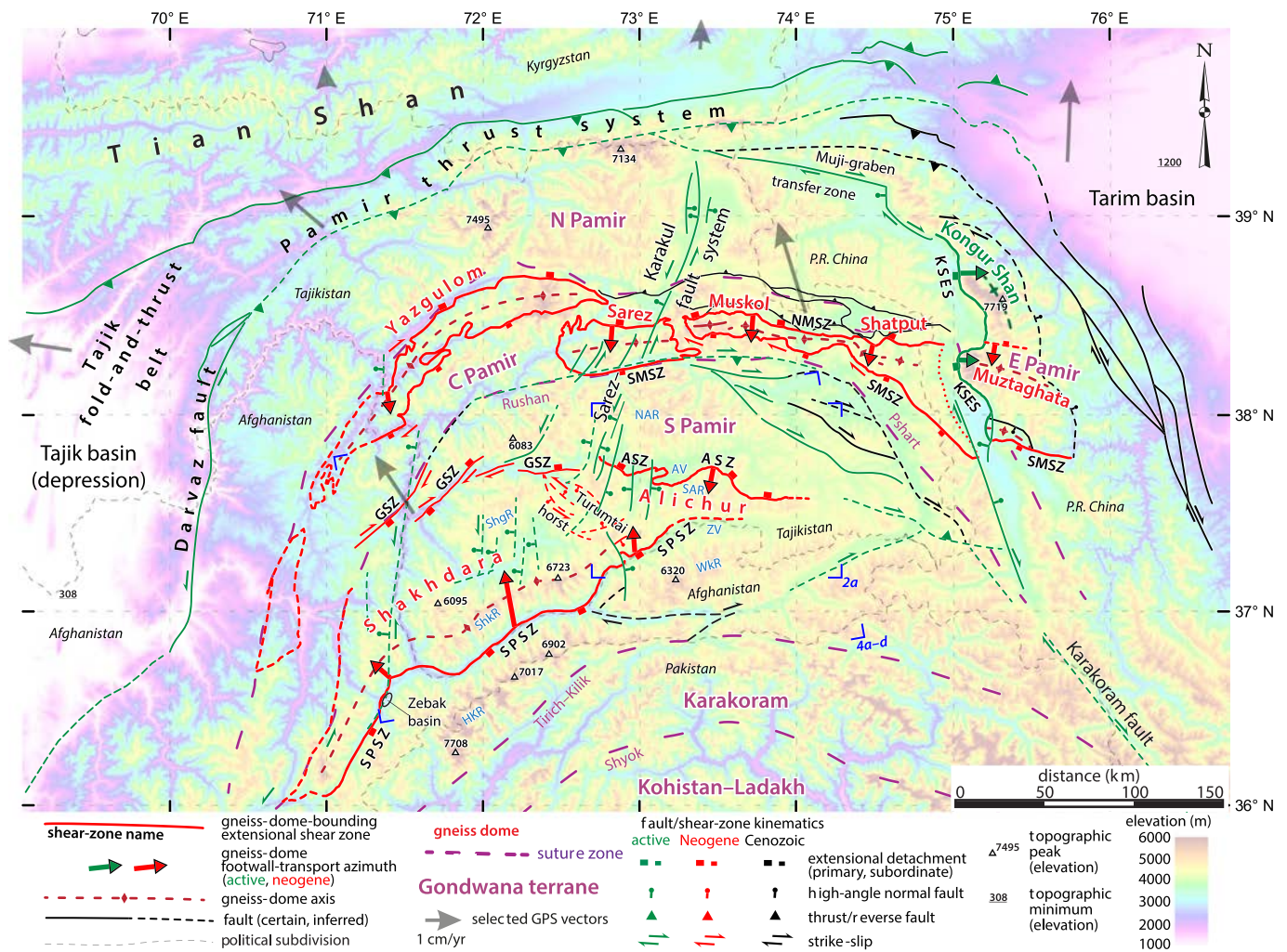


**Figure 1.** Tectonic map of the Pamir gneiss-dome system and major structures. Black and green arrows indicate dominant Neogene and active footwall-transport directions of dome-bounding, normal-sense shear zones. Locations of Figures 2a and 4a–4d outlined in blue. GPS vectors taken from Zubovich et al. (2010) and Ischuk et al. (2013). Dome-bounding shear zones: ASZ, Alichur shear zone; KSES, Kongur Shan extensional system; NMSZ, North Muskol shear zone; SMSZ, South Muskol shear zone; SPSZ, South Pamir shear zone. Mountain ranges: HKR, Hindu Kush range; NAR, Northern Alichur range; SAR, Southern Alichur range; ShgR, Shugnan range; ShkR, Shakhddara range; WkR, Wakhan Range. Valleys: AV, Alichur valley; ZV, Zorkul valley.

from geodesy, seismology, and neotectonic mapping (e.g., Ischuk et al., 2013; Jay et al., 2017; Kufner et al., 2018; Metzger et al., 2017; Schurr et al., 2014; Sippl et al., 2014; Zubovich et al., 2010). Currently, the Pamir east of the NNE-trending Sarez–Karakul fault system (SKFS; Figure 1) moves northward en bloc, with little internal deformation. At its northern boundary—the Pamir thrust system—high seismicity and focused shortening (13–19 mm/yr; Metzger et al., 2017, and references therein) reflect tectonic interaction with the Tian Shan orogen (Arrowsmith & Strecker, 1999; Coutand et al., 2002; Strecker et al., 2003), which is otherwise separated along strike from the Pamir–Tibet orogenic belt by cratonic basement (overlain by the Tarim and Tajik basins). The SKFS and its southwestward continuation into the Hindu Kush accommodate sinistral shear and ~E–W extension across the eastern and the western Pamir. The latter shows higher seismic deformation rates dominated by sinistral strike-slip faulting on NNE-striking or conjugate planes and normal faulting, indicating ~E–W extension coeval with ~N–S shortening. This deformation pattern suggests collapse of the western margin of the Pamir plateau and westward (lateral) extrusion of Pamir rocks into the Tajik-basin depression, which was shortened above an evaporitic décollement. This westward motion also occurs along the Pamir thrust system, in particular west of the area where the extension along the Kongur Shan extensional system (KSES) is transferred along the Muji-graben transfer zone into the frontal thrust system (Figure 1). The superposition of northward movement

and westward extrusion of the Pamir is reflected by rotation of GPS-derived surface velocity vectors from NNW (in the east) to WNW trending (in the west) (Ischuk et al., 2013; Zubovich et al., 2010).

This study employs geologic and structural mapping, fluid-inclusion analysis, and geo-thermochronology to investigate the Miocene exhumation of the Alichur dome—the eastern part of the Shakhdara–Alichur gneiss-dome complex. We show that footwall exhumation along the top-NNE, normal-sense, mylonitic–brittle ASZ post-dated leucogranite injection from 22–17 Ma and continued through sub-solidus temperatures (~410–130 °C) from 16–4 Ma. We specify the interaction of the Alichur-dome extensional system with that of the neighboring Shakhdara dome, tracing its southern boundary, the top-SSE South Pamir shear zone (SPSZ) eastward, detailing its timing and syn-extensional hanging-wall basin formation. We show that the longer-lasting, faster, and higher-magnitude exhumation of the kinematically linked Shakhdara dome along the SPSZ from 21–2 Ma reflects more significant tectonic exhumation than that of the Alichur dome along the ASZ. We elaborate on the Gunt shear zone (GSZ)—the northern boundary of the Shakhdara dome—which is connected to the ASZ via the Turumtai horst (the weakly extended relay bridge between the Shakhdara and Alichur domes). Integrating the data from the South and Central Pamir, we interpret the age progression of ~N–S extensional gneiss-dome exhumation from the Central Pamir to the South Pamir to reflect: (i) The predominantly northward, foreland-directed flow of hot crust into a cold foreland during the growth of the Pamir orocline; and (ii) The contrasting effect of basal shear related to underthrusting Indian lithosphere in enhancing extension in the underthrust South Pamir and inhibiting extension in the non-underthrust Central Pamir.

## 2. The Pamir Gneiss-Dome System

Although all Pamir domes were exhumed along normal-sense shear zones, there are differences (Figure 1; Robinson et al., 2004; Robinson et al., 2007; Stübner, Ratschbacher, Rutte, et al., 2013; Hacker et al., 2017; Rutte, Ratschbacher, Schneider, et al., 2017; this study). Whereas the Shakhdara–Alichur gneiss-dome complex is up to 90 km wide, the Central Pamir domes extend 5–40 km N–S; moreover, the latter show a pinch-and-swell geometry in map view, tapering and widening along strike. Another difference is the extension azimuth (Figure 1): that for the Central and South Pamir domes is roughly N–S; its convexity mirrors the moderate curvature of the Pamir orocline in its interior. The extension azimuth is ~E–W along the west-dipping KSES, which accommodated the exhumation of the Kongur Shan dome. The Muztaghata dome records both the earlier ~N–S extension of the Central Pamir domes and the later ~E–W extension along the KSES. Finally, there is a spatiotemporal difference in the timing and magnitude of exhumation. Whereas the Central Pamir domes and the East Pamir Muztaghata dome were exhumed between ~21–12 Ma from 25–35 km depth, the South Pamir domes were exhumed between ~21–2 Ma from 10–55 km. In the East Pamir, the onset of ~E–W extension along the active KSES at ~10 Ma exhumed the Kongur Shan dome and, due to a southward decrease in slip magnitude, augmented the earlier, ~N–S-extension-related exhumation of the Muztaghata dome (Arnaud et al., 1993; Brunel et al., 1994; Cai et al., 2017; Cao, Wang, et al., 2013; Robinson et al., 2004; Robinson et al., 2010; Thiede et al., 2013). Bedrock retrograde-metamorphic and/or cooling ages (Brunel et al., 1994; Cao, Bernet, et al., 2013; Hacker et al., 2017; Hubbard et al., 1999; Robinson et al., 2007; Rutte, Ratschbacher, Khan, et al., 2017; Stearns et al., 2013; Stearns et al., 2015), which are consistent with the broader signal from detrital cooling ages (Cao, Bernet, et al., 2013; Carrapa et al., 2014; Lukens et al., 2012), indicate southward propagation of convergence-parallel gneiss-dome exhumation from the Central to the South Pamir. This was followed by cross-cutting, orogen-parallel (~E–W) gneiss-dome exhumation along the KSES and the SKFS.

Previous investigations by our group (Hacker et al., 2017; Rutte, Ratschbacher, Khan, et al., 2017; Rutte, Ratschbacher, Schneider, et al., 2017; Schmidt et al., 2011; Stearns et al., 2013; Stearns et al., 2015; Stübner, Ratschbacher, Weise, et al., 2013) interpreted structural, petrologic, and geothermochronologic data for the Pamir gneiss domes within the framework of published numerical modeling results of channel flow in orogenic plateaus (Rey et al., 2010) to propose that the domes were exhumed during a Neogene stage of crustal thinning under dominant ~N–S and minor ~E–W extension. Rey et al.'s (2010) modeling showed that low channel buoyancy, a small melt fraction, and a strong foreland upper crust favor foreland-directed channel flow extrusion beneath a plateau; in contrast, high channel buoyancy, a large melt fraction, and a weak foreland upper crust favor coupling between extensional gneiss-dome exhumation within the

plateau and shortening in the foreland. Additionally, their models demonstrate that thinning due to material flow out of the plateau together with isostasy exhumed the plateau ductile crust. We envisioned that exhumation of the Central and South Pamir crust started at ~21 Ma in a lower–middle-crustal channel; in this early stage, the Pamir crust was probably flowing toward its northern and western forelands. Indian slab breakoff at 25–20 Ma (Hacker et al., 2017; Mahéo et al., 2002; Rolland et al., 2001; Rutte, Ratschbacher, Khan, et al., 2017; Stearns et al., 2015) changed the channel properties. The heat input and the regional migmatization documented in the exposed South and Central Pamir lower–middle crust inhibited channel flow due to increased buoyancy and melt fraction that thermally weakened the channel rocks, favoring core-complex formation in the Pamir plateau (Rey et al., 2010), expressed in the gneiss domes. The collapse of the Pamir crust and the gneiss-dome exhumation from ~21 Ma onward relocated the deformation front from the Central Pamir to the North Pamir, likely facilitated by the activation of the Jurassic evaporite décollement that characterizes wide parts of the Tajik-depression foreland basin (Nikolaev, 2002). Although the extension terminated within a few million years in the Central Pamir domes due to their foreland position, it continued longer in the hotter South Pamir crust. The temperature difference between the Central and South Pamir persists today, with the South Pamir showing much higher electrical conductivity (Sass et al., 2014).

Dextral-transpressive (and minor dextral-transensional) deformation throughout the Pamir (Rutte, Ratschbacher, Schneider, et al., 2017; Stübner, Ratschbacher, Rutte, et al., 2013) accommodated westward lateral extrusion of the Pamir plateau prior, during, and after the ~N–S extensional exhumation of the Pamir domes (Figure 1). This is reflected in the Central and Southeast Pamir by: (i) Evidence of E–W stretching coeval with prograde metamorphism in the dome interiors; (ii) Syn-extensional dextral shear along the dome-bounding shear zones before ~12 Ma; (iii) Post-extensional resumption of crustal thickening, that is, buckling of the Central Pamir domes, and dextral-reverse-shear reactivation of their bounding shear zones after ~12 Ma; (iv) ~S-vergent thrusting-folding north of the domes in the Trans-Muskol and North Sarez–Muskol–Shatput transpressional belts; and (v) Active, mostly ~N-vergent thrusting-folding and dextral wrenching south of the domes in the Murghab–Aksu–Southeast Pamir thrust-wrench belt since ~16 Ma (Rutte, Ratschbacher, Khan, et al., 2017; Rutte, Ratschbacher, Schneider, et al., 2017; Schurr et al., 2014; Strecker et al., 1995) that reactivated Cretaceous shortening in the South Pamir thrust belt (Chapman, Robinson, et al., 2018). The clearest expressions of dextral-transpressive deformation in the South Pamir occur in: (i) The GSZ, where it overprinted early, top-N normal shear after ~21 Ma; and (ii) The Wakhan corridor, where it is not dated (Stübner, Ratschbacher, Rutte, 2013; Stübner, Ratschbacher, Weise, et al., 2013). The active, Sarez–Murghab thrust system (Schurr et al., 2014) may link the Murghab–Aksu–Southeast Pamir thrust-wrench belt to the western strands of the GSZ. Taken together with Paleogene approximately E–W stretching and Neogene approximately E–W boudinage documented in the Central Pamir domes (Rutte, Ratschbacher, Schneider, et al., 2017), dextral-transpressive deformation in the South–Central Pamir appears to reflect long-lived ~E–W extension that accommodated westward lateral extrusion during the growth and collapse of the Pamir plateau.

### 3. Geology of the Alichur-Dome Region

The Shakhdara–Alichur gneiss-dome complex encompasses an ~350 km E-to-W increase in topographic relief that broadly correlates with an increase in exhumation depths from 10–20 km for the Alichur dome to 30–55 km for the Shakhdara dome (Figures 1 and 2a) (Hacker et al., 2017; Stübner, Ratschbacher, Rutte, et al., 2013). Whereas the top-S SPSZ bounds both domes to the south, the top-N ASZ only bounds the Alichur dome to the north. The ASZ projects westward along strike into the GSZ, which bounds the Shakhdara dome to the north. The Turumtai horst is a low-strain relay bridge between the Shakhdara and Alichur domes that kinematically links the high-strain extensional provinces of the gneiss-dome complex.

Our constraints for shear zone/fault kinematics include s-c fabrics, feldspar  $\sigma$  and  $\delta$  clasts, asymmetric folds, mica fish, subsidiary fractures, tension gashes, and slickenfibers. We also infer map-scale fault kinematics and folds based on map relationships and topographic lineaments (Figure 2a). Stereonets (Figure S1 in the supporting information) depict the structural measurements for both individual and grouped stations with consistent data. Photomicrographs of ASZ and SPSZ samples (Figure S2) highlight microstructures

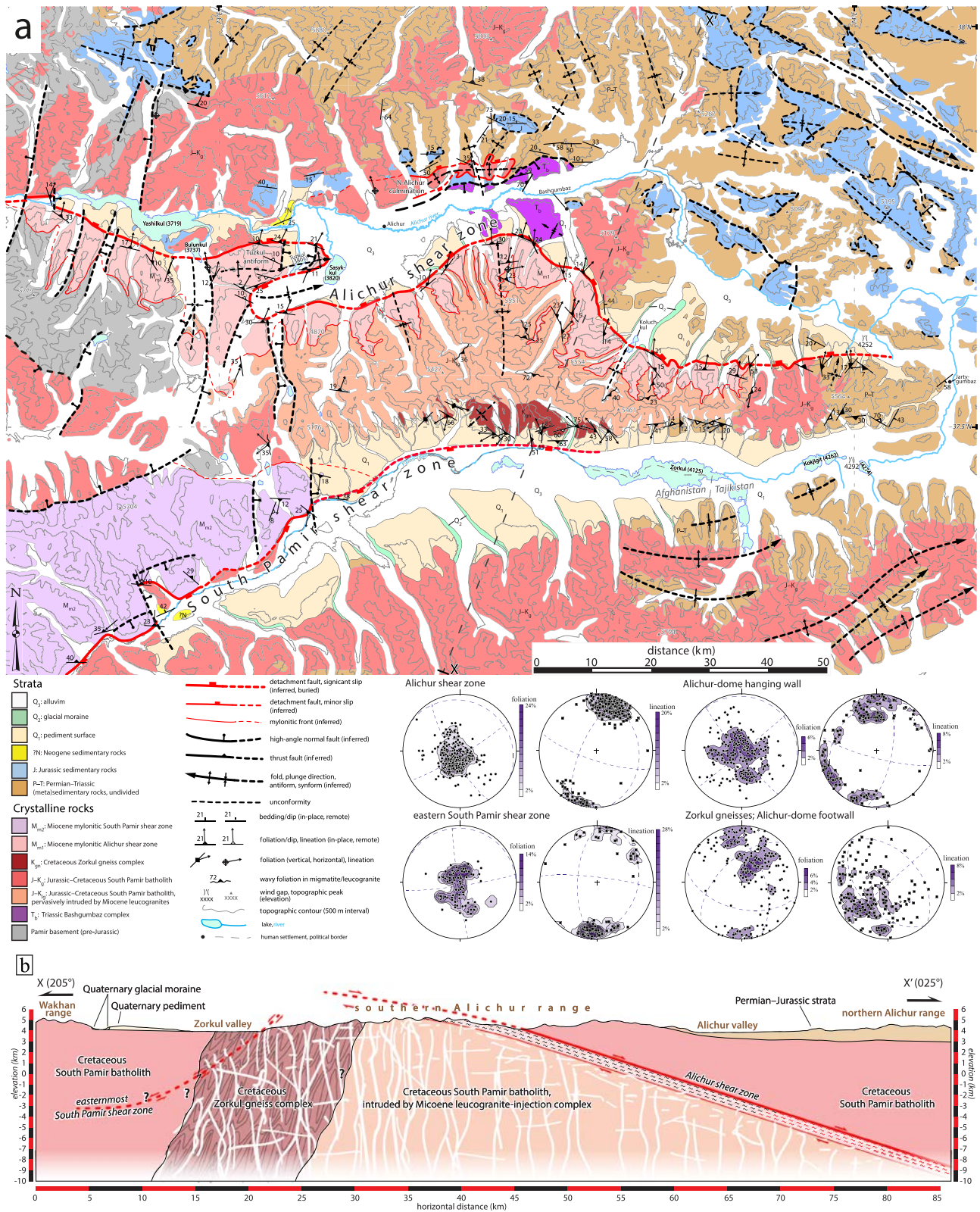


**Figure 2.** (a) Geologic map of the Alichur dome, based on Yushin et al. (1964), Stübner, Ratschbacher, Rutte, et al. (2013), and our mapping. 500 m contour interval. Stereonets show compiled structural data from all stations for all major tectonic domains. (b) Strike-normal cross section transecting the Alichur dome. Location of cross section shown in Figure 2a.

that illustrate kinematics and deformation temperatures, which are discussed in Text S1 (Cole et al., 2007; Law, 2014; Passchier & Trouw, 2005; Stipp et al., 2002; Stübner, Ratschbacher, Rutte, et al., 2013). Mapping and measurements of *c*-planes define the outcrop-scale orientation of the ASZ. Figure 2b provides a strike-normal section across the Alichur dome. Mineral-name abbreviations follow Whitney and Evans (2010).

### 3.1. Topographic Trends

The Alichur region is part of the high-elevation, low-relief Pamir plateau (Figure 1). Increasing erosional base levels from ~3,700 m near Lake Yashilkul (in the west) to ~4,100 m near colongitudinal wind gaps at 74°E (in the east) correlate with an eastward decrease in relief from ~2,100 to ~1,300 m (Figure 2a). The wind gaps are located in basins north and south of the Alichur range, near the eastern terminus of the ASZ (4252 m) and east of Lake Kokjigit (4,292 m) (Figures 2a). Gently dipping pediment surfaces ( $Q_1$ ) with average slopes of 4–10° are common in the proximal hanging wall of the ASZ (left bank of the Alichur valley) and on both sides of the Zorkul valley. Glacial moraines ( $Q_2$ ) emanating from U-shaped, glacially carved valleys cut the pediments and broadly define elevation differences between the pediments and the modern alluvium surface ( $Q_3$ ) (Figures 2a, 3a, and 3b).

### 3.2. Alichur Shear Zone (ASZ)

The ASZ ( $M_{m1}$  in Figures 2a, 3a, and 3b) dips 15–25° NNE with a ~020° trending stretching lineation. It is 0.7–1.0 km thick, based on its map distribution and ~20° dip. The Alichur detachment comprises the brittle, uppermost structural level of the ASZ, but we consider the ASZ to encompass all faults and shear zones that bound the Alichur dome to the north. The lithology of the ASZ comprises non-coaxially sheared, mylonitized Bt ± Wm granitoids and leucogranites that exhibit brittle chloritic breccia overprint along the Alichur detachment. Ductile deformation of Qz and brittle–ductile deformation of Fsp indicate mylonitic deformation temperatures of 300–450 °C (“low-temperature Qz plasticity” of Stübner, Ratschbacher, Rutte, et al., 2013). Obliquity between average *s*- and *c*-plane dip directions indicates minor strike-slip components of non-plane-strain deformation (Figure S1). Protomylonite, mylonite, and ultramylonite domains are common throughout the ASZ (Figure S2); protomylonites dominate at the lowermost structural level where the ASZ transitions into non-mylonitic Alichur-dome rocks. Variably mylonitized, 1 cm- to 1 m-thick, foliation-parallel leucogranite sheets are widespread throughout the ASZ (Figures 3c and 3d).

The Alichur detachment is exposed at the western extremity of Lake Yashilkul in the footwall of a cross-cutting, west-dipping, high-angle normal fault (Station J3710B; Figures 2a, 3e, and S1). Here, the uppermost 10 m of the ASZ are hydrothermally altered to bright orange, not lineated, and exhibit a relict, 15–35°N–NW-dipping foliation. This section transitions downward into >50 m-thick chloritic breccia with a 10–20°E-dipping foliation. The ~20 km strike length of the ASZ south of Lake Yashilkul is planar, with a N–NNE dipping foliation and a NNE-trending stretching lineation (Stations 9917D, J3710A, and J4711B; Figures 2a, S1, and S2). Subvertical joint sets formed both perpendicular and parallel to the stretching lineation (Station J4711B).

The open, gently east-plunging Tuzkul antiform in the ASZ defines a topographic edifice spanning ~15 km E–W between the Bulunkul and Sasykkul lakes (Figures 2a and 3f). Foliations dip 0–25° away from the antiform crest. Irrespective of the variations in the foliation, the stretching lineation trends NNE and the shear sense is top-NNE, except at Station 9918C, which shows an additional NW-trending lineation and top-NW kinematics (Figure S2). The antiform is cut by ~N-striking, high-angle normal faults (Stations 9915A, 9918C, J4707B–D/G–H; and J3628A; Figure S1). We infer that a buried synform southeast of the Tuzkul antiform accounts for the north dip of the ASZ to the southeast.

The remaining ~80 km of strike length of the ASZ to the east is corrugated by open, ~N-plunging, antiforms and synforms of 20–40 km wavelength (Figure 2a). The stretching-lineation azimuths show a narrow NNE range; the wider range of foliation strikes traces the long-wavelength corrugations. Secondary, moderately S–SW-dipping shear zones with SSW–SE-trending lineations occur along the major antiform axis (Stations 9914B and 9914C) and its eastern limb (9912B, 9912C, 9913C, and 9913D; Figures S1 and S2). The ASZ continues ~25 km east past the easternmost occurrence of mylonitic rocks as a fault zone. The elevation of the ASZ monotonically increases southward as a consequence of its planar and northward dip.

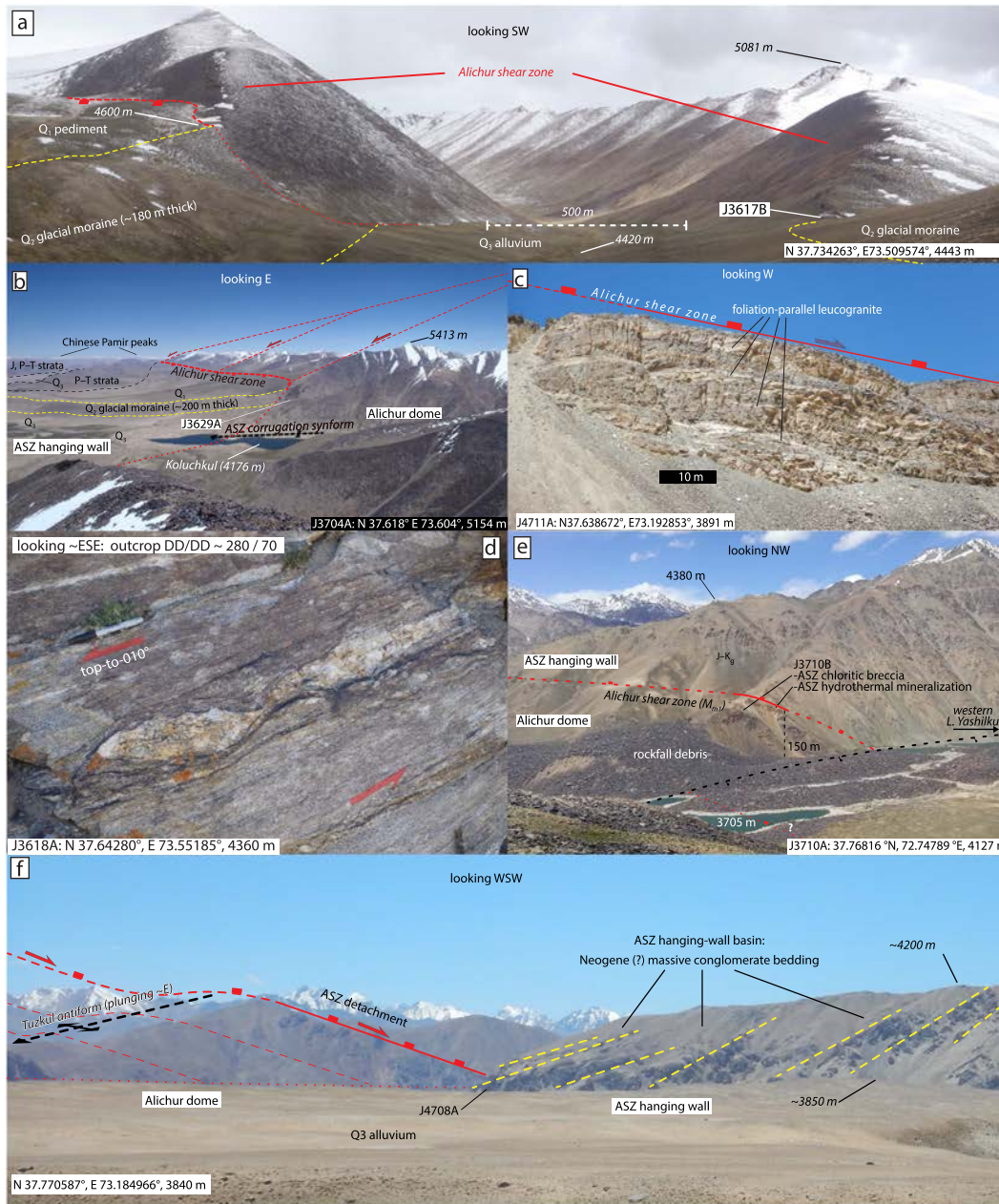


**Figure 3.** Interpreted field photos of the Alichur region. (a) Strike-normal view of the Alichur shear zone (ASZ), contextualizing geologic and geomorphic units. (b) Strike-subparallel view of the ASZ, highlighting synformal corrugation. (c) Typical mylonitic orthogneisses and foliation-parallel leucogranite sills in the ASZ. (d) Typical non-coaxially deformed leucogranite in the ASZ with top-NNE kinematics. (e) View of the hydrothermally altered top of the Alichur detachment, offset by an east dipping, high-angle normal fault. (f) View of the east plunging, open Tuzkul antiform in the ASZ (left) and a Neogene(?) syn-extensional basin in its hanging wall. (g) Typical outcrop of discordant leucogranite dikes in the core of the Alichur dome. (h) Steep cliff face showing >50% leucogranite enveloping Jurassic-Cretaceous country rocks in the core of the Alichur dome. (i) Apparent south-vergent leucogranite flow in the proximal footwall of the ASZ. (j) Typical cross-cutting relationship in the Alichur dome: ~20 Ma leucogranite dike cutting ~102 Ma migmatite. (k) Typical crosscutting relationship in the Alichur dome: ~22 Ma leucogranite intruding ~110 Ma granodiorite. (l) Asymmetric folds in the Cretaceous Zorkul-gneiss complex. (m) Isoclinal folds in the Cretaceous Zorkul-gneiss complex. (n) High-angle normal faults within the hanging wall of the ASZ, juxtaposing the Triassic Bashgumbaz complex in the hanging wall against Permian-Triassic strata in the footwall. (o) Intrusive contact between Jurassic-Cretaceous granitoids and the Permian-Triassic Wakhan formation. Inset highlights quartz-rich intervals that typify the Wakhan formation. (p) Strong flattening strain in the Wakhan formation (~E-W maximum principal stretch), where it is intruded by likely Jurassic-Cretaceous granite. (q) Rounded granitic clasts in massive, south dipping, Neogene(?) conglomerate beds in the ASZ hanging wall. (r) High-strain, high-temperature central South Pamir shear zone (SPSZ). (s) Low-strain, low-temperature eastern South Pamir shear zone. (t) Neogene(?) conglomerate strata in the hanging wall of the central eastern SPSZ, highlighting matrix-supported granitic clasts and fining-upward sequences. (u) Neogene(?) conglomerate strata in the hanging wall of the easternmost SPSZ, highlighting volcanic and foliated-gneiss clasts.

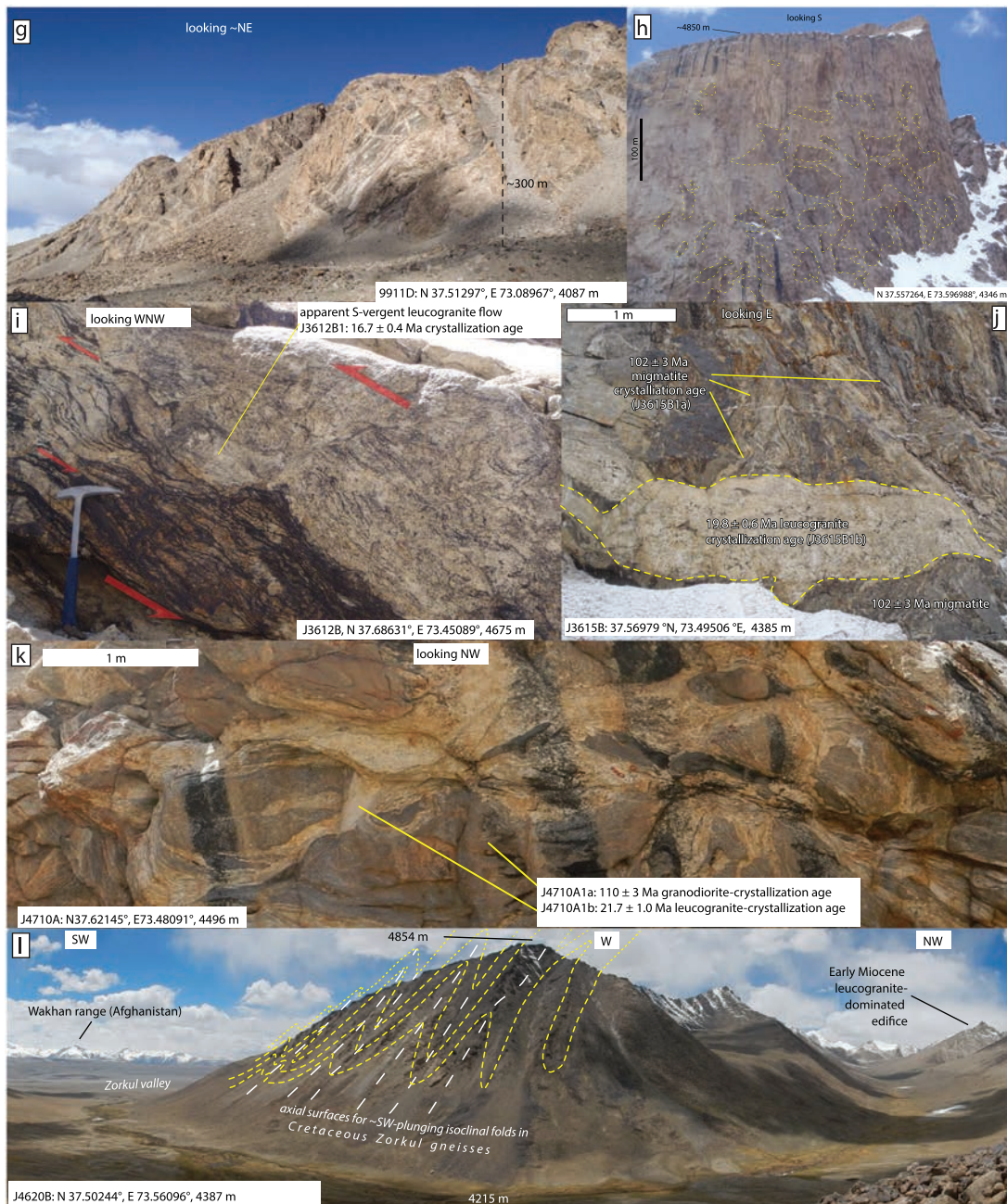


Figure 3. (continued)

### 3.3. Alichur Dome

The footwall of the ASZ comprises Cretaceous granitoids and associated migmatites (Stübner, Ratschbacher, Rutte, et al., 2013; Stübner, Ratschbacher, Weise, et al., 2013; Vlasov et al., 1991; Yushin et al., 1964); the latter are restricted to the southern core of the dome (Figure 2a). The footwall is intruded by an early Miocene (zircon U–Pb data, section 6.1) leucogranite-injection complex that transitions from ASZ-subparallel sheets in the north (Figure 3c) into increasingly randomly oriented, cm- to m-scale dikes and sills in the south (Figure 3g). The leucogranite-volume fraction and degree of injection-complex connectivity also increase southward toward the dome core, where equal or greater amounts of leucogranite relative to the cross-cut granitoids surround and envelop the country rocks (Figure 3h). The pegmatitic and aplitic leucogranites contain Tur + Ms + Grt. They exhibit substantial textural variability, ranging from mylonitic in the ASZ

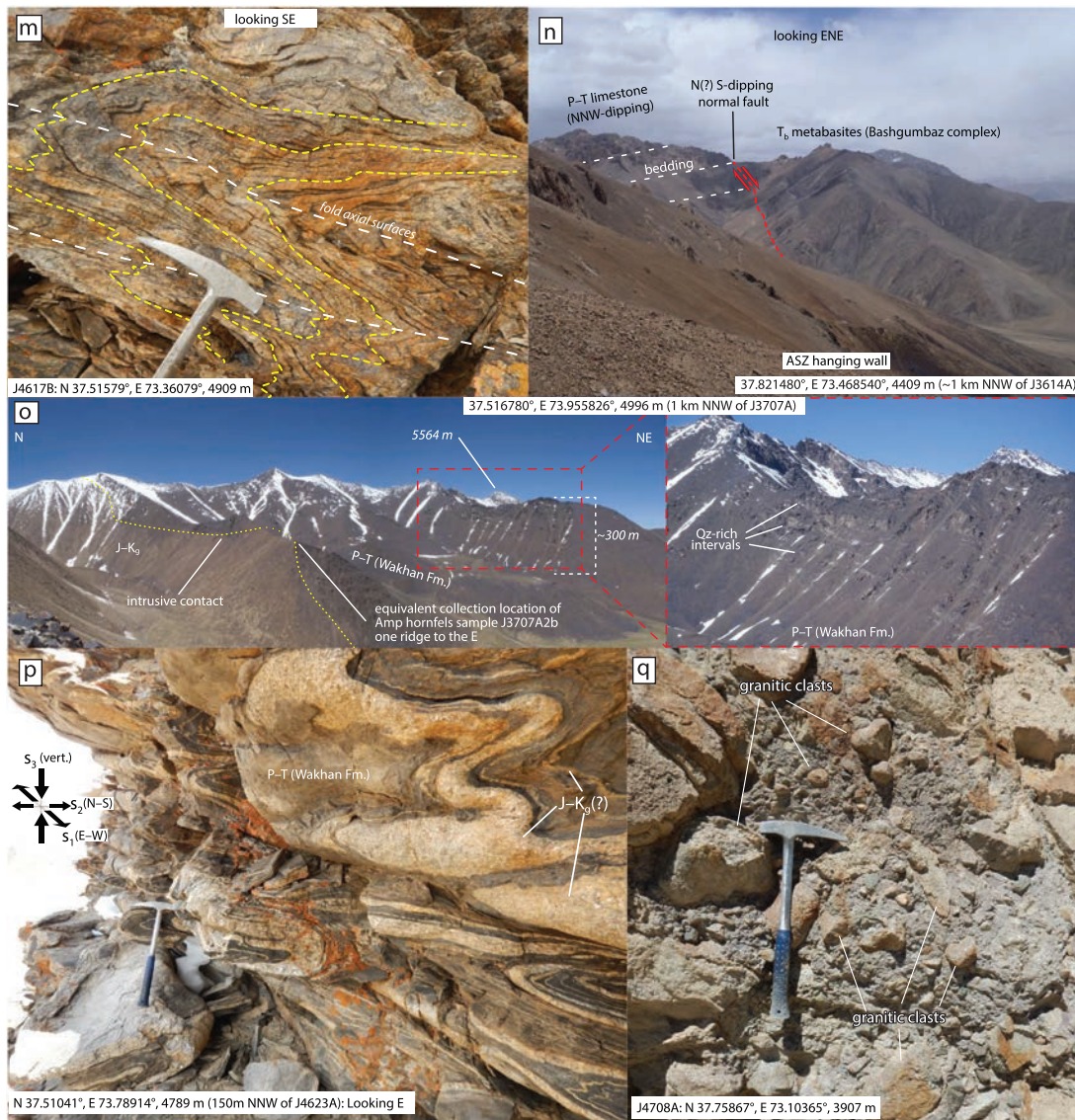


Figure 3. (continued)

to isotropic or sub-supra-solidus flow fabrics away from the ASZ and magmatic-flow textures in the dome core. Partial-melt flow asymmetry highlighted by Bt schlieren indicates leucogranite injection in a deviatoric stress field, with flow fabrics commonly exhibiting south-vergent, apparent-thrust-sense kinematics (Figure 3i). Cross-cutting relationships between the injection-complex leucogranites and Cretaceous migmatite (Figure 3j) and granodiorite (Figure 3k) are exemplified at Stations J3615B and J4710A; the migmatite is commonly ptygmatically folded and displays a wavy foliation with scattered lineation trends (Figure S1).

The Zorkul gneisses ( $K_{gn}$ ), exposed in the southernmost Alichur dome, comprise nonmylonitic Bt orthogneiss, with rare migmatite and paragneiss intervals that contain Grt + Sil. Foliations are scattered and generally dip gently steeply WSW–SE, with broadly SW-trending stretching lineations. Poles to foliations form a weakly defined, ENE dipping girdle, which, taken together with the lineations, suggests folding about a SW-plunging axis (Figures 2a and S1). Observations of Zorkul-gneiss foliation orientations from >1 km distance indicate asymmetric, tight folds with steeply SE-dipping axial planes and SW-plunging hinge lines (e.g., Station J4620B; Figure 3l). Outcrop-scale observations indicate orthogonally oriented isoclinal folds with SE-plunging hinge lines (e.g., Station J4617B; Figure 3m). False-color contrasts in Landsat images

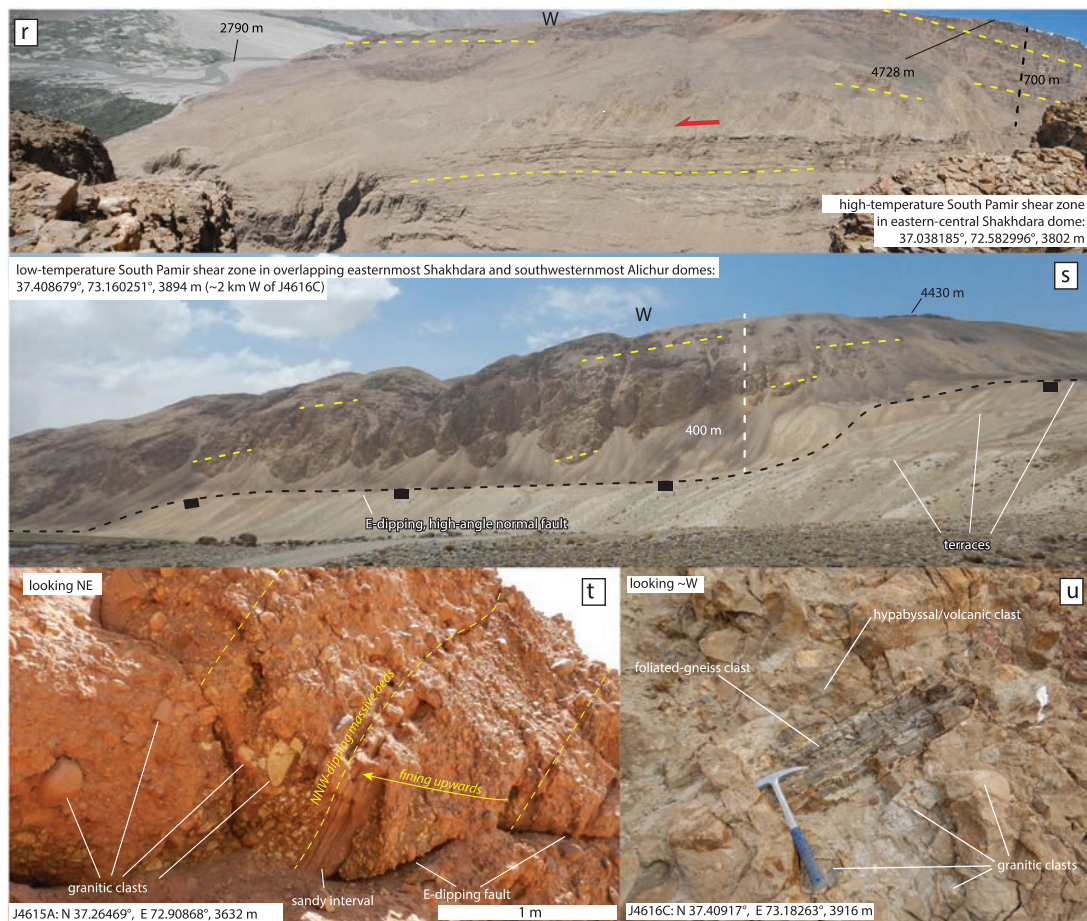


Figure 3. (continued)

indicate that the contact between the Zorkul gneisses ( $K_{gn}$ ) and the Alichur-dome units to the north ( $JK_{lg}$ ; Figure 2a) is transitional over  $\sim 5$  km.

### 3.4. Alichur Shear Zone Hanging Wall and Eastern Alichur and Zorkul Valleys

The ASZ hanging wall comprises the Triassic Bashgumbaz complex ( $T_b$ ), Permian–Triassic flysch (P–T), unconformably overlying Jurassic strata (J), Jurassic–Cretaceous granitoids (J– $K_g$ ), and minor Neogene(?) hanging wall basin strata (Figure 2a). The Triassic Bashgumbaz mafic complex (Zanchetta et al., 2018; this study) is bounded to the south by the ASZ and to the north by a south-dipping, high-angle normal fault (Figures 2a and 3n). The flysch succession (Angiolini et al., 2013; Angiolini et al., 2015), which is also exposed in the eastern Alichur and Zorkul valleys, comprises fine–medium-grained clastic and carbonate strata (Figure 3o). Deformation is reflected by open–tight folds, faults, and foliations with scattered lineations defined by Bt and/or And. The distributions of Permian and Triassic strata in the 1:200,000 maps (Yushin et al., 1964) indicate folding about NE- and NNW-trending axes (Figure 2a). The strata are metamorphosed up to Chl grade and intruded by J– $K_g$  granitoids, which have  $<1$  km-wide contact aureoles. Amp in hornfels J3707A2b, collected within 20 m of the intrusive contact (Figure 3o), indicates amphibolite-facies temperatures for the innermost contact aureole. Greenschist-facies domains with late, randomly oriented, cm-scale And porphyroblasts grown over a clay-mineral matrix with relict sedimentary structures define the majority of the contact aureole. Within a contact aureole near Station J4623A, the P–T strata and cross-cutting granitic dikes are isoclinally folded with subhorizontal axial surfaces (Figure 3p).

Red conglomerate, sandstone, and carbonate of the Jurassic Darbasatash and Gurumdi Groups unconformably overlie and are less deformed than the P–T rocks (Figure 2a; Dronov et al., 2006; Angiolini et al., 2013;

Villareal et al., 2017). Jurassic–Cretaceous granitoids (J–K<sub>g</sub>) intrude the hanging wall strata and the Bashgumbaz complex and are, in general, not deformed. Protomylonites with subhorizontal foliations, east-trending lineations, and brittle–ductile faults indicating both E–W and N–S extension occur in a basement culmination, here called the N-Alichur culmination, north of the Bashgumbaz complex (Stations 0909A–0909C; Figures 2a and S1). The N-Alichur culmination formed during localized Wm recrystallization, Bt to Chl retrogression, and across the transition from ductile to brittle Qz deformation. The map pattern and the lack of a contact aureole in the adjacent Permian to Jurassic strata indicate that these rocks are bounded by a low-angle normal fault. Neogene(?) (Yushin et al., 1964) conglomerates crop out ~2 km north of the Tuzkul antiform (Station J4708A; Figures 2a, 3f, 3q, and S1); they are massive, generally clast-supported, and contain well-rounded, pebble–boulder-sized granitoid clasts (likely J–K<sub>g</sub>) and minor, angular, pebbly (meta)sedimentary clasts (likely P–T and/or J) (Figure 3q). The SSW dip of the bedding decreases to the south toward the ASZ (Figure 3f).

### 3.5. Eastern South Pamir Shear Zone (SPSZ)

The SPSZ (Figures 1 and 2) bounds the Shakh dara dome to the SSE. Compared to the ASZ, it is thicker ( $\leq 4$  km), exhumed footwall rocks from deeper crustal levels (20–55 km), and was subjected to higher maximum deformation temperatures ( $\geq 750$  °C; Stübner, Ratschbacher, Rutte, et al., 2013; Hacker et al., 2017). Deformation temperatures decrease from Sil-grade and migmatitic tectonites in the central SPSZ along strike to the west and east. The eastward decrease is illustrated by a transition from the easternmost occurrence of syn-kinematic Sil for SPSZ mylonite Sample J4615D1 (~6 km SSE of Station J4615B), to greenschist-facies deformation for the easternmost SPSZ mylonites (Stations J4709A, J4616B, and J4621C) and exclusively brittle deformation in the northern Zorkul valley (Figures S1 and S2). The eastern SPSZ ( $M_{m2}$  in Figure 2a) dips atypically NNW–N at the southwestern corner of our map area, which we attribute to back-rotation by late, brittle, high-angle, strike-parallel normal faults within the SPSZ (Stations 9910B–9910D, 9911A, J4615B, and J4646A; Figure S1). Along this ~20-km segment of the SPSZ, kinematic indicators with NW-plunging stretching lineations exhibit top-S kinematics. The SPSZ is offset ~6 km in an apparent left-lateral sense by an active (Schurr et al., 2014), ENE-dipping, high-angle normal fault near Station J4615B.

Deformation of the easternmost mylonitic rocks of the SPSZ is ductile for Qz but not Fsp (Figure S2); weakly defined foliations and lineations indicate low strain. The foliations dip SW–S and the stretching lineations trend SSW. S-c relationships observed at stations J4621C and J4709A, as well as white-mica fish for mylonitized leucogranite J4621C2, indicate top-S sense of shear. We infer a buried, brittle extension of the SPSZ ~40 km eastward along strike as far as the western shore of Lake Zorkul (Figure 2a). This inference is motivated by the notion that the ~300 km-long SPSZ must extend along-strike for tens of km before its brittle, low-strain extremity tips out. Figures 3r and 3s highlight the contrasting character of the SPSZ in the Shakh dara- vs. Alichur-dome regions. The SPSZ is much thicker in the former and exhibits its mylonitic foliation, consistent with high deformation temperatures and strain (Figure 3r); the SPSZ in the latter shows a poorly defined foliation, indicating lower deformation temperatures and strain (Figure 3s).

### 3.6. Eastern Shakh dara-Dome Hanging Wall

We investigated the hanging wall of the eastern Shakh dara dome at two locations separated by ~30 km along strike; they feature small ( $< 0.3$  km<sup>2</sup>) exposures of N-dipping sedimentary-basin strata that were tentatively assigned a late Paleogene depositional age (Figures 2a and S1; Stations J4615A and J4616C; Yushin et al., 1964). Station J4615A (to the west) is in the hanging walls of both the SPSZ and a younger, ENE-dipping normal fault. The strata comprise ~40° NNW-dipping, massive red beds of clast-supported pebble–cobble conglomerate with randomly oriented, well-rounded granitic clasts and rare sandy intervals (Figure 3t). An ~25° E-dipping, minor fault cuts the conglomerate beds (Figure S1); both bedding and the shallow fault dip imply rotation of the strata in the hanging wall of the SPSZ. Station J4616C (to the east) is located ~4 km east of the easternmost mapped mylonites in the hanging wall of the brittle SPSZ (Figures 2a and S1). The massive pebble–boulder conglomerate beds dip ~40° N and contain poorly sorted clasts of well-rounded granite, hypabyssal/volcanic rocks, and rare non-mylonitic Bt gneiss (Figure 3u); interspersed are medium–coarse-grained sandstones. Matrix-supported conglomerates are more common than clast-supported ones. Minor, normal-oblique, top-NNW faults and steeply N- and W-dipping joints record extension (Figure S1).

The N dip of strata in both hanging-wall basins indicate deposition prior to or coeval with top-S slip along the SPSZ. The abundance of granitoid and hypabyssal/volcanic clasts suggests derivation from upper–middle-crustal levels. Whereas the granitoid clasts resemble the South Pamir batholith, the gneiss clasts resemble the Zorkul gneisses. The rocks and structures of these basin relicts resemble the lower syn-extensional deposits of the larger ( $\sim 15 \times 1$  km) Zebak basin of the southwestern SPSZ hanging wall along strike in Badakhshan, Afghanistan (Figure 1; Desio, 1975; Stübner, Ratschbacher, Rutte, et al., 2013; section 6.5). The clasts of the pre-extensional and lower syn-extensional deposits of the Zebak basin contain  $>50\%$  hornfels,  $\sim 15\%$  granitoids, 5% volcanic rocks, and  $<30\%$  quartzite and graphitic metapelite; there are no gneisses or mylonites. These rocks signify derivation from the highest levels of a magmatic-arc sequence, possibly the South Pamir batholith, and part of its roof, likely the commonly graphitic Permian–Triassic Wakhan formation. In contrast, the  $<1$  m (diameter) clasts of the majority of the syn-extensional deposits include  $\sim 70\%$  orthogneiss, partly with cross-cutting leucogranite dikes, non-deformed two-mica leucogranite, and mylonites. The syn-extensional clasts are identical to those exhumed in the Shakh dara-dome footwall.

### 3.7. The Gunt Shear Zone (GSZ) and the Turumtai Host

The GSZ remains incompletely studied due its limited accessibility. Here, we extend Stübner, Ratschbacher, Rutte, et al.'s (2013) Stübner, Ratschbacher, Weise, et al. (2013) study by adding structural data from its westernmost segment and new thermochronologic data (section 6.3). Figure S1 provides an updated map of the GSZ area and summarizes the available structural data. The structural complexity of the GSZ arises from its transitional position between the generally openly folded, rigid Shakh dara-dome gneisses and granitoids of the Shugnan range in the south and the tightly isoclinally folded, rheologically weaker Permian–Triassic metasedimentary rocks in the north (Figures 1 and S1); the latter—intruded by mostly Cretaceous granitoids (Vlasov et al., 1991)—are equivalents of the Permian–Triassic strata north of the Alichur dome. The South Pamir batholith of the eastern Shugnan range is intruded by a dike complex resembling that of the Alichur dome.

Stübner, Ratschbacher, Rutte, et al. (2013) described the GSZ as a segmented shear/fault zone with, in general, a prominent subvertical, E(NE)-striking, dextral shear fabric. This formed in an early stage as gently dipping shear zones with normal-shear kinematics. Folding, identical to that north of the Shakh dara dome, rotated this early normal-shear fabric into a subvertical position. Ongoing deformation preferentially accentuated steep fold limb sections under dextral shear. Late-stage normal shear/fault zones cut all structures. Deformation temperatures— $350$ – $500$  °C—resemble those of the ASZ. The fold tightness changes from west to east along the different segments of the GSZ. It is most pronounced along the central section of the western GSZ, whereas its eastern segment—in crystalline basement rocks and granitoids—generally features open folds (Figure S1). The following description, mainly based on Stübner, Ratschbacher, Rutte, et al. (2013), outlines key segments of the GSZ, and provides a basis for interpreting the expanded radio-isotopic-age database.

We mapped a western segment of the GSZ in Afghanistan (Figure S1). There, foliation, c-planes, and shear bands in Kfs and Tur + Bt + Wm  $\pm$  Grt gneisses dip  $\sim 60^\circ$  SE (Stations 13910A and 13910B); Qz-rich layers in the leucogranites were mylonitized at low temperature (Qz-ductile and Fsp-brittle). This segment extends eastward along strike into Tajikistan, where similar pegmatitic and leucogranitic gneisses intruded Triassic shales (Station 6905C). It is unclear whether the top-SSW dextral-normal fabric has been rotated from its primary orientation; a possibly initially shallower foliation would imply normal shear zones with an  $\sim 200^\circ$  extension azimuth.

Another segment—here called the western GSZ—is accessible along the lower Gunt river and its tributaries. Stations 1191A and 1192A in Bt + Ms + Grt gneiss, schist, and pegmatite dikes show flexure-type shear zones with ductile Qz. The kinematics are dextral-normal along SSE dipping planes. Deformation at Station 1192B is exceptional as it progressed from high-temperature ductility to cataclastic. The early fabric is associated with mylonite layers in Qz + Fsp + Tur pegmatite and adjacent Bt + Sil + Grt schist. This fabric shares the top-SSW kinematics of stations 1191A and 1192A but has  $\sim$ W-dipping foliation and shear bands with sinistral-normal slip; the low-temperature fabric is purely normal. Stations 1192C, 6904M–6904Q, 6905A, 6905B, and 4727C (Figure S1) cover the width of this segment; here, the shear zone is subvertical. Most of the section is in homogeneously deformed orthogneisses with Bt + Qz-ductile and Fsp-brittle dextral-shear fabrics. A weak foliation and a pervasive lineation outline L-tectonites, that is, constrictional

strain as result of vertical and horizontal shortening. At Stations 6905A, 6905B, and 4727C, the low-temperature fabric is tightly isoclinally folded along stretching-lineation-parallel axes; the axial planes are again folded. Here, unfolding of the early-formed fabric indicates top-SW normal-shear kinematics. In a later stage, dextral shear bands overprinted and accentuated the fold limbs. Segregation or late aplitic dikelets, intruded along the foliation, are strongly sheared; both dikelets and shear bands are tightly folded. Stations 6904A–6904H cover the northern western GSZ. Again, overprinting relationships indicate that early fabrics comprised shallowly dipping, top-SW shear zones/bands/s-c mylonites, which were folded into a sub-vertical position; later fabrics indicate dextral shear along the subvertical, NE-striking foliation. Along the northern GSZ margin, shear zones produced foliation boudins in the Permian–Triassic shales. Cross-cutting aplite dikes are locally sheared into low-temperature s-c mylonites; most of the granitoids are, however, non-deformed. Station 1192D in the southern western GSZ segment shows (ultra)mylonite in orthogneiss and quartzite. This fabric was isoclinally to tightly folded with NW vergence; these folds are openly refolded. The quartzites show high strain under intermediate–low-temperature deformation. Shear sense is mostly dextral but locally there was sinistral asymmetric boudinage. The early, pre-folding fabric may constitute a top-NE normal shear zone.

Deformation along the eastern GSZ segments and in the Turumtai host is overwhelmingly brittle. An exception occurs at Station 4726H (in the eastern GSZ). Here, a top-N, s-c fabric contains fibrolite in an ~20.5 Ma (section 6.3) pegmatite mylonite. Stations 6902B–6902G characterize one of the shear/fault zones of the Turumtai horst; locally strong deformation along mostly approximately NW-striking, low-temperature shear/fault zones is sinistral normal. Paleogene–Neogene (Pg<sub>2–3</sub>–N<sub>1</sub>?) strata (Yushin et al., 1964) in its hanging wall are tilted  $\geq 30^\circ$  toward the fault. These alluvial-fan deposits fine upward and have little sandstone, dominantly unsorted conglomerate with pebbles of sandstone, limestone, and layers rich in volcanic clasts. A parallel fault has an  $\sim 15 \times 5$  km hanging-wall basin with possibly Pliocene (N<sub>2</sub>) strata (Yushin et al., 1964) dipping up to  $40^\circ$  toward the fault (Figure S1).

#### 4. Fluid-Inclusion Analysis

We analyzed fluid inclusions in thick sections of samples from the eastern SPSZ and the ASZ (Figures S3 and S4). Analytical procedures for the University of Toronto laboratory are discussed in Text S2 (Bakker, 1997; Bodnar et al., 2003; Bodnar et al., 2014; Bodnar & Bethke, 1984; Diamond & Tarantola, 2015; Duan et al., 1995; Hacker et al., 2017; Hollister, 1988, 1990; Passchier & Trouw, 2005; Steele-MacInnis, 2018; Steele-MacInnis et al., 2012; Van den Kerkhof & Thiery, 2001). Central-eastern SPSZ Sample J4614A1 is a Bt gneiss, eastern SPSZ Sample J4615D1 is a mylonitic Bt + Sil paragneiss, and ASZ Sample J4707B1 is a mylonitic orthogneiss. The fluid inclusions are hosted in secondary assemblages of mostly Qz and rare Cal that trace healed fractures and cut across grain boundaries, indicating late syn-deformational to mostly post-deformational fluid entrapment during exhumation of the domes.

We interpret the fluid inclusions to represent fluids trapped during the early stages of fracture healing as the rocks passed through the ductile–brittle transition during exhumation. Microstructural analysis (Figure S2) indicates that the fluid inclusions were mostly trapped at temperatures below subgrain-rotation recrystallization in Qz ( $< \sim 300$ – $450$  °C) that dominates deformation in the shear-zone gneisses/mylonites. The fluid inclusions themselves indicate variable flux of fluids derived from metamorphic devolatilization and possible incursion of deeply circulating meteoric water. Combining the temperature estimates from the Qz microtextures with the fluid-inclusion estimates, crude minimum pressures for each sample can be derived:  $\sim 3$  kbar for central-eastern SPSZ Sample J4614A1,  $\sim 1.2$  kbar for eastern SPSZ Sample J4615D1, and  $\sim 1.5$  kbar for ASZ Sample J4707B1 (Figure S4).

#### 5. Geothermochronology: Techniques

##### 5.1. Acquisition of Radio-Isotopic Ages

We quantified the timing and rates of crystallization, cooling, and exhumation of the Alichur-dome region (see Figure S3 for sample locations) using the following chronometers: zircon/titanite/rutile (U–Th)/Pb, ZUPb/TUPb/RUPb and monazite Th/Pb, MThPb (Table S4 and Data Sets S1 and S2); detrital-zircon (U–Th)/Pb (Table S5); amphibole/white-mica/biotite/K-feldspar/plagioclase  $^{40}\text{Ar}/^{39}\text{Ar}$ , AmpAr/WmAr/BtAr/KfsAr/PlAr (Table S6 and Data Sets S3 and S4); zircon and apatite (U–Th)/He, ZHe/AHe (Table S7);

zircon/apatite fission track, ZFT/AFT (Tables S8 and S9). For the sake of completeness, we report our new data together with previously published intermediate–low-temperature data for the South Pamir (Chapman, Robinson, et al., 2018; Hacker et al., 2017; Hubbard et al., 1999; Schmidt et al., 2011; Stearns et al., 2013; Stearns et al., 2015; Stübner, Ratschbacher, Weise, et al., 2013; Yuan et al., 2004). The ages constrain (re)crystallization or cooling of minerals through a 700–110 °C temperature window.

Our ZUPb/TUPb/RUPb/MThPb data set was generated at six labs, analytical procedures for which are outlined in Text S3 (Frei & Gerdes, 2009; Gehrels et al., 2008; Kylander-Clark et al., 2013; Linnemann et al., 2011; Ludwig, 2000; Ludwig, 2008; Paton et al., 2011; Spear et al., 2008; Spencer et al., 2013; Van Achterbergh et al., 1999; Wiedenbeck et al., 1995; Williams, 1998). We used *Isoplot* (Ludwig, 2008) to calculate, depending on context, the most geologically meaningful Concordia, weighted-mean, and lower-intercept ages possible with common-Pb-corrected and/or non-common-Pb-corrected data. To ensure reproducibility of the reference material, we report all <2% calculated  $2\sigma$  crystallization-age uncertainties as 2%.

Our  $^{40}\text{Ar}/^{39}\text{Ar}$  data set was generated via stepwise degassing using a  $\text{CO}_2$ -laser or a high-temperature cell coupled to an ARGUS noble-gas mass spectrometer at the TU Bergakademie Freiberg, Germany. Three protomylonites were ablated in thick sections at multiple spots along and across Wm, Bt, and Kfs grains that were partly dragged into shear bands; these analyses employed an ArF-excimer laser and an ARGUS VI mass spectrometer. The ages include weighted-mean and inverse-isochron ages; we report the ablation dates as the median of all spot analyses.  $^{40}\text{Ar}/^{39}\text{Ar}$  analytical and data reduction procedures are outlined in Text S4 (Dalrymple & Lanphere, 1969; Ludwig, 2008; McDougall & Harrison, 1999; Renne et al., 2010; Renne et al., 2011; Sperner et al., 2014).

Our ZHe and AHe data set was generated at three labs: The Geochronology Center Göttingen, Germany, the (U–Th)/He Lab at the Universität Tübingen, Germany, and the Arizona Radiogenic Helium Dating Laboratory in Tucson, AZ, USA. We analyzed three grains per sample for Zrn and four grains per sample for Ap and report the ages for all samples as the nonweighted mean  $\pm 2\sigma_M$  of the  $F_T$ -corrected, single-grain ages. ZHe and AHe analytical procedures are outlined in Text S5 (Farley, 2002; Farley et al., 1996; Reiners et al., 2004; Reiners et al., 2005). Our new Zrn and Ap fission-track data set was generated by three counters at TU Bergakademie Freiberg (ZFT and AFT) and at the University of Arizona (AFT only). AFT and ZFT analytical procedures are outlined in Text S6 (Carlson et al., 1999; Donelick et al., 1999; Donelick et al., 2005; Gleadow, 1981; Gleadow et al., 2015; Hurford & Green, 1983; Jonckheere et al., 2003; McDowell et al., 2005).

We omit from consideration calculated ages that do not likely represent cooling ages, including: (i) Two new ZFT (9911D1 and 9914B1), one new ZHe (4726G1), and three published AFT (6824F1, 6828A1, and 6904M2) ages that exhibit  $>1\sigma$  intrasample age inversion with respect to higher- or lower-temperature thermochronometric data; (ii) Both of our two AHe (J3709B1 and J4619B3) that exhibit  $>50\%$   $2\sigma$  uncertainty; and (iii) One published AFT age (9914D4) that does not overlap within  $2\sigma$  uncertainty with other AFT ages from the same outcrop (published ages from Stübner, Ratschbacher, Weise, et al., 2013). The inverted thermochronometric ages may reflect heating-related annealing, slow cooling through the ZFT/ZHe/AFT/AHe partial annealing/retention zones, and/or radiation-damage accumulation (e.g., Flowers et al., 2009; Guenther et al., 2013; Reiners & Brandon, 2006).

## 5.2. Closure-Temperature Estimates

We used CLOSURE (Brandon et al., 1998; Ehlers et al., 2005) to estimate effective closure temperatures ( $T_c$ ) (Dodson, 1973) for all thermochronologic ages reported in this and previous studies. User-defined inputs for CLOSURE, including diffusion-kinetic parameters and effective diffusion domain size (EDDS), are discussed below. We selected output  $T_c$  from sets of cooling-rate-dependent  $T_c$  based on cooling rates that we prescribed for different structural domains in the South Pamir, which themselves are based on single-sample cooling-rate regressions obtained in this study and Stübner, Ratschbacher, Weise, et al. (2013). The prescribed cooling rates are highest for the footwalls of the Alichur (50 °C/Ma) and Shakh dara (40, 50, or 60 °C/Ma) domes, lowest for the Alichur-dome hanging wall (3 °C/Ma), intermediate for the Shakh dara-dome hanging wall (20 °C/Ma), and variable for the Turumtai horst (2 or 10 °C/Ma) and the GSZ (15, 35 or 50 °C/Ma) (Tables S6–S9). We used the following diffusion parameters in CLOSURE to estimate  $T_c$ : Harrison (1982) for AmpAr (437–540 °C); Robbins (1972) and Hames and Bowring (1994) for WmAr (315–412 °C); Grove and Harrison (1996) for BtAr (186–373 °C); Foland (1994) for KfsAr (279–362 °C);

Reiners et al. (2004) for ZHe (165–209 °C); Farley (2000) for AHe (56–80 °C); the radiation-damaged Zrn model of Brandon et al. (1998) for ZFT (217–250 °C); and Ketchum et al.'s (1999) “average apatite composition” model (after Table 4 in Carlson et al., 1999) for AFT (107–132 °C).

CLOSURE-based  $T_c$  estimates for  $^{40}\text{Ar}/^{39}\text{Ar}$  and (U–Th)/He data implement an additional, EDDS input. For  $^{40}\text{Ar}/^{39}\text{Ar}$ , we input analysis-specific % $^{39}\text{Ar}$  released and averaged the infinite-cylinder EDDS computed from minimum and maximum grain diameters for sieved mineral separates following Rutte, Ratschbacher, Khan, et al. (2017). For ZHe and AHe, we computed  $T_c$  for samples as the averages of those for the component grains. Single-grain  $T_c$  were computed with CLOSURE using available equivalent spherical radii (ESR) (Text S5). For the published ZHe data (Stübner, Ratschbacher, Weise, et al., 2013), we use the reported sample ESR and  $T_c$ . For ZHe samples without ESR data, we define  $T_c$  as the mean of  $T_c$  for all samples within the same structural-thermochronologic domain. For the KfsAr and PlAr analyses of grains that may contain multiple diffusion domains (Lovera et al., 1989) or complex phase changes, sericite, and/or fluid inclusions (Cassata & Renne, 2013; Villa & Hanchar, 2013), we assigned variable, empirically derived  $T_c$ . This is based on whether the dates reflect gas released at high, intermediate, or low temperatures during degassing and what microstructural, hydrothermal-alteration, and deformation features we observed in outcrop and thin sections. The large uncertainties for these KfsAr and PlAr  $T_c$  impose negligible constraints on the derived cooling-rate estimates.

### 5.3. Cooling-Rate Estimates

We used Isoplot (Ludwig, 2008) to compute weighted temperature-time regressions of multi-thermochronometric data to estimate and compare cooling rates ( $dT/dt$ ) for: (i) Individual samples and multiple samples from spatially confined (m-scale) outcrops; and (ii) Bulk structural domains. We used  $2\sigma$  age uncertainties for all chronometers and, following Rutte, Ratschbacher, Khan, et al. (2017), we defined  $2\sigma$   $T_c$  uncertainties for all low–intermediate-temperature thermochronometers as 10% of the value we computed using CLOSURE. We used 25%  $T_c$  uncertainty for BtAr for samples that represent cooling ages for fine-grained Bt (~10  $\mu\text{m}$ ) grown on rims of coarse-grained Amp (80–500  $\mu\text{m}$ ). Each regression represents an average, monotonic cooling rate through the regressed T-t domain. To address the possibility of non-monotonic cooling for single-sample/-outcrop cooling rates (“single-sample cooling rates” for simplicity), we prioritized regressions using a greater number of T-t domains over regressions using a greater number of datapoints. For bulk-average cooling-rate estimates of structural domains, we regressed through the medians  $\pm 2\sigma_M$  of cooling ages and their  $T_c$ .

### 5.4. Exhumation-Rate Estimates

Estimating local exhumation rates (vertical cooling age trends) based on sample elevations in the Alichur region is problematic and imprecise due to the low relief and lack of an elevation-age transect in this study. Compared to Stübner, Ratschbacher, Weise, et al.'s (2013) 2000–2250 m elevation range for transects in the Shakh dara dome spanning ~3 km horizontal distance, our samples span 700–1100 m and are horizontally clustered over tens of km (Figure S3). Vertical cooling-age trends are therefore difficult to resolve within analytical uncertainty over a comparatively small elevation range and cannot reliably be deconvolved from horizontal cooling-age trends. Local exhumation rates are similarly difficult to estimate in the GSZ due to its structural complexity.

As an alternative, we estimated bulk-average exhumation rates for the structural domains by regressing through the medians of the pooled thermochronometric ages and their corresponding median closure depths assuming geothermal gradients of 30–50 °C/km. We compare these results to exhumational steady-state erosion rates for the median ages of the relevant thermochronometers determined using AGE2EDOT (Brandon et al., 1998; Reiners & Brandon, 2006).

## 6. Geothermochronology: Results and Interpretations

We collectively discuss the new and published radio-isotopic-age data for the structural domains in the Alichur region to provide an updated assessment of available geologic age constraints. The data sources are provided in Table S2. The full (U–Th)/Pb and  $^{40}\text{Ar}/^{39}\text{Ar}$  data sets and plots are provided in Data Sets S1–S4.

### 6.1. Alichur Dome

Fifteen new ZUPb crystallization ages for mylonitic and non-mylonitic leucogranite samples from the Alichur dome span 22–17 Ma (Figures 4a and 5 and Table S4). The youngest, 16.7 Ma age is for deformed leucogranite J3612B1 (Figure 3i) in the proximal footwall of the ASZ where supra-solidus top-S flow contrasts with mylonitic and gneissic (sub-solidus), top-N deformation for the ASZ samples. We interpret the 22–17 Ma ZUPb ages to date crystallization of the leucogranite-injection complex and the commencement of slip along the ASZ. Zircons in the host granitoids—and inherited in the leucogranites—yielded 112–103 Ma ages, dating granitoid intrusion or migmatization.

Our new  $^{40}\text{Ar}/^{39}\text{Ar}$  step-heating ages comprise 17 WmAr and 14 BtAr analyses that span 16–11 Ma and correspond to a 412–316 °C  $T_c$  range (Figures 4b and 5 and Table S6). Although the WmAr (15.7–11.6 Ma) and BtAr (15.5–11.5 Ma) ages span the same range, the medians differ by 1 Ma (13.4 +1.5/–1.3 and 12.4 +1.5/–0.4, respectively). One ~14.7 KfsAr age for pegmatite sample 4726B2 is identical to its WmAr age; the ~9.1 Ma PlAr age for Sample 9911D1 is the youngest age. Six new  $^{40}\text{Ar}/^{39}\text{Ar}$  spot-ablation WmAr, BtAr, and KfsAr ages from protomylonitic orthogneisses (Table S5 and Data Set S3) span 17–13 Ma, within uncertainty of the step-heating ages. Despite age differences of up to ~10 Myr between the spots, there is no systematic intra- or inter-grain variation of the spot ages, and no younging of the spot ages closer to shear bands. Whereas spatial variation in spot ages could signify deformation effects, we interpret the lack thereof to signify cooling, albeit through unresolved closure temperatures. The high 14.5 +2.2/–1.9-Ma median for these ages reflects the large EDDS of these coarse-grained gneisses.

The (U–Th)/He data set comprises 17 ZHe ages that span 12–8 Ma and correspond to 202–190 °C  $T_c$  estimates (Figures 4c and 5 and Table S7). A lack of correlation between ZHe  $F_T$ -corrected single-grain ages and [eU] or ESR supports our representation of the non-weighted single-grain ages as cooling ages. The fission-track data set comprises two new ZFT ages (Figures 4c and 5 and Table S8) and 14 AFT ages (Figures 4d and 5 and Table S9). The ZFT ages are ~12.6 and 8.6 Ma and correspond to a 248 °C  $T_c$  estimate. The AFT ages collectively correspond to a 130 °C  $T_c$  estimate and span 11–4 Ma (median 7.3 +0.8/–1.5 Ma).

We interpret the narrow range of thermochronometric ages for the Alichur dome to reflect rapid, exhumation-related cooling (Figure 5). Regressing through the medians of the ages and  $T_c$  of the pooled WmAr, BtAr, ZFT, ZHe, and AFT data for the Alichur dome yields bulk-average cooling rate of ~42 °C/Myr over ~375–130 °C from 13.4–7.3 Ma (Figure 6a). With that rate, surface temperatures would have been reached at ~5 Ma. Thermal resetting due to leucogranite-intrusion-related re-heating does not account for any of the thermochronometric ages because the 16–4 Ma cooling-age range for all thermochronometers is younger than the 22–17 Ma crystallization-age range for the leucogranites, and single-sample ZUPb ages are older than and do not overlap in uncertainty with the intermediate-temperature ( $^{40}\text{Ar}/^{39}\text{Ar}$ ) ages (Figure S5). Broadly similar single-sample cooling rates for the Alichur dome corroborate the ~42 °C/Myr bulk-average cooling rate (Figure 6b).

The pooled thermochronometric data for the Alichur dome are equivalent to bulk-average exhumation rates spanning 0.8–1.4 km/Myr (assuming a 30–50 °C/km geothermal gradient). Exhumational steady-state values for the WmAr, BtAr, ZFT, ZHe, and AFT systems span 0.6–1.1 km/Myr and underestimate the true bulk-average exhumation rate due to surface temperatures being attained at ~5 Ma (Figure 6a). Our preferred bulk-average exhumation-rate estimate is ~1.1 km/Myr, consistent with a 40 °C/km geothermal gradient.

### 6.2. ASZ Hanging Wall and Turumtai Horst

The ASZ hanging wall and Turumtai horst exhibit similar radio-isotopic-age patterns for all available chronometers (Figure 4). Seven ZUPb and two TUPb ages for non-deformed or weakly deformed granitoids span 120–103 Ma; Turumtai-horst sample 6901D1 yielded two ZUPb age clusters at ~104 and ~88 Ma (Figure 4a and Table S4). The  $^{40}\text{Ar}/^{39}\text{Ar}$  data set (five AmpAr, four WmAr, eight BtAr, one KfsAr, and one PlAr) spans 118–83 Ma (Figure 4b and Table S6). Nearly all samples show Ar loss in the low-temperature part of the spectra. Four of the AmpAr ages span 107–104 Ma, one overlaps within its large uncertainty with this range; the  $T_c$  estimates span 492–477 °C. Three WmAr ages span 107–102 Ma, one is at 116 Ma;  $T_c$  estimates span 349–325 °C. Six BtAr ages span 108–101 Ma, two are at ~118 and ~83 Ma;  $T_c$  estimates span 296–262 °C. Three imprecise ages for fine-grained Bt grown on rims of Amp cluster at ~55 Ma (58–54 Ma) with  $T_c$  estimated

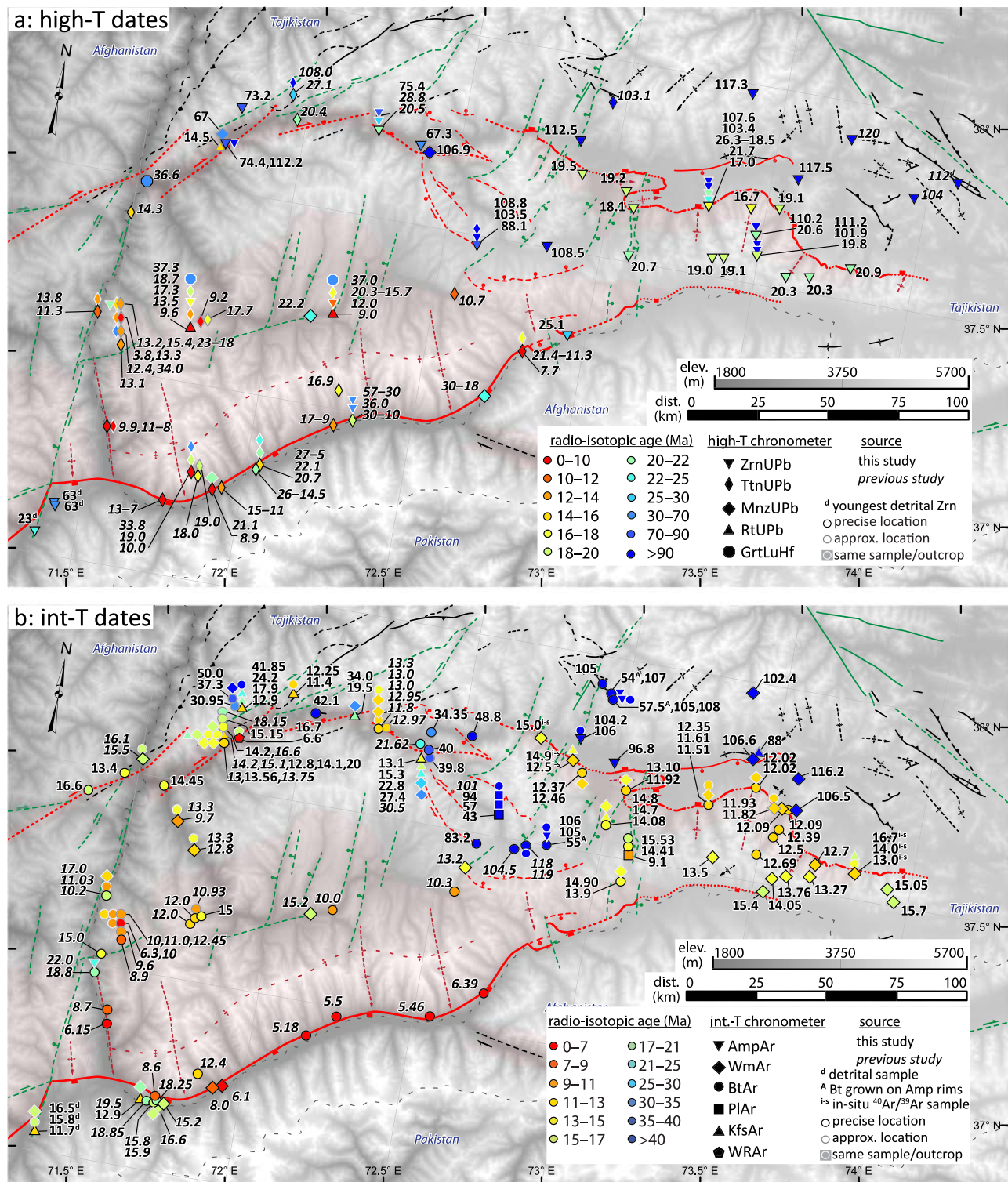


**Figure 4.** (a) (U-Th)/Pb zircon, titanite, monazite, rutile, and Lu/Hf garnet dates (Chapman, Scoggin, et al., 2018; Hacker et al., 2017; Schmidt et al., 2011; Smit et al., 2014; Stearns et al., 2015; Stübner, Ratschbacher, Weise, et al., 2013). (b) <sup>40</sup>Ar/<sup>39</sup>Ar amphibole, white-mica, biotite, K-feldspar, plagioclase, and whole-rock dates (Hubbard et al., 1999; Stübner, Ratschbacher, Weise, et al., 2013). (c) Zircon fission-track and (U-Th)/He dates (Chapman, Robinson, et al., 2018; Stübner, Ratschbacher, Weise, et al., 2013). (d) Apatite fission-track dates (Chapman, Robinson, et al., 2018; Stübner et al., 2013b). Symbol shape indicates chronometer; symbol fill color indicates age; symbol boundary color indicates sample location (black, precise location; gray, approximate location; white, approximate location for multi-dated sample/outcrop). Ages for samples with reported age ranges are colored by mean of maximum and minimum ages.

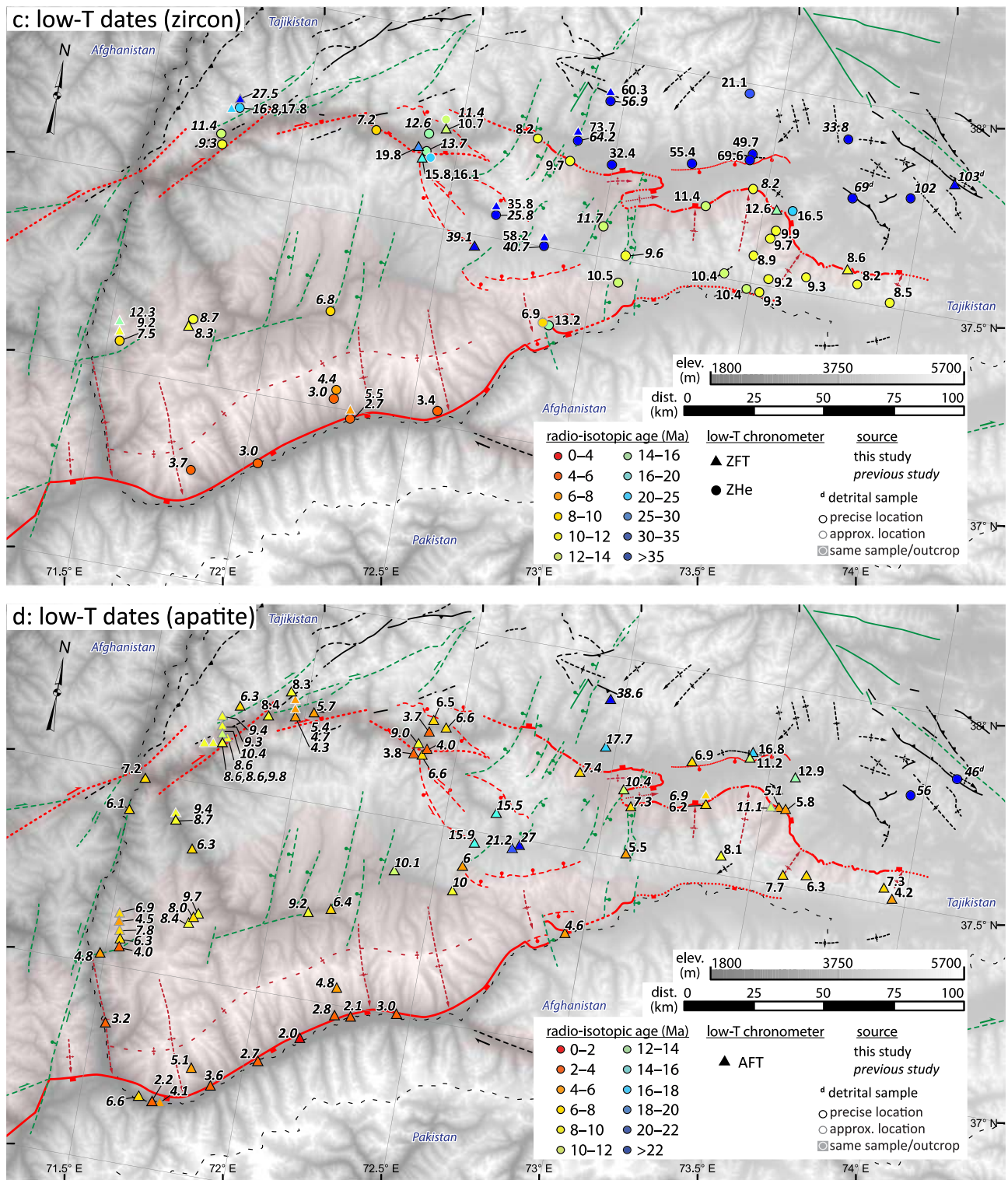
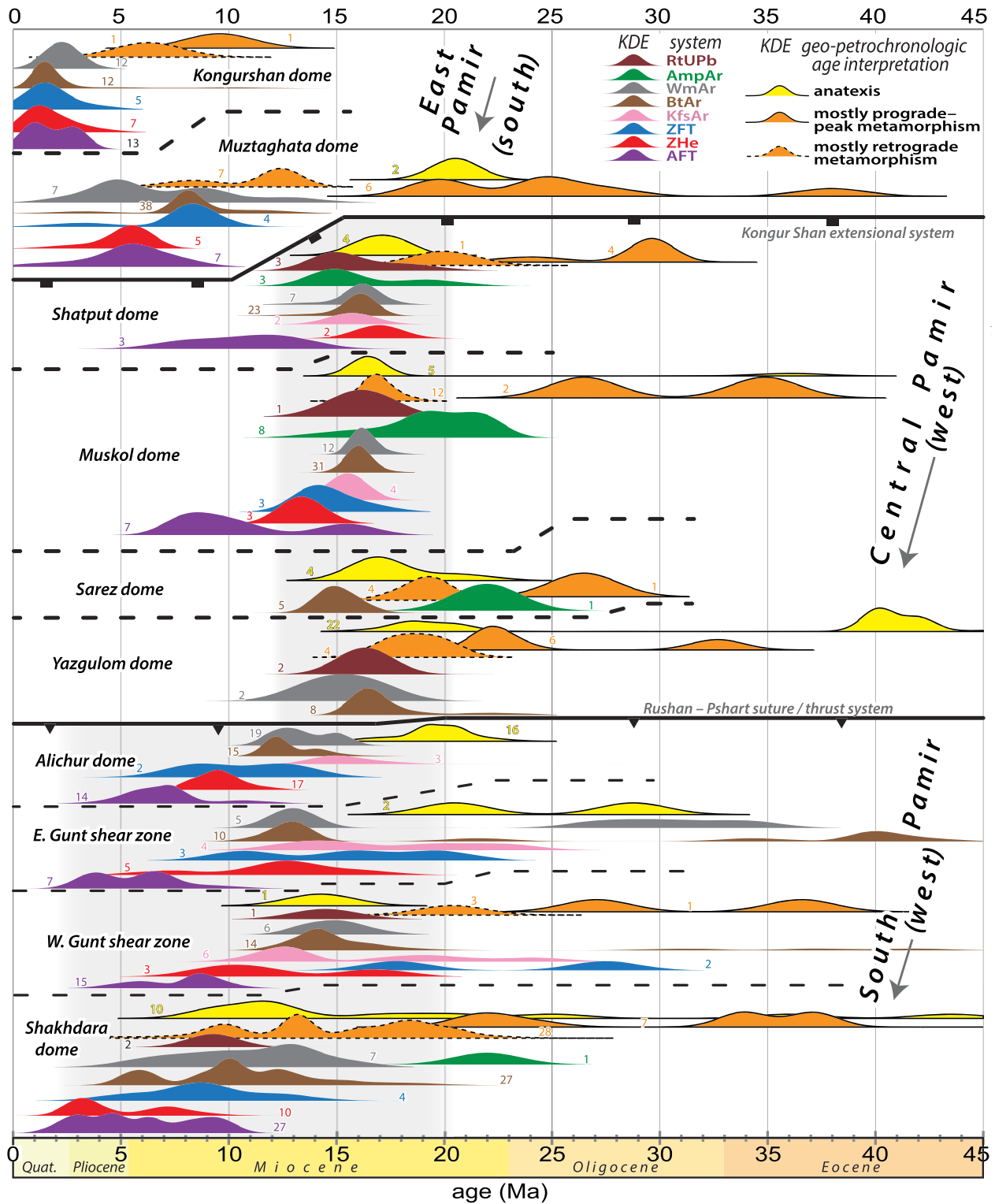
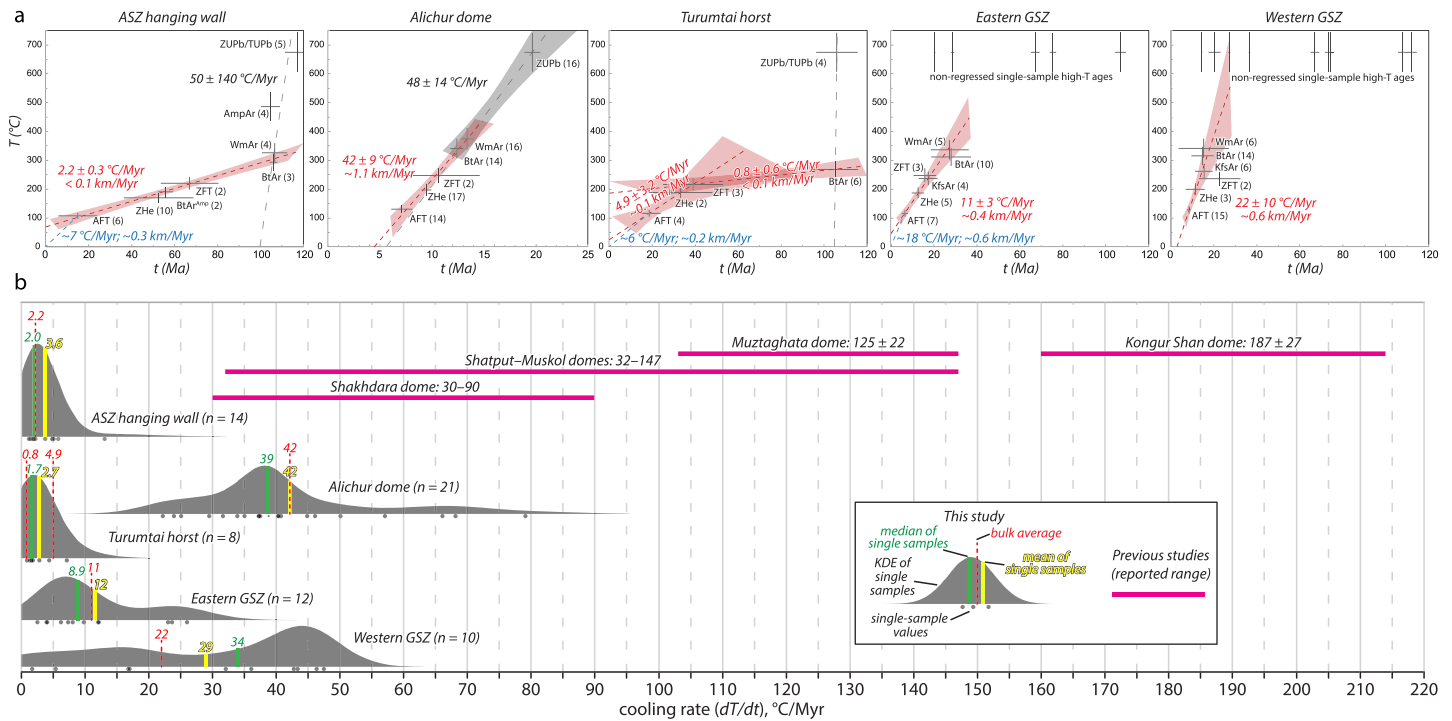


Figure 4. (continued)



**Figure 5.** Compiled kernel density estimates (KDEs) of geo-petro-thermochronologic ages for bedrock samples from the Pamir gneiss domes (Cai et al., 2017; Cao, Wang, et al., 2013; Chapman, Robinson, et al., 2018; Chapman, Scoggin, et al., 2018; Hacker et al., 2017; Hubbard et al., 1999; Robinson et al., 2004; Robinson et al., 2007; Rutte, Ratschbacher, Khan, et al., 2017; Schmidt et al., 2011; Stearns et al., 2013; Stearns et al., 2015; Stübner, Ratschbacher, Weise, et al., 2013). Shaded vertical bands highlight the timing of ~N-S extensional gneiss-dome exhumation in the Central and South Pamir; the East Pamir is not addressed. The eastern and western Gunt shear zone are included for comparison to the Alichur and Shakhdara domes. KDEs (adaptive bandwidth = 1 Myr) plotted using *DensityPlotter 7.3* (Vermeesch, 2012). U/Pb mixed ages plotted using average of minimum and maximum ages and setting  $2\sigma$  to the mixed-age range.



**Figure 6.** (a) Bulk-average cooling-rate estimates through medians of pooled cooling ages and their closure temperatures. Error crosses indicate  $\pm 2\sigma_M$  for pooled cooling ages and  $\pm 2\sigma = 10\%$  for pooled closure temperatures for each chronometer. Red error envelopes and lines indicate exhumation-related cooling through intermediate–low temperatures; gray error envelopes and lines indicate post-magmatic conductive cooling; dashed blue lines indicate steady-state cooling to the present. (b) Kernel density estimators (KDEs) of single-sample cooling rates for the ASZ hanging wall, Alichur dome, Turumtai horst, eastern and western Gunt shear zone (GSZ). Medians and means of single samples indicated in red and blue; bulk-average estimates (regressions through medians of pooled cooling ages) shown in yellow for comparison. Previously reported cooling-rate ranges for other Pamir gneiss domes shown for comparison (Cao, Wang, et al., 2013; Hacker et al., 2017; Rutte, Ratschbacher, Khan, et al., 2017; Stübner, Ratschbacher, Weise, et al., 2013). KDEs plotted use  $3^\circ\text{C/Myr}$  adaptive bandwidth with *DensityPlotter* 7.3 software (Vermeesch, 2012).

at  $\sim 190^\circ\text{C}$ . The KfsAr age for orthogneiss Sample 0909A1 is  $\sim 88$  Ma ( $T_c = 261^\circ\text{C}$ ); the magmatically zoned Pl may contain several diffusion domains with age components at  $\sim 94$ ,  $57$ , and  $\sim 43$  Ma. Five ZFT (Table S8) and 12 ZHe (Table S7) ages span  $74$ – $36$  and  $102$ – $17$  Ma and represent  $T_c$  estimates of  $\sim 220$  and  $175^\circ\text{C}$ , respectively (Figure 4c). Ten AFT ages span  $21$ – $11$  Ma with two outliers at  $39$  and  $7$  Ma;  $T_c$  is at  $\sim 107^\circ\text{C}$  for the Alichur dome hanging wall and  $\sim 116^\circ\text{C}$  for the Turumtai horst (Figure 4d and Table S9).

We interpret the  $118$ – $103$  Ma ZUPb and TUPb ages to collectively date granitoid crystallization in the ASZ hanging wall and Turumtai horst; the  $\sim 88$  Ma ZUPb age for the Turumtai horst may date partial re-melting of the former granitoids. Most of the AmpAr/WmAr/BtAr ages overlap with the crystallization ages and signify rapid post-magmatic conductive cooling. It is not clear whether the scattered ZFT and ZHe ages represent cooling due to slow exhumation or thermal relaxation subsequent to possible re-heating. The comparatively narrow AFT age range ( $21$ – $11$  Ma, excluding the youngest and the two oldest ages) likely represent exhumation-related cooling.

For the ASZ hanging wall, regressing through the medians of the ages and  $T_c$  of the WmAr, BtAr (including fine-grained Bt grown on Amp rims), ZFT, ZHe, and AFT data yields a bulk-average cooling rate of  $\sim 2^\circ\text{C/Myr}$  between  $\sim 330$ – $110^\circ\text{C}$  and  $\sim 107$ – $15$  Ma, and attainment of surface temperatures in the far future ( $\sim 30$  Myr; Figure 6a). This implies a two-stage cooling history involving very slow cooling or isothermal holding during much of the Cretaceous–Cenozoic, followed by more rapid cooling on average ( $\sim 7^\circ\text{C/Myr}$ ) from the AFT  $T_c$  to present surface conditions. Broadly similar single-sample cooling rates for the ASZ hanging wall corroborate the  $\sim 2^\circ\text{C/Myr}$  bulk-average cooling rate (Figure 6b).

The pooled thermochronometric data for the ASZ hanging wall are equivalent to bulk-average exhumation rates spanning  $0.06$ – $0.11$  km/Myr (assuming a  $20$ – $40^\circ\text{C/km}$  geothermal gradient). Inconsistency between the bulk-average exhumation rates, exhumational steady-state erosion rates for the WmAr, BtAr, ZFT,

and ZHe systems (similarly  $\sim 0.15$  km/Myr), and exhumational steady-state erosion rates for the younger AFT system ( $\sim 0.3$  km/Myr) reflects the two-stage cooling discussed above (Figure 6a); only post-AFT-age exhumation can be considered steady-state. Taken together, the data suggest bulk-average exhumation at  $< 0.1$  km/Myr during the Cretaceous–middle Cenozoic, followed by  $\sim 0.3$  km/Myr during the late Cenozoic.

Two cooling stages are resolvable for the Turumtai horst. Regressing through the medians of the ages and  $T_c$  of the BtAr and ZFT data yields a bulk-average cooling rate of  $\sim 1$  °C/Myr between  $\sim 270$ – $220$  °C and  $105$ – $40$  Ma (Figure 6a). Regressing through that of the ZFT, ZHe, and AFT data sets yields a bulk-average cooling rate of  $\sim 5$  °C/Myr between  $\sim 220$ – $120$  °C and  $\sim 40$ – $19$  Ma, which suggests an increase in the cooling rate during the early Cenozoic. This regression implies attainment of surface temperatures  $\sim 5$  Myr in the future, suggesting  $\sim 6$  °C/Myr cooling after  $\sim 19$  Ma. Single-sample cooling rates for the Turumtai horst broadly span the  $\sim 1$ – $5$  °C/Myr bulk-average cooling rates (Figure 6b).

The pooled thermochronometric data for the Turumtai horst are equivalent to bulk-average exhumation rates spanning  $0.02$ – $0.04$  km/Myr during the Cretaceous–early Cenozoic and  $0.12$ – $0.25$  km/Myr during the middle–late Cenozoic (assuming a  $20$ – $40$  °C/km geothermal gradient). Exhumational steady-state erosion rates for the BtAr system are  $\sim 0.15$  km/Myr. Those for the ZFT, ZHe, and AFT systems span  $\sim 0.20$ – $0.25$  km/Myr. Taken together, the data suggest bulk-average exhumation at  $\leq 0.1$  km/Myr during the Cretaceous–early Cenozoic, followed by  $\sim 0.2$  km/Myr during the middle–late Cenozoic (Figure 6a).

### 6.3. Gunt Shear Zone (GSZ)

Six samples suggest a common granitoid/orthogneiss crystallization and remelting history. Three Bt + Wm  $\pm$  Grt  $\pm$  Tur gneisses re-melted at  $27$ – $21$  Ma (two ZUPb and one TUPb), two of them crystallized at  $\sim 75$  Ma, and three other granitoids have similar crystallization ages ( $73$ – $67$  Ma; two ZUPb and one MThPb). Three gneisses (one ZUPb, one TUPb, and one MThPb) crystallized at or contain inherited  $112$ – $107$  Ma grains (Figure 4a and Table S4). The latter ages are similar to most ZUPb ages of the Alichur-dome region, the  $75$ – $67$  Ma crystallization ages are likely part of a still incompletely documented Late Cretaceous magmatic event in the Pamir (Chapman, Scoggin, et al., 2018; Schwab et al., 2004), and the  $27$ – $21$  Ma re-melting ages overlap with the age range for the Alichur-dome leucogranite-injection complex.

To report the intermediate–low-temperature thermochronologic results, we subdivided the GSZ—as in the structural description—into a western and an eastern segment; here, the former includes the data from the westernmost strand in Afghanistan. Fifteen of the WmAr, BtAr, and KfsAr ages are relatively evenly distributed over an  $\sim 50$ – $20$  Ma range (Figures 4b and 5 and Table S6); nearly all of these dates stem from the eastern GSZ and the low-strain margins of the western GSZ. Twenty-eight other WmAr, BtAr, and KfsAr ages— younger than  $\sim 20$  Ma—span a comparatively narrow range with a median at  $13.7 + 1.4 / - 0.7$  Ma. Two imprecise  $^{40}\text{Ar}/^{39}\text{Ar}$  dates of pseudotachylite veins—recrystallized ultracataclasite—in massive, Alichur-type granitoids south of the margin of the ductile western GSZ (station 1192E1) may indicate brittle GSZ activity at  $\sim 17$  and  $7$  Ma. The oldest two of the eight ZHe ages are—as the oldest  $^{40}\text{Ar}/^{39}\text{Ar}$  dates—from the eastern GSZ and the northern margin of the western GSZ; the remaining span  $13.7$ – $9.3$  Ma, with one outlier at  $7.2$  Ma (Figure 4c and Table S7). The 22 AFT ages again span a comparatively narrow range ( $10.4$ – $3.7$  Ma) with a median at  $7.2 + 1.4 / - 0.9$  Ma ( $T_c = \sim 125$  °C); the three youngest ages ( $4.0$ – $3.7$  Ma) are from the eastern GSZ, where it interacts with the shear zones/faults of the Turumtai horst (Figure 4c and Table S9).

For the eastern GSZ, regressing through the medians of the ages and  $T_c$  of the WmAr, BtAr, ZFT, ZHe, and AFT data produces an  $\sim 11$  °C/Myr bulk-average cooling rate between  $\sim 340$ – $120$  °C and  $\sim 27$ – $7$  Ma (Figure 6a). This regression implies attainment of surface temperatures  $\sim 5$  Myr in the future, suggesting a two-stage cooling history with  $\sim 18$  °C/Myr cooling after  $\sim 7$  Ma. Broadly similar single-sample cooling rates for the eastern GSZ corroborate the  $\sim 11$  °C/Myr bulk-average cooling rate (Figure 6b). For the western GSZ, regressing through the medians of the ages and  $T_c$  for the WmAr, BtAr, KfsAr, ZFT, ZHe, and AFT data produces an  $\sim 22$  °C/Myr bulk-average cooling rate from  $\sim 340$ – $130$  °C and  $\sim 15$ – $8$  Ma (Figure 6a). Single-sample cooling rates for the eastern GSZ are broadly faster than the  $\sim 22$  °C/Myr bulk average, similar to those of the Alichur dome (Figure 6b), and reflect the structural complexity of the GSZ.

For the eastern GSZ, the pooled thermochronometric data are equivalent to bulk-average exhumation rates of  $0.3$ – $0.5$  km/Myr (assuming a  $20$ – $40$  °C/km geothermal gradient). Inconsistency between the bulk-average exhumation rates and  $\sim 0.6$ – $0.7$ -km/Myr exhumational steady-state erosion rates for the WmAr, BtAr, KfsAr,

ZFT, ZHe, and AFT systems reflect the two-stage cooling for the eastern GSZ discussed above; only post-AFT-age exhumation can be considered steady state. Taken together, the eastern GSZ data suggest bulk-average exhumation at  $\sim 0.4$  km/Myr from 27–7 Ma, followed by  $\sim 0.6$  km/Myr since  $\sim 7$  Ma. For the western GSZ, the pooled thermochronometric data are equivalent to bulk-average exhumation rates of 0.6–1.1 km/Myr (assuming a 20–40 °C/km geothermal gradient). Exhumational steady-state erosion values for the WmAr and BtAr systems are  $\sim 1.0$  km/Myr; those for the KfsAr, ZHe, and AFT systems span 0.5–0.6 km/Myr. Taken together, the western GSZ data suggest bulk-average exhumation at  $\sim 0.6$  km/Myr since  $\sim 15$  Ma.

Interrogating the cooling history of the GSZ in more detail reveals locally systematic patterns that reflect broader structural heterogeneity. First, pooled-sample cooling rates for dates older (based on WmAr, BtAr, and KfsAr) and younger (based on WmAr, BtAr, KfsAr, ZHe, and AFT) than  $\sim 20$  Ma for the western and eastern GSZ differ drastically:  $\sim 1$  °C/Myr (regression through 15 dates, 100 % regression uncertainty) and  $\sim 23$  °C/Myr (54 dates and 16 % regression uncertainty), respectively (Figure S5). Second, pooled-sample cooling rates for the best-studied GSZ sections highlight regional variations. Within the western GSZ, the  $\leq 24$ -Ma re-melting age for pegmatite mylonite sample 4727C1 provides an oldest-age constraint for the onset of cooling along the section of stations 6905A–B, 4727C, and 1192D. Cooling there at  $\sim 43$  °C/Myr (10 dates; 18% regression uncertainty) between  $\sim 14$ –8 Ma likely marks the major shear-zone activity; the  $\sim 5$ -Ma intersection of the regression with surface temperature implies a waning of its activity sometime after  $\sim 8$  Ma. The adjacent section across the northern margin of the western GSZ (stations 6904M–Q) records cooling at  $\sim 34$  °C/Myr between  $\sim 17$  and 9 Ma (11 dates, excluding two dates  $> 17$  Ma, which are from the mostly non-deformed granitoids at the northernmost locations; 24% uncertainty); again, the  $\sim 5$  Ma intersection of the regression with surface temperature implies less-rapid cooling sometime after  $\sim 9$  Ma. For the eastern GSZ, the  $\sim 20.5$  Ma ZUPb pegmatite-mylonite re-melting age (sample 4726H1) pre-dates the onset of cooling. Stations 4726G, 6902B–6902P, 6903B, and 6903C, which are situated at the interaction between the eastern GSZ and the faults of the northern Turumtai horst, show slower cooling ( $\sim 15$  °C/Myr; 9 dates, 37% uncertainty; Figure S5) from 16–7 Ma than the sections in the western GSZ. This cooling path extrapolates to surface temperatures at  $\sim 0$  Ma. For this regression, we excluded  $> 20$  Ma ages and the cluster of the three youngest AFT ages. These anomalously young ages may be influenced by processes other than tectonic-exhumation-induced cooling, for example, active faulting along the southern continuation of the SKFS, which may drive the documented hot-spring activity in the northern Turumtai horst (Stübner, Ratschbacher, Weise, et al., 2013).

Estimating exhumation rates based on sample elevation in the GSZ is similarly problematic due to its complex structure. We confine the regressions through the WmAr, BtAr, and AFT dates, and elevation to the western GSZ (Figure S5). The WmAr and BtAr age-elevation data sets span a limited elevation range ( $\sim 485$  and 663 m over 2.4 and 4.8 km horizontal distance, respectively) and contain few data points (four and seven); their exhumation-rate estimates are similar, 0.2 (25% regression uncertainty) and 0.3 (42%) km/Myr, respectively. The AFT data set spans  $\sim 1061$  m, contains 10 data points (eight spread out over 4.8 km horizontal distance, the remaining two over 25 km), and yields an exhumation-rate estimate of  $\sim 0.9$  (181%) km/Myr. Compared to the WmAr and BtAr data set, this estimate may imply an increase in exhumation between 12–10 Ma; the exhumation rate must have decreased sometime after  $\sim 7$  Ma.

#### 6.4. Eastern Shakh dara Dome and South Pamir Shear Zone Hanging Wall: New (U-Th)/He Ages

One  $\sim 7$  Ma ZHe age for the eastern SPSZ proximal footwall ( $T_c = 203$  °C) and one  $\sim 13$  Ma ZHe age ( $T_c = 176$  °C) for the eastern SPSZ proximal hanging wall are separated by  $\sim 0.5$  km horizontal distance across the SPSZ detachment and define an  $\sim 6$ -Myr age offset. The offset indicates tectonic-exhumation-related cooling. The additional structural context for both samples in the hanging wall of a cross-cutting, ENE-dipping, high-angle normal fault that produced  $\sim 6$  km of apparent left-lateral separation of the SPSZ (station J4615B; Figure 2a) may imply a contribution of a younger component of erosion-related exhumation for both samples. One  $\sim 3$  Ma ZHe SPSZ footwall age ( $T_c = 196$  °C) farther west is in accordance with higher-magnitude exhumation along the central SPSZ.

#### 6.5. The South Pamir Shear Zone Hanging-Wall Basins

Age assignments for Cenozoic basin fill exposed in the hanging walls of the Shakh dara and Alichur domes span the Eocene/Oligocene–Pliocene (Vlasov et al., 1991). The Zebak basin in the hanging wall of the western SPSZ (Figure 1; Desio, 1975; Stübner, Ratschbacher, Rutte, et al., 2013) may be representative for all

basins in the Shakhdara–Alichur-dome area. Herein, we dated detrital zircons from two samples of red and gray sandstones with rare pebble layers of the pre-extensional sequence (without growth strata; samples 11910E1 and 11910F1) and one sample from a sandy layer in gray conglomerate of the syn-extensional sequence (with growth strata; 11911C5) (Figure 4a and Table S5). The youngest ZUPb age group of the pre-extensional strata is at ~63 Ma; older major age groups cluster at ~90, 215, 600, 930, and 2500 Ma. The youngest and one of the major age groups of the syn-extensional strata is at ~23 Ma; other major groups are at 150 and 180 Ma. The WmAr, BtAr, and KfsAr ages of a two-mica leucogranite pebble from sample 11911C1 of the syn-extensional strata, which we also used for detrital zircon dating, are ~16.5, 15.8, and (low confidence) 11.7 Ma, respectively; they record cooling through ~300 °C (Figure 4b and Table S6). This assigns a post-mid-Miocene depositional age to the syn-extensional strata, in accordance with the abundance of gneisses, leucogranites, and mylonites in their clast spectrum. These rocks are typical for the Shakhdara-dome footwall. The pre-extensional strata may have an Oligocene–early Miocene or older depositional age. The massive conglomerates of the basin remnants of the eastern SPSZ hanging wall, lacking the deformed rocks of the Shakhdara-dome footwall but containing lithologies of the South Pamir batholith, thus likely represent early syn-extensional strata, representing the upper-crustal equivalents of the lower–middle-crustal Shakhdara-dome footwall, and the Shakhdara-dome hanging wall.

## 7. Discussion

### 7.1. Cretaceous Geologic Evolution of the Alichur–Gunt Region

The Cretaceous granitoids in the Alichur–Gunt region represent an Andean-style continental arc—the South Pamir batholith (Aminov et al., 2017; Chapman, Scoggin, et al., 2018). The assignment of deformation in the protomylonite belt in the Cretaceous granitoids in the N-Alichur culmination north of the Bashgumbaz complex (Figure 2a) to Cretaceous or Cenozoic is ambiguous. The WmAr/KfsAr, ZHe, and AFT cooling age ranges are 107–88, 70–50, and 17–7 Ma, respectively. The highly variable but grossly E-trending stretching lineations and fault slickenlines, which formed during low-temperature deformation, are in general at high angle to the ~NNE-trending ASZ lineations (Figure 2a). This contrast in the lineation azimuths means the N-Alichur culmination is likely not an anticline exposing the ASZ—unlike the Tuzkul antiform. Because the formation temperature of the protomylonite fabrics overlaps with the  $T_c$  of the WmAr/KfsAr and ZHe thermochronometers, we interpret the protomylonite belt to have formed during the Late Cretaceous.

The strongly folded, non-mylonitic Zorkul gneisses ( $K_{gn}$ ; Figures 2a, 3l, and 3m) represent a fundamentally different style of deformation with respect to the mylonitic, consistently oriented Miocene shear zones that exhumed the Alichur and Shakhdara domes. Forthcoming petrochronology will detail the intrusion and metamorphism ages of these gneisses. The first, ~102 Ma ZUPb date (Figure 3j) indicates that the Zorkul gneisses may provide an igneous, metamorphic, and structural record of the South Pamir Cretaceous continental arc.

### 7.2. Cenozoic Geologic Evolution of the Alichur Region

#### 7.2.1. Alichur-Dome Leucogranite-Injection Complex

The textural and structural discordance between the early Miocene leucogranite-injection complex and the Alichur-dome Cretaceous granitoids, migmatites, and gneisses shows that the injecting magma was sourced from a deeper crustal level. The textural discordance between the highly oblique or orthogonal orientations of the dikes/sills with respect to the pre-Miocene fabrics (Figures 3g, 3h, 3j, and 3k) is corroborated by the Cretaceous, rather than Miocene ZUPb ages for the dated migmatitic rocks. Although mylonitized and broadly parallel to the foliation in the ASZ, the absence of in-situ melt textures and the ZUPb ages that overlap with those for non-deformed leucogranites, indicate a common, deep origin of these dike/sills (Figures 3c and 3d). We propose that the 22–17 Ma Alichur-dome leucogranite-injection complex originated from melts that formed during migmatization of the underlying lower–middle crust. Coeval gneisses exposed in the deeply exhumed Shakhdara dome (Figure 5a; (Hacker et al., 2017; Schmidt et al., 2011; Stearns et al., 2015; Stübner, Ratschbacher, Rutte, et al., 2013), especially the 22–17 Ma restitic migmatites, may represent an exposed analogue of the source of the Alichur-dome leucogranite-injection complex, which we propose underlies the Alichur dome. It remains to be tested whether modern anatexis in the South Pamir subsurface (Sass et al., 2014) represents a continuance of the melt-production episode that generated the exposed migmatites and leucogranites or a subsequent and distinct melt-production episode.

Whether exhumation of the Alichur dome commenced during or subsequent to the onset of local anatexis remains to be determined. We interpret the 22–17 Ma emplacement-age range for the Alichur-dome leucogranite-injection complex to represent an oldest-age constraint for the onset of exhumation. Emplacement of anatectic melts into the middle crust would have weakened the South Pamir crust due to heating above the ambient geotherm, providing an impetus to accommodate N–S extension by non-coaxial strain and facilitating the inception of the ASZ (e.g., Vanderhaeghe et al., 1999). The lack of in-situ migmatization structures in the leucogranite host rocks, and of contact aureoles along the leucogranite dike/sills, indicates that the latter intruded crust that was cooler than the leucogranite-crystallization temperatures (~675 °C). Although the apparent cooling rates from the high–intermediate-temperature systems (ZUPb–WmAr/BtAr) and the tectonic cooling rates (WmAr/BtAr–AFT) are to first order similar (48 and 42 °C/Myr, respectively; Figure 6a), monotonic cooling from leucogranite crystallization to upper-crustal conditions is unlikely; the 48 °C/Myr rate likely underestimates the post-emplacement dike/sill conductive-cooling rate.

### 7.2.2. Convergence-Parallel Exhumation of the Alichur Dome: Geometry and Kinematics

The Alichur dome was tectonically exhumed in the footwall of the low-angle ASZ via top-NNE, normal-sense shear (Figures 2 and 3b). Because the ASZ is not S-dipping in the south, a clear delineation of a dome axis is not possible (unlike the adjacent Shakh dara dome; Figure 1) (e.g., Whitney et al., 2004). Likely coeval deposition of hanging-wall strata N of the Tuzkul anticline (Figures 3f and 3m) and high-angle, top-S, normal faulting south of the N-Alichur culmination in the ASZ hanging wall (Figure 3n) reflect the same ~N–S extension that exhumed the Alichur dome in the footwall (Figure 2).

There are two possible interpretations for the open, long-wavelength, ~N-plunging corrugations of the ASZ (Figures 2a and 3b). One possibility is that they signify syn-mylonitic, extension-parallel lengthening and extension-perpendicular shortening (constriction) superimposed on the dominant, top-NNE simple shear (e.g., Singleton, 2013); this would imply that the corrugations are folds. Alternatively, they may signify regional (dome-scale) boudinage, that is, pinch-and-swell structures, that record minor ~E–W extension superimposed on the major ~N–S extension. The latter, our preferred interpretation (see section 7.2.5), resembles the inter- and intra-dome pinch-and-swell geometries of the Central Pamir domes (Rutte, Ratschbacher, Schneider, et al., 2017) and is consistent with locally observed dispersion in lineation azimuths in the ASZ (stations J4707B–J4707D/J4707G and J4707H, J4708B, J3612A–J3612C, and J3617C/J3618A–J3618C, Figure S1) that suggest flattening strain, in which minor ~E–W extension (boudinage) was coeval with the dominant ~N–S extension. We interpret the open and ~E-trending Tuzkul anticline and the N-Alichur culmination to record a phase of minor ~N–S shortening subsequent to the major ~N–S extension that exhumed the Alichur dome (Figures 2a and 3f). The double plunge of their fold axes likely reflects the geometric effect of ~N–S shortening overprinting the pre-existing, long-wavelength, ~N–S corrugations that characterize the Alichur dome and may be equivalent to those that folded the normal-shear fabrics of the GSZ (section 7.2.5).

Our observations of mylonitic SPSZ outcrops in the southwestern extremity of the Alichur dome (which overlaps with the northeastern Shakh dara dome) indicates that the SPSZ bounds at least this part of the Alichur dome (Figures 2a and 3s). The SPSZ may extend up to 40 km E of the easternmost mylonitic SPSZ rocks (Station J4621C; Figure S1) to brittle and shallow structural levels near the western shore of lake Zorkul. Regarding exhumation of the Alichur dome and with respect to the ASZ, the easternmost SPSZ is a subordinate structure that bounds the Alichur dome to the south for an incompletely constrained along-strike distance (roughly two thirds of the longitudinal range of the ASZ) and contributed negligibly to the exhumation of the Alichur dome.

The magnitude of convergence-parallel extension associated with the exhumation of the Alichur dome is difficult to constrain due to a lack of piercing points for the crystalline rocks in all of the footwall and much of the hanging wall (Figure 2). The planar geometry of the ASZ indicates minor footwall back-rotation and/or negligible isostatic-rebound-driven doming (e.g., Lister & Davis, 1989), both of which may be interpreted to imply a low slip magnitude. A simplification of the ASZ as a 20° N-dipping, dip-slip fault enables a rough estimate of the extension and normal-slip magnitudes: a >6 km estimate for the magnitude of vertical exhumation based on our ~1.5-kbar fluid-trapping-pressure estimate for ASZ Sample J4707B1 (section 4, Figure S4) implies >16 km N–S extension and >18 km offset. Alternatively, assuming a 30–50 °C/km geotherm, the ~300–450 °C deformation-temperature range derived from microstructures in the ASZ

tectonites (Text S1 and Figure S2) is equivalent to 6–15 km exhumation, or >6–15 km exhumation (our preferred interpretation) if we integrate the minimum estimate from fluid-inclusion data (Figure S4). This implies >16–38 km N–S extension and >18–48 km slip. Because both the fluid-inclusion-derived and the ~300 °C lower-bound, ductile-deformation-derived exhumation-depth estimates are minimum values that constrain exhumation from the brittle–ductile transition, our preferred values are 10–15 km (exhumation), 27–41 km (extension), and 29–44 km (slip). In the case that the ASZ dip is listric and becomes subhorizontal at depth, the extension and slip estimates represent minimum constraints. Because the Alichur dome is fault/shear zone bounded both to the north and to the south, and because the Miocene cooling ages that span its entire width imply exhumation by a single event, the maximum exposed ~N–S width of the dome suggests that 30–35 km is a reasonable ~N–S extension estimate.

We interpret the south dip and dominantly granitic-clast lithology of the conglomerate strata in the Alichur-dome hanging wall north of the Tuzkul anticline (station J4708A; Figures 2a, 3g, and S1) to represent a Neogene syn-extensional basin. Our interpretation of the conglomerate strata in the proximal hanging wall of the eastern SPSZ (stations J4615A and J4616C) is genetically compatible with the top-S extension recorded by the SPSZ mylonites (Figures 2a, 3s, 3t, and S1). Our detrital ZUPb dating and  $^{40}\text{Ar}/^{39}\text{Ar}$ -based clast-cooling ages for the pre-extensional and syn-extensional strata in the Zebak proximal hanging wall basin of the southwestern Shakhdara dome (Figure 1) assign an early syn-extensional age to the strata of these basins (Tables S5 and S6); their conglomerate clasts contain the typical, upper-crustal rock association of the Shakhdara–Alichur region (particularly the granitoids of the South Pamir batholith) but lack the Neogene mylonites and leucogranite gneisses of the dome interiors.

### 7.2.3. Convergence-Parallel Exhumation of the Alichur Dome: Timing and Rates

The onset of the exhumation of the Alichur dome via ~N–S extension is bracketed between the 22–17 Ma crystallization-age range of the Alichur-dome leucogranite-injection complex and the oldest, ~16 Ma WmAr footwall cooling ages. Our thermochronology data set constrains the timing of sub-solidus cooling and exhumation of the Alichur dome through 410–130 °C from 16–4 Ma (Figures 5 and S5). The Alichur dome monotonically cooled through sub-solidus temperatures at ~42 °C/Myr (Figures 6 and S5), which is equivalent to an exhumation rate of ~1.1 km/Myr. Three observations demonstrate that the cooling ages dominantly reflect normal-sense slip along the ASZ: (i) Cooling-age offset across the ASZ for all chronometers, with younger ages in the footwall and older ages in the hanging wall (with one exception for AFT, discussed below; Figures 4b–4d); (ii) Cooling-rate offset across the ASZ, in which the ~42 °C/Myr bulk-average cooling of the Alichur dome through 410–130 °C from 16–4 Ma was roughly six times faster than ~7 °C/Myr time-averaged cooling of the ASZ hanging wall through low-surface temperatures from 15–0 Ma (Figure 6a); and (iii) The pattern of broadly older WmAr/BtAr/ZHe cooling ages closer to the easternmost SPSZ and broadly younger WmAr/BtAr/ZHe cooling ages closer to the ASZ, which attests to trivial involvement of the easternmost SPSZ in exhuming the Alichur dome.

The greater susceptibility of the AFT system to upper-crustal tectonic and surface processes necessitates a wider variety of possible interpretations. Firstly, the ~11–4 Ma AFT cooling-age range for the Alichur dome may exclusively signify exhumation due to extension along the ASZ. However, we cannot rule out the possibility that the youngest ages reflect exhumation in the footwalls of the cross-cutting, ~N-striking north striking normal faults that characterize the neotectonic deformation (section 7.2.7). Secondly, the ~7 Ma AFT cooling age for ASZ hanging wall sample 0909C1 overlaps with the footwall cooling-age range and could be interpreted to reflect the cessation of slip along the ASZ by ~7 Ma. More likely, however, is that this age represents exhumation of the footwall of the steeply S-dipping normal fault (Figures 2a, 3n, and 4d) that bounds the N-Alichur culmination to the south. This fault likely extends ~20 km westward from its westernmost exposure as a buried fault given the westward widening of the Quaternary(?) alluvium basin that floors the Alichur valley, recording minor, ~N–S extension within the ASZ hanging wall that occurred coevally with and antithetically to the greater ~N–S extension associated with the exhumation of the Alichur dome (Figure 2).

Two considerations suggest that erosion contributed negligibly to the exhumation of the Alichur dome. First, the position of the Alichur dome in the leeward, eastern Pamir plateau (Figure 1) with eastward-decreasing modern precipitation from the midlatitude Westerlies (Aizen et al., 2001; Carrapa et al., 2014; Chen et al., 2002; Huffman et al., 1997; Huffman et al., 2007) is consistent with minimal evident denudation that the upper-crustal exposure levels for the ASZ hanging-wall strata that imply (Figures 2a, 3n, and 3q). Second,

the slow exhumation in the ASZ hanging wall (Figure 6) is a proxy for regional erosion rates that should add to tectonic exhumation rates for an  $\sim 1.1$  km/Myr total exhumation rate.

#### 7.2.4. The Gunt Shear Zone

The GSZ is a segmented shear/fault zone with a subvertical, E(NE)-striking, generally dextral shear fabric (Figure S1). Its early evolution is defined by a series of shallowly, broadly  $\sim$ N- and S-dipping shear zones with dominantly normal-shear kinematics. Folding about  $\sim$ E-trending fold axes rotated the GSZ into a subvertical orientation. Continued deformation preferentially accentuated steeply dipping fold limbs under dextral shear. The fold tightness broadly decreases from west (isoclinal-tight) to east (tight-open) along the GSZ segments. The gentle-open geometry of the folds in the Alichur region reflects the eastward continuation of decreasing fold tightness along the GSZ. This may reflect the rheological transition from the dominantly well-bedded metasedimentary rocks in the west (western GSZ) to dominantly crystalline rocks in the eastern GSZ and the Alichur region. The segmentation, folding, overall low-temperature deformation, and particularly pronounced dextral strike-slip deformation of the GSZ sharply contrast with the overwhelmingly normal-shear, non-segmented ASZ and SPSZ; the GSZ contributed little to exhumation of the gneiss domes but signifies lateral, along-strike displacement (section 7.2.5).

Our geo-thermochronology (Figures 4, 5, and S5) constrains the onset of tectonic exhumation and cooling along the GSZ to after 27–21 Ma (ZUPb ages of pre-tectonic leucogranites); Sil-bearing, high-temperature deformation of the pegmatite mylonite observed at station 4726H indicates late syn-intrusive flow, possibly constraining it to  $\leq 20.5$  Ma (the pegmatite-dike-emplacment age). The evenly distributed intermediate-temperature ages over the  $\sim 50$ –20 Ma range may trace the thermal evolution of the uppermost South Pamir crust during the Paleogene: isothermal holding or very slow cooling ( $\sim 1$  °C/Myr). This implies little shortening/erosion of the upper crust in this part of the Pamir, consistent with the findings of Rutte, Ratschbacher, Schneider, et al. (2017) and Chapman, Robinson, et al. (2018) in the eastern South Pamir.

Bulk-average cooling rates differ between the eastern ( $\sim 11$  °C/Myr,  $\sim 340$ –120 °C,  $\sim 27$ –7 Ma) and western GSZ ( $\sim 22$  °C/Myr,  $\sim 340$ –130 °C,  $\sim 15$ –8 Ma; Figure 6a) and are lower than in the Alichur ( $\sim 42$  °C/Myr) and Shakh dara domes ( $\sim 60$  °C/Myr). The two best-studied sections in the western GSZ further emphasize that the GSZ segments may have followed variable exhumation/cooling histories; there, pooled-sample cooling rates are higher—43–34 °C/Myr—between  $\sim 17$ –8 Ma. Taking all dates younger than 20 Ma from the entire GSZ, we observe that the Wm/BtAr, ZHe, and AFT dates cluster in comparatively narrow ranges, with medians at 13.7, 12.0, and 7.2 Ma and average  $T_c$  of  $\sim 320$ , 190, and 130 °C, respectively. This may imply more rapid cooling (up to 75 °C/Myr) earlier ( $> \sim 12$  Ma) in the cooling history than in the later history ( $\sim 13$  °C/Myr; Figure S5). Common to all segments of the GSZ is a decrease in exhumation/cooling rates some time after 9–7 Ma; this is reflected in both the cooling rates derived from the regressions of age vs.  $T_c$  and the exhumation rates derived from age vs. elevation data. This qualitatively conforms with the structural evolution of the GSZ, with an earlier and more pronounced normal-slip and later more important strike-slip history. Most importantly, our geo-thermochronology indicates temporal overlap between the ASZ and the GSZ activities.

#### 7.2.5. The Shakh dara–Alichur Gneiss-Dome Complex

Because the Alichur and Shakh dara domes were exhumed coevally along normal-sense shear zones and jointly accommodated roughly convergence-parallel extension in the South Pamir over a spatially continuous region, we concur with Stübner, Ratschbacher, Rutte, et al.'s (2013) view that the domes represent a kinematically linked structure with a common origin: the  $\sim 350$  km-long Shakh dara–Alichur gneiss-dome complex (Figures 1 and 7a). The normal-sense shear zones that bound the complex contributed unequally to the bulk exhumation; the SPSZ accommodated the majority, and the ASZ and GSZ accommodated the minority. This relationship is illustrated in the western two thirds of the gneiss-dome complex (the Shakh dara dome), where structural observations and cooling-age patterns attest to the dominance of the SPSZ and the subordination of the GSZ in exhuming this component of the gneiss dome complex from  $\geq 50$  km depth (Hacker et al., 2017). For the eastern third of the complex (the Alichur dome), the ASZ accommodated the majority of the footwall exhumation. Finally, in addition to exhumation from shallower depths, our  $\sim 1.1$  km/Myr bulk-average exhumation-rate estimate for the Alichur dome (Figure 6) indicates that it was exhumed up to three times more slowly than the Shakh dara dome (1–3 km/Myr; (Hacker et al., 2017; Stübner, Ratschbacher, Weise, et al., 2013).

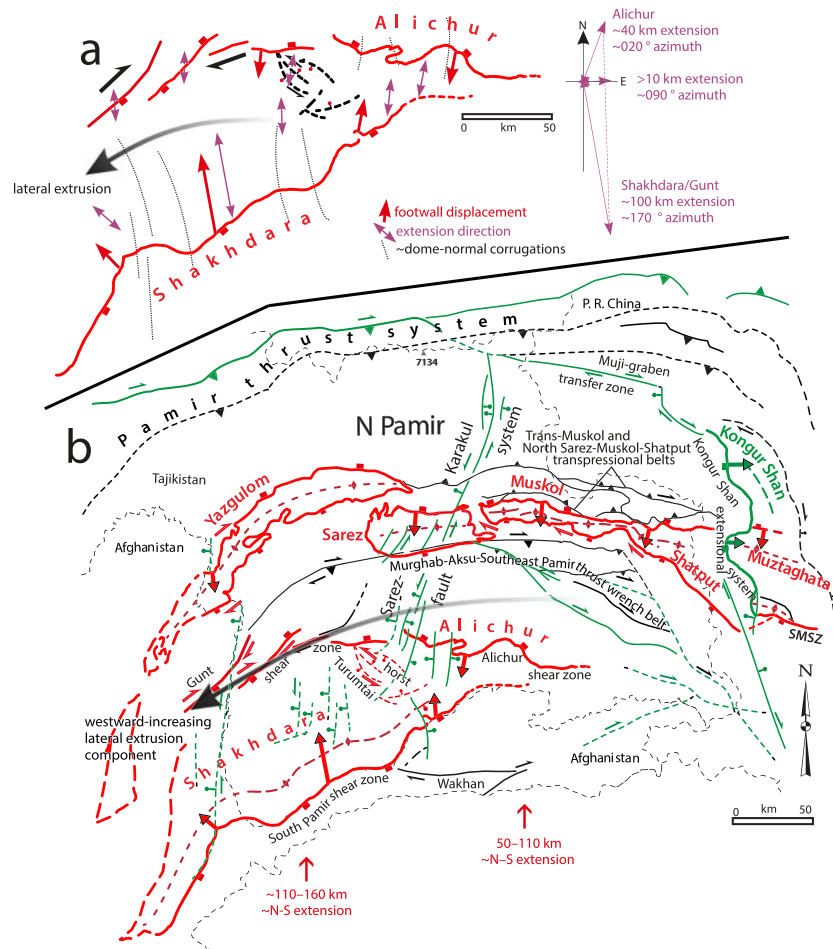


**Figure 7.** (a) Structural-kinematic framework of the Shakhdara–Alichur gneiss-dome complex highlighting dominant ~N–S extension along detachment faults (red) and minor ~E–W extension and dextral wrenching along secondary structures (black). Footwall displacement vectors and extension directions along the detachments are grossly scaled for the variable along-strike displacement/strain of the gneiss-dome complex. Azimuthal divergence in displacement/strain is highlighted in the vector diagram to the right, employing maximum values for extension. The Turumtai horst is a low-strain relay bridge between the Shakhdara and Alichur domes and accommodates extension at the eastern terminus of the Gunt shear zone (GSZ). The segmented GSZ, likely with mostly normal displacements in its early history, is one of several dextral shear zones mapped from the Wakhan of Afghanistan in the south to the Central Pamir in the north (Rutte, Ratschbacher, Schneider, et al., 2017; Stübner, Ratschbacher, Rutte, et al., 2013) (see panel b). The dome-normal corrugations are mega-boudins indicating minor ~E–W extension. Relative to the weakly deformed crust of the eastern South Pamir (east of the Alichur dome), the boudinage and wrenching accommodate a westward-increasing flow component—westward lateral extrusion—of the Pamir plateau crust, secondary to the dominant northward material flow. (b) The Neogene gneiss-dome system of the Central and South Pamir (in red) and the fault network of the neotectonic deformation field (in green). Faults in black have unknown timing or formed at an intermediate stage, and have overwhelmingly dextral-transpressive kinematics. Major fault zones discussed in the text are named. Cumulative ~N–S extension across the gneiss domes (bottom) is larger in the west (Shakhdara–Yazgulom transect) than east (Alichur–Muskol transect). Whereas a westward-increasing lateral-extrusion component for the neotectonic deformation field is given by the ~N-striking normal-fault systems and dextral strike-slip component along the Pamir thrust system, that for the Neogene deformation field is traced by the mega-boudin structure of the domes and the distributed wrench belts in the Central and South Pamir.

The difference between the bulk stretching-lineation trajectories for the SPSZ (~170°) and the ASZ (~020°) implies that lateral divergence between the hanging walls of the SPSZ and ASZ was asymmetric and ~30° oblique; this divergence requires an ~E–W stretch of the entire complex (Figure 7a). We showed that activities of the mostly dextral shear GSZ and the mostly normal-shear ASZ and SPSZ temporally overlap. As the former implies a strong component of along-strike material flow, it also imposes an ~E–W stretch on the

entire complex. Because the structural data require that the oblique divergence in the Shakh dara–Alichur gneiss-dome complex could not have been accommodated by the SPSZ and ASZ themselves, we propose that a kinematically linked network of structures accommodated bulk along-strike extension. First, kinematic linkage between the sinistral oblique-normal shear zones/faults of the northwestern Turumtai horst and the dextral eastern GSZ suggests that this structure accommodated some along-strike extension at its eastern terminus together with taking up the divergence in slip between the SPSZ and ASZ. Second, we collectively interpret the ~N-trending corrugations mapped in both the Shakh dara and Alichur domes (Figure 7a), the culminations and depressions in the crest line of the Shakh dara dome (Stübner, Ratschbacher, Rutte, et al., 2013), and their regional expression in the plunging folds (e.g., in the ASZ, the open, E-trending Tuzkul anticline and the doubly plunging N-Alichur culmination) as expressions of dome-scale pinch-and-swell structures that indicate long-lived, minor along-strike extension. Finally, we note that ~000°-trending stretching lineations in the northern SPSZ in the upper Shakh dara valley (Stübner, Ratschbacher, Rutte, et al., 2013) record earlier exhumation of the Shakh dara dome than the southern SPSZ and may reflect a 10° westward shift in the footwall exhumation azimuth from early footwall exhumation to the N to late footwall exhumation to the NNW. We interpret this to reflect broader, along-strike extension of the Shakh dara–Alichur gneiss-dome complex.

#### 7.2.6. Neotectonic E–W Extension in the Alichur Region

Broadly ~N-striking, high-angle, normal-oblique faults cut all Neogene structures that exhumed the South-Central Pamir domes via ~N–S extension. Relevant to the Alichur region is the ~NNE-striking, sinistral-normal SKFS (Figures 1 and 7b), which is well-developed in the North and Central Pamir as a concentrated fault zone. It extends into the South Pamir as a more-diffuse network of en echelon, right-stepping, faults (Metzger et al., 2017; Schurr et al., 2014). The high-angle normal faults that we map in the western Alichur and eastern Shakh dara regions cut all older structures and are consistent with the neotectonic stress field (Figure 2a). It is not presently clear whether the youngest, ~4 Ma AFT ages in the Alichur dome signify: (i) The termination of ~N–S extension along the ASZ and a local oldest-age constraint for onset of ~E–W extension; (ii) Unresolved continuation of ~N–S extension along the ASZ that would imply a younger onset of ~E–W extension; or (iii) Footwall exhumation along unmapped, N-striking, high-angle brittle normal faults that would imply an earlier onset of ~E–W extension.

### 7.3. The Role of the Shakh dara–Alichur Gneiss-Dome Complex in the Evolution of the Pamir

#### 7.3.1. Boundary Conditions From the Central and South Pamir

What are the similarities and differences between the Central and South Pamir gneiss-dome complexes? The preeminent similarity is the approximately N–S, syn-collisional extension that exhumed all the domes. Superimposed is a north(out-)ward-convex fanning of the extension azimuths, which define a much less tight northward-convex curvature than that for the Pamir orocline (see the azimuths of the Yazgulom dome and Shen-ti klippe of the Muztaghata dome; Figures 1 and 7b) (Rutte, Ratschbacher, Schneider, et al., 2017; Stearns et al., 2015; Stübner, Ratschbacher, Rutte, et al., 2013). In addition, petrochronology shows that the switch from prograde to retrograde metamorphism occurred at ~20 Ma throughout an area that encompasses the Pamir gneiss domes and the Karakorum (Hacker et al., 2017; Palin et al., 2012). One significant difference among the Pamir gneiss domes is their variable magnitudes of syn-collisional ~N–S extension, which vary along the strike of the orogen. Rutte, Ratschbacher, Schneider, et al. (2017) estimated 20–70 km extension for the eastern Central Pamir domes (Sarez–Muskol–Shatput); our unpublished structural work suggests similar amounts for the western Central Pamir Yazgulom dome. The Alichur and Shakh dara domes accommodated, respectively, 30–40 km and ~90 km of extension (this study; Stübner, Ratschbacher, Rutte, et al., 2013). This highlights an orogen-parallel, ~westward increase in ~N–S extension across the central South Pamir from 50–110 km at the longitudes of the Sarez–Muskol–Shatput and Alichur domes to 110–160 km at the longitudes of the Yazgulom and central Shakh dara domes (Figure 7b).

Another prominent trend that our investigation reinforces is the southward younging of cooling ages and the cessation of ~N–S extension. Cooling through intermediate–low temperatures is 2–3 Myr younger for the South Pamir domes than for the Central Pamir domes (Figure 5; Hacker et al., 2017; Rutte, Ratschbacher, Khan, et al., 2017; This study). The pattern is clearest for the WmAr/BtAr systems in the Shatput–Muskol–Sarez and Alichur domes, for which 18–13 Ma vs. 16–11 Ma cooling-age ranges indicate a 2 Myr-southward younging of the 5 Myr duration of convergence-parallel gneiss-dome exhumation through WmAr/BtAr closure. Broad southward younging of WmAr ages observed in the modern detrital record

corroborate the bedrock-based observations (Carrapa et al., 2014). An analogous pattern of 3 Myr-southward younging of the 6 Myr ZHe cooling age durations for the 16–10 and 13–7 Ma cooling-age ranges for the Muskol and Alichur domes corroborates the intermediate-temperature-closure observation. Whereas approximately N-S extension was replaced by shortening at ~12 Ma in the Central Pamir, it continued to ~4 Ma in the Alichur dome and to 4–2 Ma in the Shakh dara dome.

Our study also reinforces differences in the gneiss-dome exhumation rates between the Central and South Pamir. The Central Pamir domes record broadly faster tectonic exhumation (2–5 km/Myr) from mid-crustal depths (25–35 km) than the Shakh dara–Alichur gneiss dome-complex (1–3 km/Myr) from lower–upper-crustal depths (10–55 km) (Stübner, Ratschbacher, Weise, et al., 2013; Hacker et al., 2017; Rutte, Ratschbacher, Khan, et al., 2017; This study). Cooling rates estimated from multi-method thermochronology span 32–147 °C/Myr for the Central Pamir Muskol–Shatput domes (Rutte, Ratschbacher, Khan, et al., 2017) and are generally higher than those for the South Pamir domes, which span 30–90 °C/Myr for the Shakh dara dome (Stearns et al., 2015; Stübner, Ratschbacher, Weise, et al., 2013) and 22–79 °C/Myr (bulk-average ~42 °C/Myr) for the Alichur dome (this study; Figures 6b and S5).

### 7.3.2. Connection to Lithospheric Processes

Our refinement of the structural geometry of the Shakh dara–Alichur gneiss-dome complex and the timing of the development of the Alichur dome and GSZ prompts us to refine our previously proposed geodynamic model for the tectonic evolution of the Central and South Pamir (section 1; Figures 8a–8f; Rutte, Ratschbacher, Khan, et al., 2017; Hacker et al., 2017, and references therein). The Paleogene development is characterized by prograde metamorphism ( $\geq 37$ –20 Ma) during crustal thickening (Figures 5, 8a, and 8b). Approximately E–W extension accompanied crustal thickening. Apparently dissimilar magnitudes of upper-crustal shortening for the Central and South Pamir are likely effects of heterogeneous strain accumulation. The highly shortened Central Pamir crustal stack implies coupled upper- and lower-crustal thickening that can account for tectonic burial of the Central Pamir dome rocks to 25–35 km depth; it may have developed along the southern margin of cratonic Asia (Rutte, Ratschbacher, Schneider, et al., 2017). By contrast, the minor upper-crustal shortening documented in the South Pamir thrust belt (Chapman, Robinson, et al., 2018), across a part of the South Pamir batholith, is insufficient to account for tectonic burial of the Shakh dara–Alichur gneiss-dome rocks to 10–55 km depth. This implies locally decoupled upper- and lower-crustal thickening for parts of the South Pamir. We speculate that enhanced shortening was partitioned away from the rheologically rigid South Pamir batholith to its margins, that is, the Rushan–Pshart thrust-fold belt between the Central and South Pamir and the thrust-fold belt along the Tirich–Kilik suture in the Karakorum.

Following our previous interpretation, we propose that break-off of northward subducting Greater Indian lithosphere at 25–20 Ma induced two geodynamic changes in the possibly >90-km-thick Pamir plateau (Rutte, Ratschbacher, Schneider, et al., 2017) that drove its gravitational collapse: (i) An unstable surplus of gravitational potential energy; and (ii) Asthenospheric-upwelling-derived heating. In this regard, two coeval tectonic events induced the Neogene gravitational collapse of the Pamir plateau and a northward migration of the deformation front: (i) The extensional exhumation of the South–Central Pamir gneiss-dome system; and (ii) Shortening in the Tajik–Tarim fold-and-thrust belt along the northern margin of the North Pamir (the Tajik–Tarim foreland). Considering the heating-induced increases in buoyancy and partial-melt abundance in the Pamir plateau and a weak Tajik–Tarim foreland upper crust, these symptoms suggest coupling between the ~20–12 Ma extension in the Pamir plateau and coeval shortening in the Tajik–Tarim fold-thrust belt, reflecting “gravitational sliding” of the former Pamir plateau margin onto the Tajik–Tarim foreland (Figures 8c and 8d; Rey et al., 2010). With respect to the South Pamir, earlier termination of ~N–S extension in the Central Pamir can be attributed to its position at the former northern periphery of the Pamir plateau, where the thick, hot crust would have transitioned northward into the cold, thin Tajik–Tarim foreland. In this regard, rapid cooling of the hot, northward-flowing, Central Pamir lower–middle crust as it propagated into the cold Tajik–Tarim foreland is expected to have impeded gneiss-dome exhumation.

What allowed ~N–S extension to terminate earlier (~12 Ma) in the Central Pamir, and why did extension in the South Pamir domes proceed to ~4 Ma (Alichur dome) and 4–2 Ma (Shakh dara dome)? Basal shear imposed by underthrusting Indian lithosphere was demonstrably significant in the construction of the Tibet plateau (e.g., Willett & Beaumont, 1994). Geodynamic modeling illustrates that basal shear associated with rigid Indian lithosphere underthrusting Tibet interacts differently with the indentation-related,

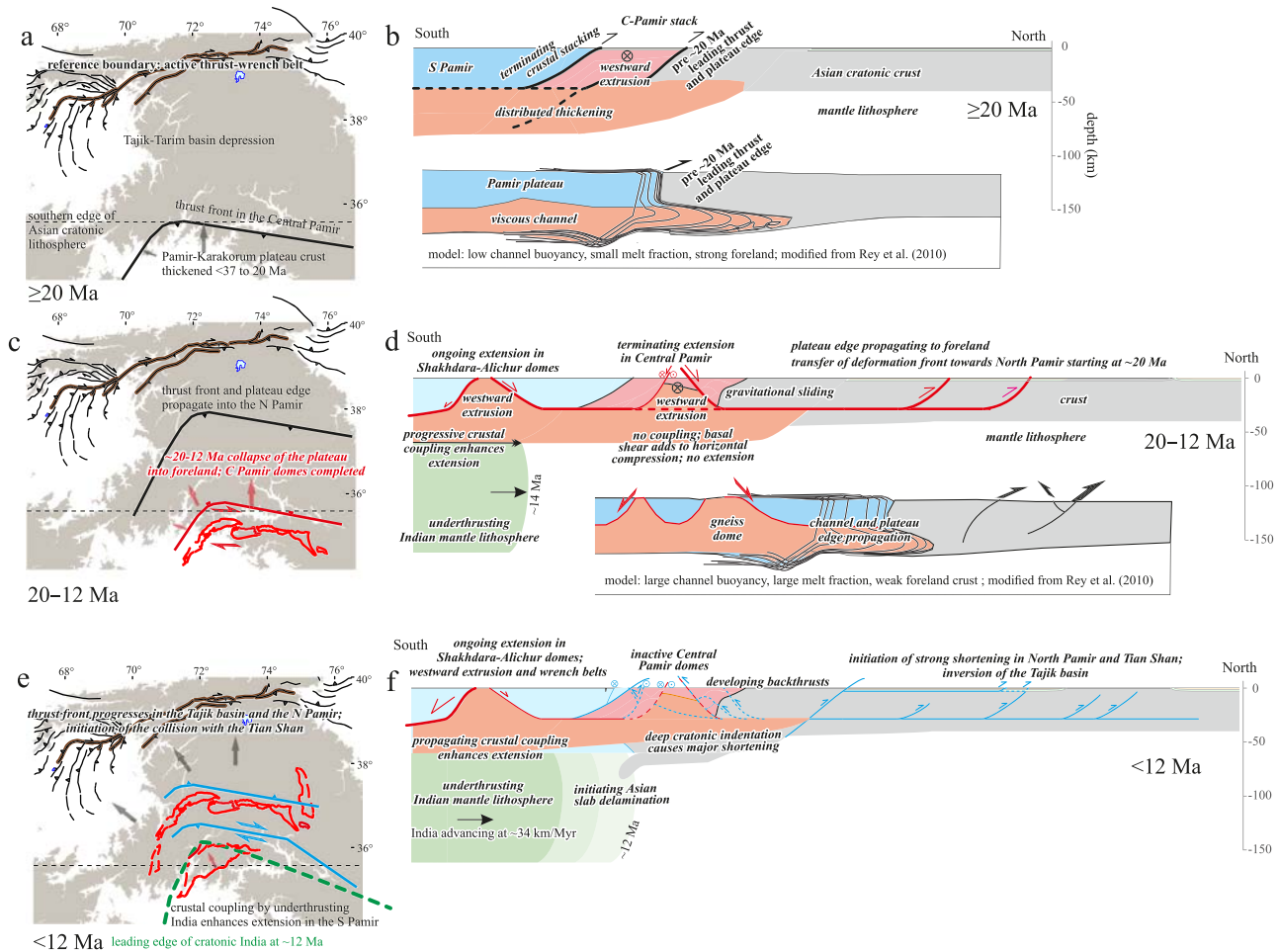


**Figure 8.** Geodynamic model for the evolution of the Central and South Pamir, refined from Rutte, Ratschbacher, Khan, et al. (2017). (a and b) The  $\geq 37$ –20 Ma development was characterized by crustal thickening resulting in up to 90 km-thick crust, the formation of the Pamir plateau, and the generation of a viscous channel beneath the plateau. Low channel buoyancy, a small melt fraction, and a strong foreland upper crust favored foreland-directed channel-flow extrusion beneath the plateau (Rey et al., 2010). The leading edge of the Pamir plateau was located along the Central Pamir. (c and d) Indian slab breakoff at 25–20 Ma changed the channel properties. The heat input and the regional migmatization documented in the exposed South Pamir lower–middle crust inhibited channel flow, favoring core-complex formation in the Pamir plateau (the Central and South Pamir gneiss domes). The collapse of the Pamir crust from ~21 Ma onward relocated the deformation front from the Central Pamir to the North Pamir. Earlier termination of ~N–S extension in the Central Pamir with respect to the South Pamir is attributed to its position at the former northern periphery of the Pamir plateau, where the thick, hot crust was transitioned northward into the cold, thin Tajik–Tarim foreland. At ~12 Ma, the formation of the Central Pamir gneiss domes was completed. After the 25- to 20-Ma break-off of Greater Indian lithosphere, the India–Asia convergence was characterized by underthrusting (Kufner et al., 2016). The resulting strong coupling between underthrusting Indian lower crust and overlying Asian crust (Copley et al., 2011; Liu & Yang, 2003) enhanced ~N–S extension in the underthrust South Pamir (where it continued until ~4–2 Ma) and inhibited ~N–S extension in the non-underthrust Central Pamir (where it ceased by ~12 Ma). (e and f) Greater ~N–S extension in the Shakh dara dome than in the Alichur dome reflects a triangular geometry of the underthrusting Indian promontory, which facilitated stronger coupling beneath the western Pamir than the eastern Pamir. The onset of out-of-sequence thrust-wrenching in the Central Pamir and the northern South Pamir by ~12 Ma reflects the initiation of northward delamination and roll-back of Asian lithosphere by northward bulldozing Indian lithosphere (Kufner et al., 2016). The shear zones in the Central Pamir and northern South Pamir have dominantly top-N kinematics, whereas the exhumation of the Shakh dara dome occurred along the top-SSE South Pamir shear zone (SPSZ). Rey et al.’s (2010) conceptual model of gravitational-collapse-driven plateau growth attributes the Central Pamir top-N collapse to mass transfer by gravitational sliding of the plateau edge onto the foreland (see panel d). The SPSZ constitutes an antithetic shear zone in the orogenic hinterland that accommodated the formation of a large metamorphic-core complex, exposing a weak, formerly northward-flowing lower–middle-crustal channel. The upper crust south of the SPSZ was relatively stationary, whereas the Shakh dara-dome crust spread northward and upward beneath it.

horizontal compressive stresses in the Tibet plateau, producing two deformation regimes: (i) Extension in the southern plateau overlying the underthrusting Indian lithosphere, where basal shear counteracts horizontal compressive stresses; and (ii) Strike-slip deformation in the non-underthrust plateau to the north, where basal shear adds to horizontal compressive stresses (e.g., Copley et al., 2011; Liu & Yang, 2003). In particular, the observation that increasing basal-shear force rotates and narrows extension from

~E–W to ~N–S in southern Tibet may explain the occurrence of the South Tibet detachment system and the North Himalayan gneiss domes, which accommodated ~N–S extension from ~26–13 Ma.

Considering the differential effect of basal shear for the Pamir suggests that India–Asia convergence was characterized by underthrusting (Kufner et al., 2016) after the 25–20 Ma break-off of Greater Indian lithosphere (Figures 8c–8f). Strong coupling between northward-underthrusting Indian lower crust and overlying Asian crust may have enhanced ~N–S extension in the underthrust South Pamir (where it continued until ~4–2 Ma) and inhibited ~N–S extension in the non-underthrust Central Pamir (where it ceased by ~12 Ma). Greater ~N–S extension in the Shakhdara dome than in the Alichur dome may reflect a triangular geometry of the underthrusting Indian promontory, which would have facilitated stronger coupling and basal shear beneath the western Pamir than the eastern Pamir, allowing more extension in the west (Shakhdara) than in the east (Alichur) (Figure 8e). Finally, the onset of out-of-sequence thrust-wrenching in the Central Pamir and the northern South Pamir by ~12 Ma (Rutte, Ratschbacher, Khan, et al., 2017) may reflect the initiation of northward delamination and forced rollback of Asian lithosphere by northward-bulldozing Indian lithosphere (Kufner et al., 2016). The southerly position of the SPSZ, overlying underthrusting Indian lithosphere, likely permitted continued ~N–S extensional exhumation of the Shakhdara dome despite minor ~N–S contractional and/or dextral shear overprinting of the more northerly ASZ and GSZ. In this regard, the ASZ and the GSZ are more akin to the Central Pamir domes, and all signify collapse and foreland propagation of the Pamir plateau.

Why do the dominant shear zones/faults in the Central Pamir and northern South Pamir have top-N kinematics, whereas nearly all the exhumation of the Shakhdara dome occurred along the top-SSE SPSZ? As outlined above, the conceptual model of gravitational-collapse-driven plateau growth attributes the Central Pamir top-N collapse, along with the top-N displacement along the ASZ and GSZ, to mass transfer by gravitational sliding of the plateau edge onto the foreland, exhuming deeper plateau crust in the hinterland. The SPSZ in this scenario constitutes an antithetic shear/fault zone in the orogenic hinterland that accommodated the formation of a large metamorphic-core complex, in which the upper part of a weak, formerly northward-flowing lower–middle-crustal channel is exposed. Compared to the North Pamir, the greater northward distance to the plateau edge implies that crustal extension in the southern hinterland, that is, in the nucleation zone of the Shakhdara dome, was mostly driven by foreland-directed lower–middle-crustal flow, accommodating the northward plateau growth. The rigid upper crust lagged behind and ultimately faulted, re-directing northward-flowing crust upward and exposing it in the SPSZ footwall. This scenario suggests that the upper crust south of the SPSZ—the SPSZ hanging wall—was relatively stationary, whereas the Shakhdara-dome crust spread northward and upward beneath it (Figure 8d and 8f); a similar scenario occurs along the Brenner normal-shear detachment in the Tauern Window of the Eastern Alps (Ratschbacher et al., 1991, p. 261).

Intensified shortening along the North Pamir front and reactivation of the Paleozoic Tian Shan after ~12–10 Ma (e.g., Cheng et al., 2017; Fu et al., 2010; Jepson et al., 2018; Käbner et al., 2016; Thompson et al., 2015), a result of the northward propagation of the collision between cratonic India and cratonic Asia beneath the Pamir, closed the Tajik–Tarim foreland between the Pamir plateau and the Tian Shan. Weak foreland upper crust enhanced by a Jurassic evaporitic décollement in the Tajik-basin depression remained to the west, permitting significant westward material flow (e.g., Nikolaev, 2002). This facilitated the transition to the neotectonic phase of the Pamir, characterized by the interaction of the Pamir with the Tian Shan along the Pamir thrust system and the westward gravitational collapse and lateral extrusion (Figure 8e). The cooling of the gneiss-dome rocks to upper-crustal temperatures rendered them strong by this time, moving the major upper-crustal shortening into the North Pamir, the Tian Shan, and the areas along the dome margins and between the domes (e.g., the Murghab–Aksu–Southeast Pamir thrust-wrench belt). The neotectonic deformation field, ~E–W extension along the SKFS and the KSES, started to dominate when extension in the Pamir gneiss domes had mostly terminated. At this stage, in the latest Miocene–Pliocene, the Pamir frontal thrust system started to accommodate the bulk of India–Asia convergence. The KSES accommodated westward lateral extrusion into the Tajik-basin depression via the Muji-graben transfer system and the dextral strike-slip component in the Pamir frontal-thrust system, and the SKFS started to accommodate both lateral extrusion and the disruption of the Pamir into an eastern, rigidly northward-moving block, and a western block with distributed deformation that moves both northward and collapses westward (resulting in a bulk northwestward motion) into the Tajik-basin depression (Kufner et al., 2018; Metzger et al., 2017; Schurr

et al., 2014). The latest stages of extension in the Shakh dara dome (until its termination at 4–2 Ma) thus may be part of the neotectonic phase; characteristically the youngest extension in the gneiss domes is in the western block, proximal to the Tajik-basin depression.

## 8. Conclusions

The syn-collisional Alichur dome was tectonically exhumed from mid-crustal levels (10–15 km) via convergence-parallel extension in the footwall of the top-NNE, normal-sense, low-angle, mylonitic ASZ between 22–17 and 4 Ma. Broad, ~N-plunging corrugations in the ASZ reflect dome-scale boudinage in which minor ~E–W extension was superimposed on dominant, non-coaxial ~N–S extension (flattening strain). The Alichur-dome leucogranite-injection complex intruded before exhumation and likely originated from buoyancy-driven ascent of anatectic melts, as exposed in-situ along strike to the west in the more deeply exhumed Shakh dara dome. Subsequent monotonic cooling and exhumation of the Alichur dome through 410–130 °C from 16–4 Ma occurred at ~42 °C/Myr and ~1.1 km/Myr. Broad, ~E-trending folding reflects minor, post-~N–S extensional, ~N–S shortening coeval with ~E–W extension that accommodated westward lateral extrusion of the Pamir.

Longer-lasting, faster, and higher-magnitude exhumation of the kinematically linked Shakh dara dome along the South Pamir shear zone (SPSZ) from 21–2 Ma reflects more-significant tectonic exhumation than that of the Alichur dome along the ASZ. The Gunt shear/fault zone (GSZ) bounds the Shakh dara dome to the north and is connected to the ASZ via the Turumtai horst, which itself is a weakly extended relay bridge between the Shakh dara and Alichur domes. It accommodated a part of the ~E–W flow of the Pamir plateau crust.

Basin relicts in the proximal hanging wall of the SPSZ and ASZ corroborate the kinematics and timing of ~N–S extension along these detachments. Detrital-zircon U/Pb geochronology for sandstones and mica <sup>40</sup>Ar/<sup>39</sup>Ar thermochronology for a granitic conglomerate clast from pre-extensional and syn-extensional strata in the Zebak proximal hanging wall basin of the southwestern Shakh dara dome assign: (i) A <63 Ma age to pre-extensional strata, which include clasts that resemble the upper-crustal rock association of the Shakh dara–Alichur region (including the South Pamir batholith); and (ii) A <16 Ma age to syn-extensional strata, which include mylonite and leucogranite-gneiss clasts that resemble the dome interiors.

Southward-younging ~N–S-extensional gneiss-dome exhumation from the Central Pamir to the South Pamir reflects: (i) The predominantly northward, foreland-directed flow of hot crust into a cold foreland during the growth of the Pamir orocline; and (ii) The contrasting effect of basal shear related to underthrusting Indian lithosphere in enhancing extension in the underthrust South Pamir and inhibiting extension in the non-underthrust Central Pamir.

The Central Pamir top-N collapse, along with the top-N displacement along the ASZ and GSZ, reflects early Miocene mass transfer by gravitational sliding of the Pamir plateau edge onto the Tajik–Tarim foreland. The top-SSE SPSZ constitutes an antithetic shear/fault zone in the orogenic hinterland that accommodated the formation of a large metamorphic-core complex, in which the upper part of a weak, formerly northward-flowing lower–middle-crustal channel is exposed. The rigid upper crust lagged behind and ultimately faulted, re-directing northward-flowing crust upward and exposing it in the SPSZ footwall. This scenario suggests that the upper crust south of the SPSZ was relatively stationary, whereas the Shakh dara-dome crust spread northward and upward beneath it.

## References

- Aizen, E. M., Aizen, V. B., Melack, J. M., Nakamura, T., & Ohta, T. (2001). Precipitation and atmospheric circulation patterns at mid-latitudes of Asia. *International Journal of Climatology*, *21*(5), 535–556. <https://doi.org/10.1002/joc.626>
- Aminov, J., Ding, L., Mamadjonov, Y., Dupont-Nivet, G., Aminov, J., Zhang, L.-Y., et al. (2017). Pamir Plateau formation and crustal thickening before the India-Asia collision inferred from dating and petrology of the 110–92 Ma Southern Pamir volcanic sequence. *Gondwana Research*, *51*(Supplement C), 310–326. <https://doi.org/10.1016/j.gr.2017.08.003>
- Angiolini, L., Zanchi, A., Zanchetta, S., Nicora, A., & Vezzoli, G. (2013). The Cimmerian geopuzzle: New data from South Pamir. *Terra Nova*, *25*(5), 352–360. <https://doi.org/10.1111/ter.12042>
- Angiolini, L., Zanchi, A., Zanchetta, S., Nicora, A., Vuolo, I., Berra, F., et al. (2015). From rift to drift in South Pamir (Tajikistan): Permian evolution of a Cimmerian terrane. *Journal of Asian Earth Sciences*, *102*, 146–169. <https://doi.org/10.1016/j.jseas.2014.08.001>
- Arnaud, N. O., Brunel, M., Cantagrel, J. M., & Tapponnier, P. (1993). High cooling and denudation rates at Kongur-Shan, Eastern Pamir (Xinjiang, China) revealed by <sup>40</sup>Ar/<sup>39</sup>Ar Alkali Feldspar Thermochronology. *Tectonics*, *12*(6), 1335–1346. <https://doi.org/10.1029/93tc00767>

## Acknowledgments

Funded by DFG bundle TIPAGE (PAK 443); BMBF bundle CAME project TIPTIMON (Support Code 03G0809); NSF Grant EAR-1419748; ExxonMobil; Geological Society of America; American Association of Petroleum Geologists; University of Arizona Coney fund; and Conoco Phillips scholarship. The Arizona Laserchron Center was funded by NSF Instrumentation & Facilities Grant EAR-1338583. A Fulbright Fellowship enabled J. W.'s research at TU Bergakademie Freiberg. Reviews by A. Robinson and an anonymous reviewer and editorial handling by M. Jolivet and M.E. Rusmore improved this manuscript. We are grateful to the following individuals for providing analytical assistance: B. Sperner (Argonlab Freiberg); M. Hofmann and U. Linnemann (Senckenberg Labs); M. Pecha, N. Geisler, K. Plange, M. Pepper, and C. White (Arizona Laserchron Center); A. R. C. Kylander-Clark (UCSB LASS Lab); U. Chowdhury (Arizona Radiogenic Helium Dating Lab); and Z. Zajacz (University of Toronto Fluid Inclusion Lab). Discussions with the GFZ Potsdam Pamir group (in particular S.-K. Kufner and B. Schurr), V. Minaev, B. Carrapa, P. DeCelles, M. Ducea, P. Reiners, K. Murray, S. Thompson, G. Gehrels, G. Davis, and J.-P. Avouac improved this work. Our new data are available in Tables S1–S9 and Data Sets S1–S4 of the Supporting Information and at the Open Science Framework ([https://osf.io/u6zha/?view\\_only=abe312f95192412584669-da2f80e92c3](https://osf.io/u6zha/?view_only=abe312f95192412584669-da2f80e92c3)). All cited data are available in referenced publications.

- Arrowsmith, J. R., & Strecker, M. R. (1999). Seismotectonic range-front segmentation and mountain-belt growth in the Pamir-Alai region, Kyrgyzstan (India-Eurasia collision zone). *Geological Society of America Bulletin*, *111*(11), 1665–1683. [https://doi.org/10.1130/0016-7606\(1999\)111<1665:srsam>2.3.co;2](https://doi.org/10.1130/0016-7606(1999)111<1665:srsam>2.3.co;2)
- Bakker, R. J. (1997). Clathrates: Computer programs to calculate fluid inclusion VX properties using clathrate melting temperatures. *Computers & Geosciences*, *23*(1), 1–18.
- Bodnar, R. J., & Bethke, P. M. (1984). Systematics of stretching of fluid inclusions. I. Fluorite and sphalerite at 1 atmosphere confining pressure. *Economic Geology*, *79*(1), 141–161. <https://doi.org/10.2113/gsecongeo.79.1.141>
- Bodnar, R. J., Lecumberri-Sanchez, P., Moncada, D., & Steele-MacInnis, M. (2014). Fluid inclusions in hydrothermal ore deposits. In H. D. Holland & K. K. Turekian (Eds.), *Treatise on Geochemistry* (Second ed., pp. 119–142). Oxford: Elsevier.
- Bodnar, R. J., Samson, I., Anderson, A., & Marshall, D. (2003). Reequilibration of fluid inclusions. *Fluid inclusions: Analysis and Interpretation*, *32*, 213–230.
- Brandon, M. T., Roden-Tice, M. K., & Garver, J. I. (1998). Late Cenozoic exhumation of the Cascadia accretionary wedge in the Olympic Mountains, northwest Washington State. *Geological Society of America Bulletin*, *110*(8), 985–1009. [https://doi.org/10.1130/0016-7606\(1998\)110<0985:lceotc>2.3.co;2](https://doi.org/10.1130/0016-7606(1998)110<0985:lceotc>2.3.co;2)
- Brunel, M., Arnaud, N., Tapponnier, P., Pan, Y., & Wang, Y. (1994). Kongur-Shan normal-fault—Type example of mountain building assisted by extension (Karakoram Fault, Eastern Pamir). *Geology*, *22*(8), 707–710. [https://doi.org/10.1130/0091-7613\(1994\)022<0707:Ksnfte>2.3.Co;2](https://doi.org/10.1130/0091-7613(1994)022<0707:Ksnfte>2.3.Co;2)
- Burtman, V. S., & Molnar, P. (1993). Geological and geophysical evidence for deep subduction of continental crust beneath the Pamir. *Geological Society of America Special Papers*, *281*, 1–76. <https://doi.org/10.1130/SPE281-p1>
- Cai, Z., Xu, Z., Cao, H., Robinson, A. C., Li, G., & Xu, X. (2017). Miocene exhumation of northeast Pamir: Deformation and geo/thermochronological evidence from western Muztaghata shear zone and Kuke ductile shear zone. *Journal of Structural Geology*, *102*, 130–146. <https://doi.org/10.1016/j.jsg.2017.07.010>
- Cao, K., Bernet, M., Wang, G.-C., van der Beek, P., Wang, A., Zhang, K.-X., & Enkelmann, E. (2013). Focused Pliocene–Quaternary exhumation of the Eastern Pamir domes, western China. *Earth and Planetary Science Letters*, *363*, 16–26. <https://doi.org/10.1016/j.epsl.2012.12.023>
- Cao, K., Wang, G.-C., van der Beek, P., Bernet, M., & Zhang, K.-X. (2013). Cenozoic thermo-tectonic evolution of the northeastern Pamir revealed by zircon and apatite fission-track thermochronology. *Tectonophysics*, *589*, 17–32. <https://doi.org/10.1016/j.tecto.2012.12.038>
- Carlson, W. D., Donelick, R. A., & Ketcham, R. A. (1999). Variability of apatite fission-track annealing kinetics: I. Experimental results. *American Mineralogist*, *84*(9), 1213–1223.
- Carrapa, B., Shazanee Mustapha, F., Cosca, M., Gehrels, G., Schoenbohm, L. M., Sobel, E. R., et al. (2014). Multisystem dating of modern river detritus from Tajikistan and China: Implications for crustal evolution and exhumation of the Pamir. *Lithosphere*, *6*, 443–455. <https://doi.org/10.1130/L360.1>
- Cassata, W. S., & Renne, P. R. (2013). Systematic variations of argon diffusion in feldspars and implications for thermochronometry. *Geochimica et Cosmochimica Acta*, *112*, 251–287. <https://doi.org/10.1016/j.gca.2013.02.030>
- Chapman, J. B., Robinson, A. C., Carrapa, B., Villarreal, D., Worthington, J., DeCelles, P. G., et al. (2018). Cretaceous shortening and exhumation history of the South Pamir terrane. *Lithosphere*, *10*(4), 494–511. <https://doi.org/10.1130/L691.1>
- Chapman, J. B., Scoggin, S. H., Kapp, P., Carrapa, B., Ducea, M. N., Worthington, J., et al. (2018). Mesozoic to Cenozoic magmatic history of the Pamir. *Earth and Planetary Science Letters*, *482*, 181–192. <https://doi.org/10.1016/j.epsl.2017.10.041>
- Chen, M., Xie, P., Janowiak, J. E., & Arkin, P. A. (2002). Global land precipitation: A 50-yr monthly analysis based on gauge observations. *Journal of Hydrometeorology*, *3*(3), 249–266.
- Cheng, X., Chen, H., Lin, X., Wu, L., & Gong, J. (2017). Geometry and kinematic evolution of the Hotan-Tiklik segment of the Western Kunlun Thrust Belt: Constrained by structural analyses and apatite fission track thermochronology. *The Journal of Geology*, *125*(1), 65–82. <https://doi.org/10.1086/689187>
- Cole, J., Hacker, B., Ratschbacher, L., Dolan, J., Seward, G., Frost, E., & Frank, W. (2007). Localized ductile shear below the seismogenic zone: Structural analysis of an exhumed strike-slip fault, Austrian Alps. *Journal of Geophysical Research*, *112*, B12304. <https://doi.org/10.1029/2007JB004975>
- Coney, P. J., & Harms, T. A. (1984). Cordilleran metamorphic core complexes—Cenozoic extensional relics of Mesozoic compression. *Geology*, *12*(9), 550–554. [https://doi.org/10.1130/0091-7613\(1984\)12<550:Cmccce>2.0.Co;2](https://doi.org/10.1130/0091-7613(1984)12<550:Cmccce>2.0.Co;2)
- Copley, A., Avouac, J.-P., & Wernicke, B. P. (2011). Evidence for mechanical coupling and strong Indian lower crust beneath southern Tibet. *Nature*, *472*, 79. <https://doi.org/10.1038/nature09926>
- Coutand, I., Strecker, M. R., Arrowsmith, J. R., Hilley, G., Thiede, R. C., Korjenkov, A., & Omuraliev, M. (2002). Late Cenozoic tectonic development of the intramontane Alai Valley, (Pamir-Tien Shan region, central Asia): An example of intracontinental deformation due to the Indo-Eurasia collision. *Tectonics*, *21*(6), 1053. <https://doi.org/10.1029/2002tc001358>
- Dalrymple, G. B., & Lanphere, M. A. (1969). Potassium-argon dating: Principles, techniques and applications to geochronology, in *(Freeman) San Francisco, California* (p. 258).
- de Sigoyer, J., Guillot, S., & Dick, P. (2004). Exhumation of the ultrahigh-pressure Tso Moriri unit in eastern Ladakh (NW Himalaya): A case study. *Tectonics*, *23*, TC3003. <https://doi.org/10.1029/2002TC001492>
- Desio, A. (1975). Geology of central Badakhshan (North-east Afghanistan) and surrounding countries: Italian expeditions to the Karakorum (K2) and Hindu Kush, EJ Brill.
- Diamond, L. W., & Tarantola, A. (2015). Interpretation of fluid inclusions in quartz deformed by weak ductile shearing: Reconstruction of differential stress magnitudes and pre-deformation fluid properties. *Earth and Planetary Science Letters*, *417*, 107–119. <https://doi.org/10.1016/j.epsl.2015.02.019>
- Dodson, M. H. (1973). Closure temperature in cooling geochronological and petrological systems. *Contributions to Mineralogy and Petrology*, *40*(3), 259–274. <https://doi.org/10.1007/Bf00373790>
- Donelick, R. A., Ketcham, R. A., & Carlson, W. D. (1999). Variability of apatite fission-track annealing kinetics: II. Crystallographic orientation effects. *American Mineralogist*, *84*(9), 1224–1234.
- Donelick, R. A., O'Sullivan, P. B., & Ketcham, R. A. (2005). Apatite fission-track analysis. *Reviews in Mineralogy and Geochemistry*, *58*(1), 49–94. <https://doi.org/10.2138/rmg.2005.58.3>
- Dronov, V. L., Melnikova, G. K., Salibajev, G. C., Bardashev, I. A., Minaev, V., & Muchabatov, M. M. (2006). *Stratigraphic Dictionary of the Pamirs* (p. 252). Freiberg: Technische Universität Bergakademie.
- Duan, Z., Moller, N., & Weare, J. H. (1995). Equation of state for the NaCl–H<sub>2</sub>O–CO<sub>2</sub> system: Prediction of phase equilibria and volumetric properties. *Geochimica et Cosmochimica Acta*, *59*(14), 2869–2882.

- Ehlers, T. A., Chaudhri, T., Kumar, S., Fuller, C. W., Willett, S. D., Ketcham, R. A., et al. (2005). Computational tools for low-temperature thermochronometer interpretation. *Reviews in Mineralogy and Geochemistry*, 58(1), 589–622. <https://doi.org/10.2138/rmg.2005.58.22>
- Farley, K. A. (2000). Helium diffusion from apatite: General behavior as illustrated by Durango fluorapatite. *Journal of Geophysical Research*, 105(B2), 2903–2914. <https://doi.org/10.1029/1999JB900348>
- Farley, K. A. (2002). (U-Th)/He dating: Techniques, calibrations, and applications. In D. Porcelli, C. J. Ballentine, & R. Wieler (Eds.), *Noble Gases in Geochemistry and Cosmochemistry* (pp. 819–844). Davos, Switzerland: Symposium on Noble Gases.
- Farley, K. A., Wolf, R. A., & Silver, L. T. (1996). The effects of long alpha-stopping distances on (U-Th)/He ages. *Geochimica et Cosmochimica Acta*, 60(21), 4223–4229. [https://doi.org/10.1016/S0016-7037\(96\)00193-7](https://doi.org/10.1016/S0016-7037(96)00193-7)
- Flowers, R. M., Ketcham, R. A., Shuster, D. L., & Farley, K. A. (2009). Apatite (U-Th)/He thermochronometry using a radiation damage accumulation and annealing model. *Geochimica et Cosmochimica Acta*, 73(8), 2347–2365. <https://doi.org/10.1016/j.gca.2009.01.015>
- Foland, K. A. (1994). Argon diffusion in feldspars. In I. Parsons (Ed.), *Feldspars and their reactions* (pp. 415–447). Dordrecht, Netherlands: Springer.
- Frei, D., & Gerdes, A. (2009). Precise and accurate in situ U–Pb dating of zircon with high sample throughput by automated LA-SF-ICP-MS. *Chemical Geology*, 261(3), 261–270. <https://doi.org/10.1016/j.chemgeo.2008.07.025>
- Fu, B., Ninomiya, Y., & Guo, J. (2010). Slip partitioning in the northeast Pamir–Tian Shan convergence zone. *Tectonophysics*, 483(3), 344–364. <https://doi.org/10.1016/j.tecto.2009.11.003>
- Gehrels, G. E., Valencia, V. A., & Ruiz, J. (2008). Enhanced precision, accuracy, efficiency, and spatial resolution of U–Pb ages by laser ablation–multicollector–inductively coupled plasma–mass spectrometry. *Geochemistry, Geophysics, Geosystems*, 9, Q03017. <https://doi.org/10.1029/2007gc001805>
- Gleadow, A. (1981). Fission-track dating methods: What are the real alternatives? *Nuclear Tracks*, 5(1), 3–14. [https://doi.org/10.1016/0191-278X\(81\)90021-4](https://doi.org/10.1016/0191-278X(81)90021-4)
- Gleadow, A., Harrison, M., Kohn, B., Lugo-Zazueta, R., & Phillips, D. (2015). The Fish Canyon Tuff: A new look at an old low-temperature thermochronology standard. *Earth and Planetary Science Letters*, 424, 95–108. <https://doi.org/10.1016/j.epsl.2015.05.003>
- Grove, M., & Harrison, T. M. (1996). <sup>40</sup>Ar\* diffusion in Fe-rich biotite, in *Am. Miner.* (p. 940).
- Guenthner, W. R., Reiners, P. W., Ketcham, R. A., Nasdala, L., & Giester, G. (2013). Helium diffusion in natural zircon: Radiation damage, anisotropy, and the interpretation of zircon (U-Th)/He thermochronology. *American Journal of Science*, 313(3), 145–198. 10.2475/03.2013.01
- Hacker, B. R., Ratschbacher, L., Rutte, D., Stearns, M. A., Malz, N., Stübner, K., et al. (2017). Building the Pamir–Tibet Plateau–crustal stacking, extensional collapse, and lateral extrusion in the Pamir: 3. Thermobarometry and petrochronology of deep Asian crust. *Tectonics*, 36, 1743–1766. <https://doi.org/10.1002/2017tc004488>
- Hames, W. E., & Bowring, S. A. (1994). An empirical evaluation of the argon diffusion geometry in muscovite. *Earth and Planetary Science Letters*, 124(1), 161–169. [https://doi.org/10.1016/0012-821X\(94\)00079-4](https://doi.org/10.1016/0012-821X(94)00079-4)
- Harrison, M. (1982). Diffusion of <sup>40</sup>Ar in hornblende. *Contributions to Mineralogy and Petrology*, 78(3), 324–331. <https://doi.org/10.1007/bf00398927>
- Hollister, L. S. (1988). On the origin of CO<sub>2</sub>-rich fluid inclusions in migmatites. *Journal of Metamorphic Geology*, 6(4), 467–474.
- Hollister, L. S. (1990). Enrichment of CO<sub>2</sub> in fluid inclusions in quartz by removal of H<sub>2</sub>O during crystal-plastic deformation. *Journal of Structural Geology*, 12(7), 895–901.
- Horton, F., Lee, J., Hacker, B., Bowman-Kamaha'o, M., & Cosca, M. (2015). Himalayan gneiss dome formation in the middle crust and exhumation by normal faulting: New geochronology of Gianbul dome, northwestern India. *Geological Society of America Bulletin*, 127(1–2), 162–180. <https://doi.org/10.1130/b31005.1>
- Hubbard, M. S., Grew, E. S., Hodges, K. V., Yates, M. G., & Pertsev, N. N. (1999). Neogene cooling and exhumation of upper-amphibolite-facies ‘whiteschists’ in the southwest Pamir Mountains, Tajikistan. *Tectonophysics*, 305(1–3), 325–337. [https://doi.org/10.1016/s0040-1951\(99\)00012-8](https://doi.org/10.1016/s0040-1951(99)00012-8)
- Huffman, G. J., Adler, R. F., Arkin, P., Chang, A., Ferraro, R., Gruber, A., et al. (1997). The Global Precipitation Climatology Project (GPCP) combined precipitation dataset. *Bulletin of the American Meteorological Society*, 78(1), 5–20. [https://doi.org/10.1175/1520-0477\(1997\)078<0005:tgpcpg>2.0.co;2](https://doi.org/10.1175/1520-0477(1997)078<0005:tgpcpg>2.0.co;2)
- Huffman, G. J., Adler, R. F., Bolvin, D. T., Gu, G. J., Nelkin, E. J., Bowman, K. P., et al. (2007). The TRMM multisatellite precipitation analysis (TMPA): Quasi-global, multiyear, combined-sensor precipitation estimates at fine scales. *Journal of Hydrometeorology*, 8(1), 38–55. <https://doi.org/10.1175/jhm560.1>
- Hurford, A. J., & Green, P. F. (1983). The zeta-age calibration of fission-track dating. *Isotope Geoscience*, 1(4), 285–317.
- Ischuk, A., Bendick, R., Rybin, A., Molnar, P., Khan, S. F., Kuzikov, S., et al. (2013). Kinematics of the Pamir and Hindu Kush regions from GPS geodesy. *Journal of Geophysical Research: Solid Earth*, 118, 2408–2416. <https://doi.org/10.1002/jgrb.50185>
- Jay, C. N., Flesch, L. M., & Bendick, R. O. (2017). Kinematics and dynamics of the Pamir, Central Asia: Quantifying surface deformation and force balance in an intracontinental subduction zone. *Journal of Geophysical Research: Solid Earth*, 122, 4741–4762. <https://doi.org/10.1002/2017jb014177>
- Jepson, G., Glorie, S., Konopelko, D., Gillespie, J., Danišik, M., Evans, N. J., et al. (2018). Thermochronological insights into the structural contact between the Tian Shan and Pamirs, Tajikistan. *Terra Nova*, 30(2), 95–104. <https://doi.org/10.1111/ter.12313>
- Jonckheere, R., Ratschbacher, L., & Wagner, G. A. (2003). A repositioning technique for counting induced fission tracks in muscovite external detectors in single-grain dating of minerals with low and inhomogeneous uranium concentrations. *Radiation Measurements*, 37(3), 217–219. [https://doi.org/10.1016/s1350-4487\(03\)00029-5](https://doi.org/10.1016/s1350-4487(03)00029-5)
- Käbner, A., Ratschbacher, L., Enkelmann, E., Jonckheere, R., Khan, J., Sonntag, B., et al. (2016). Cenozoic intra-continental deformation and exhumation at the northwestern tip of the India–Asia collision—Southwestern Tian Shan, Tajikistan and Kyrgyzstan. *Tectonics*, 35, 2171–2194. <https://doi.org/10.1002/2015TC003897>
- Ketcham, R. A., Donelick, R. A., & Carlson, W. D. (1999). Variability of apatite fission-track annealing kinetics; III. Extrapolation to geological time scales. *American Mineralogist*, 84(9), 1235–1255.
- Kufner, S.-K., Schurr, B., Ratschbacher, L., Murodkulov, S., Abdulhameed, S., Ischuk, A., et al. (2018). Seismotectonics of the Tajik Basin and Surrounding Mountain Ranges. *Tectonics*, 37, 2404–2424. <https://doi.org/10.1029/2017TC004812>
- Kufner, S.-K., Schurr, B., Sippl, C., Yuan, X., Ratschbacher, L., Akbar, A. S. O. M., et al. (2016). Deep India meets deep Asia: Lithospheric indentation, delamination and break-off under Pamir and Hindu Kush (Central Asia). *Earth and Planetary Science Letters*, 435, 171–184. <https://doi.org/10.1016/j.epsl.2015.11.046>
- Kylander-Clark, A. R. C., Hacker, B. R., & Cottle, J. M. (2013). Laser-ablation split-stream ICP petrochronology. *Chemical Geology*, 345, 99–112. <https://doi.org/10.1016/j.chemgeo.2013.02.019>

- Laskowski, A. K., Kapp, P., Ding, L., Campbell, C., & Liu, X. (2017). Tectonic evolution of the Yarlung suture zone, Lopu Range region, southern Tibet. *Tectonics*, *36*, 108–136. <https://doi.org/10.1002/2016TC004334>
- Law, R. D. (2014). Deformation thermometry based on quartz c-axis fabrics and recrystallization microstructures: A review. *Journal of Structural Geology*, *66*, 129–161. <https://doi.org/10.1016/j.jsg.2014.05.023>
- Linnemann, U., Ouzegane, K., Drareni, A., Hofmann, M., Becker, S., Gärtner, A., & Sagawe, A. (2011). Sands of West Gondwana: An archive of secular magmatism and plate interactions—A case study from the Cambro-Ordovician section of the Tassili Ouan Ahaggar (Algerian Sahara) using U–Pb–LA-ICP-MS detrital zircon ages. *Lithos*, *123*(1), 188–203. <https://doi.org/10.1016/j.lithos.2011.01.010>
- Lister, G. S., & Davis, G. A. (1989). The origin of metamorphic core complexes and detachment faults formed during Tertiary continental extension in the Northern Colorado River Region, USA. *Journal of Structural Geology*, *11*(1–2), 65–94. [https://doi.org/10.1016/0191-8141\(89\)90036-9](https://doi.org/10.1016/0191-8141(89)90036-9)
- Liu, M., & Yang, Y. Q. (2003). Extensional collapse of the Tibetan Plateau: Results of three-dimensional finite element modeling. *Journal of Geophysical Research*, *108*(B8), 2361. <https://doi.org/10.1029/2002jb002248>
- Lovera, O. M., Richter, F. M., & Harrison, T. M. (1989). The  $^{40}\text{Ar}/^{39}\text{Ar}$  thermochronometry for slowly cooled samples having a distribution of diffusion domain sizes. *Journal of Geophysical Research*, *94*(B12), 17,917–17,935. <https://doi.org/10.1029/JB094iB12p17917>
- Ludwig, K. R. (2000). *SQUID 1.00: A User's Manual*. Berkeley: Berkeley Geochronology Center Special Publications.
- Ludwig, K. R. (2008). Isoplot 3.70. A geochronological toolkit for Microsoft Excel. *Berkeley Geochronology Center Special Publication*, *4*, 1–76.
- Lukens, C. E., Carrapa, B., Singer, B. S., & Gehrels, G. (2012). Miocene exhumation of the Pamir revealed by detrital geothermochronology of Tajik rivers. *Tectonics*, *31*, TC2014. <https://doi.org/10.1029/2011tc003040>
- Mahéo, G., Guillot, S., Blichert-Toft, J., Rolland, Y., & Pecher, A. (2002). A slab breakoff model for the Neogene thermal evolution of South Karakorum and South Tibet. *Earth and Planetary Science Letters*, *195*(1–2), 45–58. [https://doi.org/10.1016/s0012-821x\(01\)00578-7](https://doi.org/10.1016/s0012-821x(01)00578-7)
- McDougall, I., & Harrison, T. M. (1999). *Geochronology and thermochronology by the  $^{40}\text{Ar}/^{39}\text{Ar}$  method*. Oxford University: Press on Demand.
- McDowell, F. W., McIntosh, W. C., & Farley, K. A. (2005). A precise  $^{40}\text{Ar}/^{39}\text{Ar}$  reference age for the Durango apatite (U-Th)/He and fission-track dating standard. *Chemical Geology*, *214*(3–4), 249–263. <https://doi.org/10.1016/j.chemgeo.2004.10.002>
- Metzger, S., Schurr, B., Ratschbacher, L., Sudhaus, H., Kufner, S.-K., Schöne, T., et al. (2017). The 2015 Mw7.2 Sarez strike-slip earthquake in the Pamir Interior: Response to the underthrusting of India's western promontory. *Tectonics*, *36*, 2407–2421. <https://doi.org/10.1002/2017TC004581>
- Molnar, P., & Stock, J. M. (2009). Slowing of India's convergence with Eurasia since 20 Ma and its implications for Tibetan mantle dynamics. *Tectonics*, *28*, TC3001. <https://doi.org/10.1029/2008tc002271>
- Murphy, M. A., Yin, A., Kapp, P., Harrison, T. M., Manning, C. E., Ryerson, F. J., et al. (2002). Structural evolution of the Gurla Mandhata detachment system, southwest Tibet: Implications for the eastward extent of the Karakoram fault system. *Geological Society of America Bulletin*, *114*(4), 428–447. [https://doi.org/10.1130/0016-7606\(2002\)114<0428:Seotgm>2.0.Co;2](https://doi.org/10.1130/0016-7606(2002)114<0428:Seotgm>2.0.Co;2)
- Negredo, A. M., Replumaz, A., Villasenor, A., & Guillot, S. (2007). Modeling the evolution of continental subduction processes in the Pamir-Hindu Kush region. *Earth and Planetary Science Letters*, *259*(1–2), 212–225. <https://doi.org/10.1016/j.epsl.2007.04.043>
- Nikolaev, V. (2002). Afghan-Tajik depression: Architecture of sedimentary cover and evolution. *Russian Journal of Earth Sciences*, *4*(6), 399–421.
- Palin, R. M., Searle, M. P., Waters, D. J., Horstwood, M. S. A., & Parrish, R. R. (2012). Combined thermobarometry and geochronology of peraluminous metapelites from the Karakoram metamorphic complex, North Pakistan; New insight into the tectonothermal evolution of the Baltoro and Hunza Valley regions. *Journal of Metamorphic Geology*, *30*(8), 793–820. <https://doi.org/10.1111/j.1525-1314.2012.00999.x>
- Passchier, C. W., & Trouw, R. A. (2005). *Microtectonics*. Berlin: Springer Science & Business Media.
- Paton, C., Hellstrom, J., Paul, B., Woodhead, J., & Hergt, J. (2011). Iolite: Freeware for the visualisation and processing of mass spectrometric data. *Journal of Analytical Atomic Spectrometry*, *26*(12), 2508–2518.
- Pegler, G., & Das, S. (1998). An enhanced image of the Pamir Hindu Kush seismic zone from relocated earthquake hypocenters. *Geophysical Journal International*, *134*(2), 573–595. <https://doi.org/10.1046/j.1365-246x.1998.00582.x>
- Ratschbacher, L., Frisch, W., Linzer, H.-G., & Merle, O. (1991). Lateral extrusion in the eastern Alps, PArt 2: Structural analysis. *Tectonics*, *10*(2), 257–271. <https://doi.org/10.1029/90tc02623>
- Ratschbacher, L., Frisch, W., Neubauer, F., Schmid, S. M., & Neugebauer, J. (1989). Extension in Compressional Orogenic Belts—The Eastern Alps. *Geology*, *17*(5), 404–407. [https://doi.org/10.1130/0091-7613\(1989\)017<0404:Eicob>2.3.Co;2](https://doi.org/10.1130/0091-7613(1989)017<0404:Eicob>2.3.Co;2)
- Reiners, P. W., & Brandon, M. T. (2006). Using thermochronology to understand orogenic erosion. In *Annual Review of Earth and Planetary Sciences* (pp. 419–466). Palo Alto: Annual Reviews.
- Reiners, P. W., Ehlers, T. A., & Zeitler, P. K. (2005). Past, present, and future of thermochronology. In P. W. Reiners, & T. A. Ehlers (Eds.), *Low-temperature thermochronology: Techniques, interpretations, and applications* (pp. 1–18). Chantilly: Mineralogical Soc Amer.
- Reiners, P. W., Spell, T. L., Nicolescu, S., & Zanetti, K. A. (2004). Zircon (U-Th)/He thermochronometry: He diffusion and comparisons with  $^{40}\text{Ar}/^{39}\text{Ar}$  dating. *Geochimica et Cosmochimica Acta*, *68*(8), 1857–1887. <https://doi.org/10.1016/j.gca.2003.10.021>
- Renne, P. R., Balco, G., Ludwig, K. R., Mundil, R., & Min, K. (2011). Response to the comment by WH Schwarz et al. on “Joint determination of  $^{40}\text{K}$  decay constants and  $^{40}\text{r}/^{40}\text{K}$  for the Fish Canyon sanidine standard, and improved accuracy for  $^{40}\text{Ar}/^{39}\text{Ar}$  geochronology” by PR Renne et al.(2010). *Geochimica et Cosmochimica Acta*, *75*(17), 5097–5100.
- Renne, P. R., Mundil, R., Balco, G., Min, K., & Ludwig, K. R. (2010). Joint determination of  $^{40}\text{K}$  decay constants and  $^{40}\text{Ar}^*/^{40}\text{K}$  for the Fish Canyon sanidine standard, and improved accuracy for  $^{40}\text{Ar}/^{39}\text{Ar}$  geochronology. *Geochimica et Cosmochimica Acta*, *74*(18), 5349–5367. <https://doi.org/10.1016/j.gca.2010.06.017>
- Rey, P. F., Teyssier, C., & Whitney, D. L. (2010). Limit of channel flow in orogenic plateaux. *Lithosphere*, *2*(5), 328–332. <https://doi.org/10.1130/L114.1>
- Robbins, G. A. (1972). Radiogenic argon diffusion in muscovite under hydrothermal conditions, M.S. thesis, Brown University.
- Robinson, A. C., Yin, A., & Lovera, O. M. (2010). The role of footwall deformation and denudation in controlling cooling age patterns of detachment systems: An application to the Kongur Shan extensional system in the Eastern Pamir, China. *Tectonophysics*, *496*(1–4), 28–43. <https://doi.org/10.1016/j.tecto.2010.10.003>
- Robinson, A. C., Yin, A., Manning, C. E., Harrison, T. M., Zhang, S. H., & Wang, X. F. (2004). Tectonic evolution of the northeastern Pamir: Constraints from the northern portion of the Cenozoic Kongur Shan extensional system, western China. *Geological Society of America Bulletin*, *116*(7–8), 953–973. <https://doi.org/10.1130/b25375.1>

- Robinson, A. C., Yin, A., Manning, C. E., Harrison, T. M., Zhang, S.-H., & Wang, X.-F. (2007). Cenozoic evolution of the eastern Pamir: Implications for strain-accommodation mechanisms at the western end of the Himalayan-Tibetan orogen. *Geological Society of America Bulletin*, *119*(7-8), 882–896. <https://doi.org/10.1130/b25981.1>
- Roecker, S. W. (1982). Velocity structure of the Pamir-Hindu-Kush Region—Possible evidence of subducted crust. *Journal of Geophysical Research*, *87*(Nb2), 945–959. <https://doi.org/10.1029/JB087iB02p00945>
- Rolland, Y., Mahéo, G., Guillot, S., & Pecher, A. (2001). Tectono-metamorphic evolution of the Karakorum Metamorphic complex (Dassu-Askole area, NE Pakistan): Exhumation of mid-crustal HT-MP gneisses in a convergent context. *Journal of Metamorphic Geology*, *19*(6), 717–737. <https://doi.org/10.1046/j.0263-4929.2001.00342.x>
- Rutte, D., Ratschbacher, L., Khan, J., Stübner, K., Hacker, B. R., Stearns, M. A., et al. (2017). Building the Pamir-Tibet Plateau—Crustal stacking, extensional collapse, and lateral extrusion in the Central Pamir: 2. Timing and rates. *Tectonics*, *36*, 385–419. <https://doi.org/10.1002/2016TC004294>
- Rutte, D., Ratschbacher, L., Schneider, S., Stübner, K., Stearns, M. A., Gulzar, M. A., et al. (2017). Building the Pamir-Tibet Plateau—Crustal stacking, extensional collapse, and lateral extrusion in the Central Pamir: 1. Geometry and kinematics. *Tectonics*, *36*, 342–384. <https://doi.org/10.1002/2016TC004293>
- Sass, P., Ritter, O., Ratschbacher, L., Tympel, J., Matiukov, V. E., Rybin, A. K., & Batalev, V. Y. (2014). Resistivity structure underneath the Pamir and Southern Tian Shan. *Geophysical Journal International*, *198*(1), 564–579. <https://doi.org/10.1093/gji/ggu146>
- Schmidt, J., Hacker, B. R., Ratschbacher, L., Stübner, K., Stearns, M., Kylander-Clark, A., et al. (2011). Cenozoic deep crust in the Pamir. *Earth and Planetary Science Letters*, *312*(3-4), 411–421. <https://doi.org/10.1016/j.epsl.2011.10.034>
- Schurr, B., Ratschbacher, L., Sippl, C., Gloaguen, R., Yuan, X., & Mechie, J. (2014). Seismotectonics of the Pamir. *Tectonics*, *33*, 1501–1518. <https://doi.org/10.1002/2014tc003576>
- Schwab, M., Ratschbacher, L., Siebel, W., McWilliams, M., Minaev, V., Lutkov, V., et al. (2004). Assembly of the Pamirs: Age and origin of magmatic belts from the southern Tien Shan to the southern Pamirs and their relation to Tibet. *Tectonics*, *23*, TC4002. <https://doi.org/10.1029/2003tc001583>
- Singleton, J. S. (2013). Development of extension-parallel corrugations in the Buckskin-Rawhide metamorphic core complex, west-central Arizona. *Geological Society of America Bulletin*, *125*(3-4), 453–472. <https://doi.org/10.1130/b30672.1>
- Sippl, C., Ratschbacher, L., Schurr, B., Krumbiegel, C., Rui, H., Pingren, L., & Abdybachev, U. (2014). The 2008 Nura earthquake sequence at the Pamir-Tian Shan collision zone, southern Kyrgyzstan. *Tectonics*, *33*, 2382–2399. <https://doi.org/10.1002/2014tc003705>
- Sippl, C., Schurr, B., Yuan, X., Mechie, J., Schneider, F. M., Gadoev, M., et al. (2013). Geometry of the Pamir-Hindu Kush intermediate-depth earthquake zone from local seismic data. *Journal of Geophysical Research: Solid Earth*, *118*, 1438–1457. <https://doi.org/10.1002/jgrb.50128>
- Smit, M. A., Ratschbacher, L., Kooijman, E., & Stearns, M. A. (2014). Early evolution of the Pamir deep crust from Lu-Hf and U-Pb geochronology and garnet thermometry. *Geology*, *42*(12), 1047–1050. <https://doi.org/10.1130/g35878.1>
- Spear, F. S., Cheney, J. T., Pyle, J. M., Harrison, T. M., & Layne, G. (2008). Monazite geochronology in central New England: Evidence for a fundamental terrane boundary. *Journal of Metamorphic Geology*, *26*(3), 317–329. <https://doi.org/10.1111/j.1525-1314.2007.00751.x>
- Spencer, K. J., Hacker, B. R., Kylander-Clark, A. R. C., Andersen, T. B., Cottle, J. M., Stearns, M. A., et al. (2013). Campaign-style titanite U-Pb dating by laser-ablation ICP: Implications for crustal flow, phase transformations and titanite closure. *Chemical Geology*, *341*, 84–101. <https://doi.org/10.1016/j.chemgeo.2012.11.012>
- Sperner, B., Jonckheere, R., & Pfänder, J. A. (2014). Testing the influence of high-voltage mineral liberation on grain size, shape and yield, and on fission track and  $^{40}\text{Ar}/^{39}\text{Ar}$  dating. *Chemical Geology*, *371*, 83–95. <https://doi.org/10.1016/j.chemgeo.2014.02.003>
- Stearns, M. A., Hacker, B. R., Ratschbacher, L., Lee, J., Cottle, J. M., & Kylander-Clark, A. (2013). Synchronous Oligocene–Miocene metamorphism of the Pamir and the north Himalaya driven by plate-scale dynamics. *Geology*, *41*(1), 1071–1074. <https://doi.org/10.1130/g34451.1>
- Stearns, M. A., Hacker, B. R., Ratschbacher, L., Rutte, D., & Kylander-Clark, A. R. C. (2015). Titanite petrochronology of the Pamir gneiss domes: Implications for middle to deep crust exhumation and titanite closure to Pb and Zr diffusion. *Tectonics*, *34*, 784–802. <https://doi.org/10.1002/2014tc003774>
- Steele-MacInnis, M. (2018). Fluid inclusions in the system  $\text{H}_2\text{O}-\text{NaCl}-\text{CO}_2$ : An algorithm to determine composition, density and isochore. *Chemical Geology*, *498*, 31–44. <https://doi.org/10.1016/j.chemgeo.2018.08.022>
- Steele-MacInnis, M., Lecumberri-Sanchez, P., & Bodnar, R. J. (2012). HOKIEFLINCS\_H2O-NACL: A Microsoft Excel spreadsheet for interpreting microthermometric data from fluid inclusions based on the PVTX properties of  $\text{H}_2\text{O}-\text{NaCl}$ . *Computers & Geosciences*, *49*, 334–337.
- Stipp, M., Stünitz, H., Heilbronner, R., & Schmid, S. M. (2002). Dynamic recrystallization of quartz: Correlation between natural and experimental conditions. *Geological Society, London, Special Publications*, *200*(1), 171–190. <https://doi.org/10.1144/gsl.sp.2001.200.01.11>
- Strecker, M. R., Frisch, W., Hamburger, M. W., Ratschbacher, L., Semiletkin, S., Samoruyev, A., & Sturchio, N. (1995). Quaternary deformation in the Eastern Pamirs, Tajikistan and Kyrgyzstan. *Tectonics*, *14*(5), 1061–1079. <https://doi.org/10.1029/95tc00927>
- Strecker, M. R., Hilley, G. E., Arrowsmith, J. R., & Coutand, I. (2003). Differential structural and geomorphic mountain-front evolution in an active continental collision zone: The northwest Pamir, southern Kyrgyzstan. *Geological Society of America Bulletin*, *115*(2), 166–181.
- Stübner, K., Ratschbacher, L., Rutte, D., Stanek, K., Minaev, V., Wiesinger, M., & Gloaguen, R. (2013). The giant Shakh dara migmatitic gneiss dome, Pamir, India-Asia collision zone: 1. Geometry and kinematics. *Tectonics*, *32*, 948–979. <https://doi.org/10.1002/tect.20057>
- Stübner, K., Ratschbacher, L., Weise, C., Chow, J., Hofmann, J., Khan, J., et al. (2013). The giant Shakh dara migmatitic gneiss dome, Pamir, India-Asia collision zone: 2. Timing of dome formation. *Tectonics*, *32*, 1404–1431. <https://doi.org/10.1002/tect.20059>
- Thiede, R. C., Sobel, E. R., Chen, J., Schoenbohm, L. M., Stockli, D. F., Sudo, M., & Strecker, M. R. (2013). Late Cenozoic extension and crustal doming in the India-Eurasia collision zone: New thermochronologic constraints from the NE Chinese Pamir. *Tectonics*, *32*, 763–779. <https://doi.org/10.1002/tect.20050>
- Thompson, J. A., Burbank, D. W., Li, T., Chen, J., & Bookhagen, B. (2015). Late Miocene northward propagation of the northeast Pamir thrust system, northwest China. *Tectonics*, *34*, 510–534. <https://doi.org/10.1002/2014tc003690>
- Tirel, C., Brun, J.-P., & Burov, E. (2004). Thermomechanical modeling of extensional gneiss domes. *Geological Society of America Special Papers*, *380*, 67–78. <https://doi.org/10.1130/0-8137-2380-9.67>
- Van Achterbergh, E., Ryan, C., & Griffin, W. (1999). GLITTER: On-line interactive data reduction for the laser ablation inductively coupled plasma mass spectrometry microprobe, paper presented at Ninth Annual VM Goldschmidt Conference.
- Van den Kerkhof, A., & Thiery, R. (2001). Carbonic inclusions. *Lithos*, *55*(1-4), 49–68.

- Vanderhaeghe, O., Teyssier, C., & Wysoczanski, R. (1999). Structural and geochronological constraints on the role of partial melting during the formation of the Shuswap metamorphic core complex at the latitude of the Thor-Odin dome, British Columbia. *Canadian Journal of Earth Sciences*, 36(6), 917–943. <https://doi.org/10.1139/cjes-36-6-917>
- Vermeech, P. (2012). On the visualisation of detrital age distributions. *Chemical Geology*, 312–313, 190–194. <https://doi.org/10.1016/j.chemgeo.2012.04.021>
- Villa, I. M., & Hanchar, J. M. (2013). K-feldspar hydrochronology. *Geochimica et Cosmochimica Acta*, 101, 24–33. <https://doi.org/10.1016/j.gca.2012.09.047>
- Villareal, D., Robinson, A. C., Worthington, J., Chapman, J. B., Carrapa, B., Oimahmadov, I., et al. (2017). Timing of crustal suturing in the Pamir, in Geological Society of America 2017 Meeting, Seattle, WA.
- Vlasov, N. G., Dyakov, Y. A., & Cherev, E. S. (1991). Geological map of the Tajik SSR and adjacent territories, 1:500,000, Vsesojuznoi Geological Institute Leningrad, St. Petersburg.
- Whitney, D. L., & Evans, B. W. (2010). Abbreviations for names of rock-forming minerals. *American Mineralogist*, 95(1), 185–187. <https://doi.org/10.2138/am.2010.3371>
- Whitney, D. L., Teyssier, C., & Vanderhaeghe, O. (2004). Gneiss domes and crustal flow. *Geological Society of America Special Papers*, 380, 15–33. <https://doi.org/10.1130/0-8137-2380-9.15>
- Wiedenbeck, M., Alle, P., Corfu, F., Griffin, W., Meier, M., Oberli, F., et al. (1995). Three natural zircon standards for U-Th-Pb, Lu-Hf, trace element and REE analyses. *Geostandards Newsletter*, 19(1), 1–23.
- Willett, S. D., & Beaumont, C. (1994). Subduction of Asian lithospheric mantle beneath Tibet inferred from models of continental collision. *Nature*, 369(6482), 642–645. <https://doi.org/10.1038/369642a0>
- Williams, I. S. (1998). U-Th-Pb geochronology by ion microprobe. *Reviews in Economic Geology*, 7, 1–35.
- Yin, A. (2004). Gneiss domes and gneiss dome systems. *Geological Society of America Special Papers*, 380, 1–14. <https://doi.org/10.1130/0-8137-2380-9.1>
- Yuan, H., Gao, S., Liu, X., Li, H., Günther, D., & Wu, F. (2004). Accurate U-Pb age and trace element determinations of zircon by laser ablation-inductively coupled plasma-mass spectrometry. *Geostandards and Geoanalytical Research*, 28(3), 353–370. <https://doi.org/10.1111/j.1751-908X.2004.tb00755.x>
- Yushin, I. P., Sass, M. E., Karapetov, S. S., Altukhov, S. M., Teplov, I. C., Raekov, C. R., et al. (1964). 1:200,000 maps of the Tajik SSR, Russian Geological Research Institute.
- Zanchetta, S., Worthington, J., Angiolini, L., Leven, E. J., Villa, I. M., & Zanchi, A. (2018). The Bashgumbaz Complex (Tajikistan): Arc obduction in the Cimmerian orogeny of the Pamir. *Gondwana Research*, 57, 170–190. <https://doi.org/10.1016/j.gr.2018.01.009>
- Zubovich, A. V., Wang, X.-q., Scherba, Y. G., Schelochkov, G. G., Reilinger, R., Reigber, C., et al. (2010). GPS velocity field for the Tien Shan and surrounding regions. *Tectonics*, 29, TC6014. <https://doi.org/10.1029/2010tc002772>